Lunar Occultation Studies of Late type Stars

A THESIS

submitted for the Award of Ph.D. degree of

MOHANLAL SUKHADIA UNIVERSITY

in the

Faculty of Science

BY

Tapas Baug

Under the Supervision of

Prof. A.K. Ambastha
Physical Research Laboratory, Ahmedabad

Department of Physics

MOHANLAL SUKHADIA UNIVERSITY

UDAIPUR

Year of submission: 2012

In memory

of my grand-parents

DECLARATION

I, **Mr. Tapas Baug**, S/o Mr. Saroj Kr. Baug, resident of C-104, PRL residences, Navrangpura, Ahmedabad 380009, hereby declare that the research work incorporated in the present thesis entitled, **"Lunar Occultation Studies of Late type Stars"** is my own work and is original. This work (in part or in full) has not been submitted to any University for the award of a Degree or a Diploma. I have properly acknowledged the material collected from secondary sources wherever required. I solely own the responsibility for the originality of the entire content.

Date:

Tapas Baug
(Author)

CERTIFICATE

I feel great pleasure in certifying that the thesis entitled, **"Lunar Occultation Studies of Late type Stars"** by Mr. Tapas Baug under my guidance. He has completed the following requirements as per Ph.D regulations of the University.

(a) Course work as per the university rules.

(b) Residential requirements of the university.

(c) Regularly submitted six monthly progress reports.

(d) Presented his work in the departmental committee.

(e) Published minimum of one research papers in a referred research journal.

I recommend the submission of thesis.

Date:

Dr. Ashok Ambastha
Professor, USO,
Physical Research Laboratory,
Ahmedabad - 380 009.

Countersigned by

Head of the Department

Acknowledgements

First of all, I express my sincere and deepest gratitude to Prof. T. Chandrasekhar, who has introduced me to the observational universe and under the guidance of whom, the work reported in this thesis has been carried out. His deep insight in the subject and vast experience helped me immensely in learning the subject. Discussion with him was a great pleasure as he always gave importance to my views and was always patient with me. It was a great experience to work with him and I consider myself fortunate to have him as my supervisor.

I take this opportunity to offer my profound gratitude to Prof. A.K. Ambastha who has been my co-guide throughout this period. He helped me whenever I asked for it, even on his way to Air-port!

I have greatly profited by the valuable astronomical discussion with Prof. N.M. Ashok. He always patiently answered my questions, irrespective of its silliness. I thank A&A faculty members, Prof. B.G. Anandarao, Prof. Hari Om Vats, Prof. Janardhan, Dr. D.P.K. Banerjee, Dr. Singal, Dr. Baliyan, Dr. Abhijit Chakraborty, Dr. Santhosh Vadawale, Dr. Shashikiran Ganesh who always encouraged me during the period. I specially thank Dr. Sachindra Naik for his critics which always cheered me up. I would also like to thank Dr. Shibu Mathew for helping me out of the registration trap.

I thank Prof. J. N. Goswami, Director; Prof. Anjan Joshipura and Prof. A. K. Singhvi, former Deans, and Prof. Utpal Sarkar, Dean of PRL for providing necessary facilities and encouragements to carry out research work.

I thank all the staffs of PRL computer center for providing excellent computational and internet facilities. I must express my appreciation for the cooperation and help extended ever-willingly by the library and its staff members.

I have always enjoyed the visit to Gurushikhar for making observations. The wonderful company of Purohitji, Jinesh bhai, Rajesh bhai, Mathur bhai, Nafees, Mahendra and Hitesh at Mt. Abu has left pleasant memories.

I thank Murli bhai, Vadheer ji and PRL Admin for helping me in many official works. I always enjoyed the company of Murli bhai, Vadheerji, Kaka (Kayasth), Vishal Shah and A.B. Shah. They, specially Kaka, made the daily *bus journey between PRL main campus and Thaltej the most enjoyable event.*

Life in PRL would have never been same without Khan, Srinivas, Prashant, Moumita, Iman, Pravin, Ketan, Patra, Awasthi, Ashish, Suruchi, Satinder, Arvind, Jayati, Suratna di, Ritesh and 'time killing benchmates' Amjad da, Bhaswar da, Soumya, Rabiul da, Sandy, Suman da, Anand, Villu (captain), Ashok, Sreekanth, Vinni, Sarkhel, Alok bhai, Akhilesh (Dr. Naughty), Zeen, Purnendu da, Jaydeep, Sidhartha, Vema and Avdhesh. I am specially thankful to Jayati, Khan, Iman and Bhaswar da for their unconditional support during bad periods of my life. I spent many memorable experience with them.

I enjoyed the company of Ramkrishna da, Blesson, Venkat, Vishal bhai, Sunil, Susanta, Arun, Priyanka, Anjali, Tanmoy, Gaurav, Varun, Vaibhav, Ranjith, Rishi and Pragya. They made my life in Thaltej cheerful. I would also like to thank Ramkrishna da, Vishal bhai, Soumen da and Anandmayee for the fruitful discussion and suggestions.

I would also like to thank Dr. Somenath Chakraborty who first taught me the Theoretical Astronomy. I acknowledge Shri Biplab Kumar Manna, my favorite teacher cum friend who taught me how to stand still. My friends Bultu, Somnath, Kuntal, Debu, Amit, Robin, Swarup, Ananda, Nibedita, Latif, Sougat, Hirak, Harry (Haridas) and Milton (Swagat) periodically refreshed me either in phone or face to face whenever I visited home.

This thesis is incomplete if I do not acknowledge Google and SIMBAD database. Google always tried to make my life easier like a true friend.

I am also grateful to my uncle, aunt and in-laws for providing the mental support and encouragement through out the period.

Finally last but not the least the devotion I got from my parents, my brother, my family members and my beloved Supriya is something beyond acknowledgement. They were always with me for whatever reason it may be and the encouragement I received from them will never fade away.

Tapas

ABSTRACT

This thesis presents high angular resolution study of a few late type giant stars using the lunar occultation (LO) technique in the near infrared region (NIR). Due to the motion of the sharp lunar limb relative to the stars many of them disappear (and reappear from) behind the moon. At the point of disappearance (or reappearance) Fresnel diffraction of the star light occurs. The diffraction pattern sweeps across the earth's surface and can be collected as a time varying signal by a telescope in the path. The observed light curve of the event is capable of yielding milliarcsecond spatial resolution on the occulted source. All the LO observations reported in the thesis have been carried out in the Near-IR (NIR) K-band (2.2 μm) using the fast sub-array mode of IR-camera (NICMOS) attached to 1.2m Mt. Abu telescope. The fast sub-array mode was specially developed for lunar occultation observations. In this thesis, two magnitude fainter sources, than observed earlier with fast photometer, have been studied. Using NICMOS sub-array, lunar occultation of sources upto K-magnitude of 5.0 have been successfully observed. Three separate studies are presented in this thesis using this technique - (1) Rare LO events towards the Galactic centre, (2) Determination of angular diameter of a few highly evolved cool stars called Asymptotic Giant Branch (AGB) variables, and (3) Noise reduction of LO light curves using Fourier and Wavelet Transforms.

The rare passages of the moon's disk in the high stellar density region in the vicinity of the Galactic centre provide an opportunity to study occulted sources at high angular resolutions. During one such passage (September 19, 2007) we have observed a dozen events successfully. The minimum approach to Galactic centre during the observations was about $1^{\circ}.0$. A detailed analysis of the occultation light curves and limiting angular resolution of this method shows that in atleast 3 cases the sources are well resolved. At the distance to these sources, estimated indirectly, using K-band extinction and available spectral data, the resolved structures do not correspond to stellar disks and suggest a more extended circumstellar emission. Within limits of distance

errors we estimate the extent of circumstellar material around these sources in units of the respective stellar radii.

The uniform disk (UD) angular diameter measurements of two oxygen-rich Mira variables (AW Aur and BS Aur) and three semiregular (SRb) variables (GP Tau, RS Cap, RT Cap), in near Infrared K-band (2.2 μm) by lunar occultation observations are reported. UD angular diameters of the two Miras and one SRV are first time measurements. In addition a method of predicting angular diameters through a calibration using (V-K) colour is discussed and applied to the five sources. The effect of mass-loss enhancing measured K-band diameters is examined for Miras using $(K - [12])$ colour excess as an index. In our sample the measured angular diameter of one of the Miras (BS Aur) is found enhanced by nearly 40% compared to its expected value, possibly due to mass loss effects leading to formation of a circumstellar shell.

Sources fainter than observed earlier are targeted using the NICMOS sub-array in this thesis. The angular resolution achieved on a source is sensitive to the signal to noise ratio (S/N) of the observed light curve. Two noise reduction techniques using Fourier and Wavelet transforms have been carried out on the observed light curves and both of them, specifically Wavelet transforms, are found to be effective in terms of S/N improvement of the light curves. But the intrinsic smoothening effect of the Wavelet transforms deforms the observed fringes and leads to fit higher uniform disk angular diameter. An improvement in the S/N of the light curve as well as model fit using Fourier transforms is obtained in the fainter regime ($m_K \geq$3.3) of our sample.

LIST OF PUBLICATIONS

A. Publications related to the thesis work

1. **"Lunar Occultations of sources in the near infrared towards the Galactic centre"**
   T. Chandrasekhar and **Tapas Baug**
   2010, MNRAS, 408, 1006

2. **"Near Infrared Angular diameters of a few AGB variables by Lunar Occultations"**
   Tapas Baug and T. Chandrasekhar
   2012, MNRAS, 419, 866

Small Publications

1. **"Near-infrared angular diameters of a few Asymptotic Giant Branch variables by Lunar occultations"**
   Tapas Baug and T. Chandrasekhar
   2011, The AGB Newsletter, 171, p8

Contents

List of Tables

List of Figures

Chapter 1

Introduction

1.1 Stars in Solar neighbourhood

There are more than 10^{11} stars in our Galaxy, the Milky way which is about 30 kilo-parsec (kpc) across and only about 300 pc thick (Cabrera-Lavers et al., 2008). The sun is located towards the outer part of the Milky way at a distance of about 8 kpc from the centre. According to the Hipparcos catalog (Perryman et al., 1997), more than 100 000 stars with V-band magnitude limit of m_V $\leq$12.4 are present in the solar neighborhood within $\sim$1kpc. The Hertzsprung-Russell diagram of 20 853 stars which have atleast 10% accuracies in the Hipparcos parallax measurements is shown in Fig.1.1. The vertical line in the plot represents the sources with spectral type $K0$ and have intrinsic (B-V) colour of 0.80 (Lang, 1991). Our interest is in late-type giants present in upper-right quadrant in the figure.

A large fraction of the late-type giants experience mass-loss and develop circumstellar shells. After completion of the hydrogen burning inside the core these stars move away from the 'main-sequence' and generally expand to linear sizes of about 100 times bigger than their main sequence counter parts. The expansion of the stellar envelopes lead to low surface temperatures ($T_{eff} \sim$ 4000), which makes them brighter in the near infrared (NIR; 1-5 μm) than in the visible region. Observational studies of these evolved stars help in investigations related to late stages of stellar evolution and for fine tuning model atmospheres. The material ejected by these stars via mass-loss processes, are an important source for replenishment of the interstellar medium. Due to their high luminosities, these stars can be detected at greater distances and serve as an important tool in the study of the interstellar extinction. However, late-type giants are relatively rare objects. It can be seen that a small fraction of sources are present in the upper-right quadrant of the Fig.1.1.

Among the late-type giants the Asymptotic Giant Branch (AGB) variables are a special class and have a distinct importance. The AGB variables, which include early-AGB semi-regulars to evolved-AGB Mira variables, often experience huge mass-loss at a rate of about 10^{-7} to 10^{-6} $M_{\odot}$/yr. Miras also experience stellar pulsations. The detailed physical nature of mass-loss process, region where it originates, and particularly its connection with pulsation mechanism are not well understood. Also, the mechanism by which spherically symmetric AGBs evolve to axisymmetric planetary nebulae is unknown. Their high luminosities and enormous sizes of about 1 Astronomical Unit ($\sim$214 $R_{\odot}$) make them resolvable at distances of a few hundreds of parsec from the sun. The extended atmospheres of these cool giants are believed to be the habitable zones for dust formation. Observational evidence has been found for different species of molecules to form at different layers in the atmosphere depending on their condensation temperatures (Wittkowski et al., 2011). Recently, the mid- and far-infrared observations are revealing interesting properties of AGB stars. Unexpected presence of water vapour has been detected on a sample of eight carbon-rich AGB variables in the mid-IR using Herschel Space Observatory (Neufeld et al., 2011). More details on AGB variables is discussed in Chapter 4.

The high angular resolution (HAR) data for Miras is still limited especially if one considers that it is phase and wavelength dependent. It is important to study these stars at high angular resolution at NIR wavelengths. HAR observations in the NIR help to understand the stellar atmosphere and detect close circumstellar envelope of these stars.

The angular diameter values of stars along with the bolometric flux can

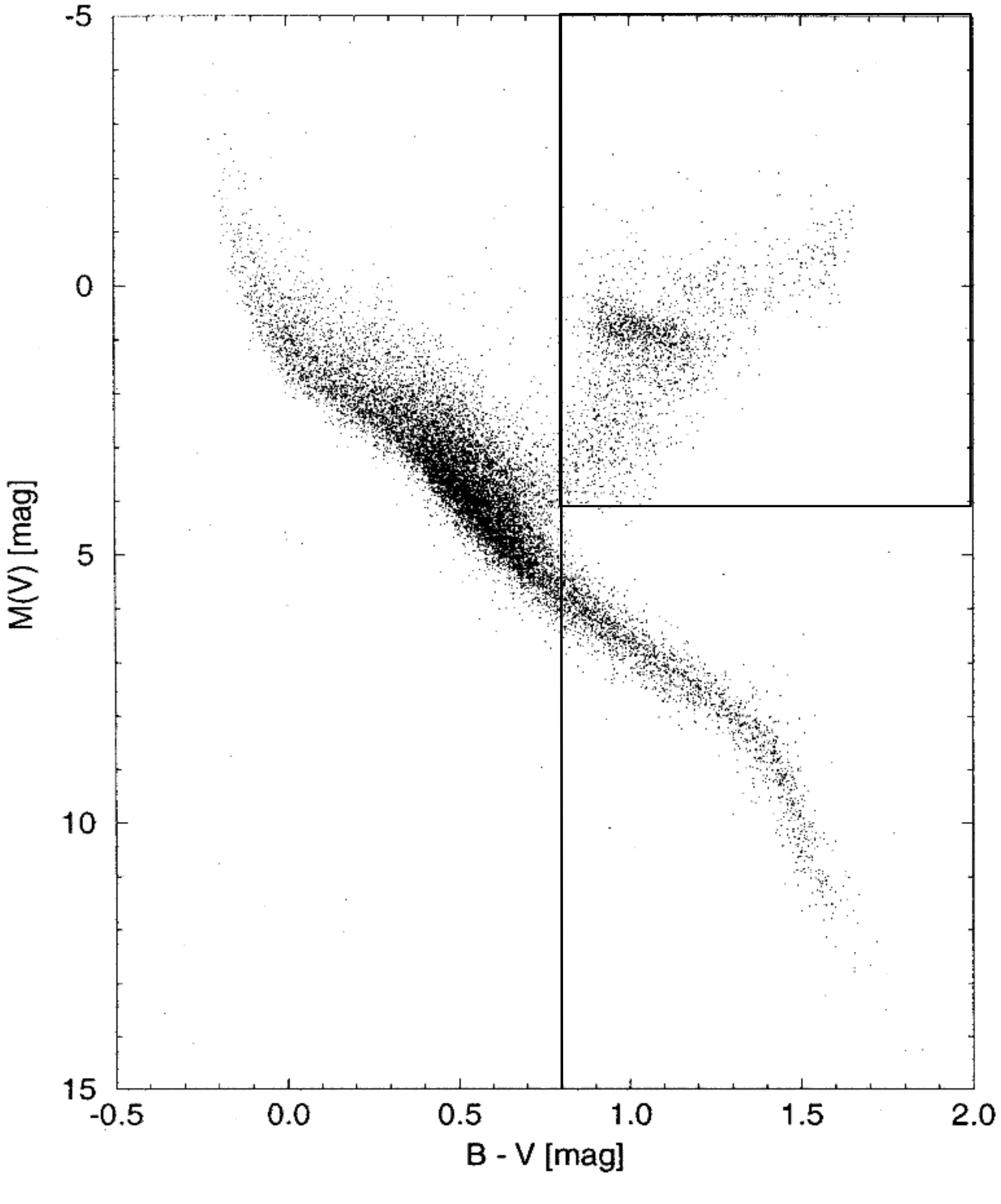

Figure 1.1: The observational Hertzsprung-Russell diagram, M_V versus $(B-V)$, for the 20 853 stars with $\sigma_\pi/\pi < 0.1$ is reproduced from 'The Hipparcos Catalog' (Perryman et al., 1997). The sources in the right of the vertical line correspond to late type stars which have intrinsic (B-V) colours more than 0.80 (Lang, 1991). The sources inside upper-right quadrant are late-type giants.

determine their effective temperatures, independent of their distances. Also linear size of a star can be determined if good parallax measurements are available (like Hipparcos new reduction; van Leeuwen, 2007). Direct determination of these fundamental quantities are required to validate and refine stellar evolution models as well as models on their dynamic atmospheres.

Due to turbulence in the earth's atmosphere, the actual angular size of a star cannot be determined from the ground based observations with simple imaging techniques. In astronomy this distortion of stellar image by the turbulence in the earth's atmosphere, is quantified as atmospheric *seeing*. The *seeing* disk has typically an angular size of ∼1.0 arcsecond which is about thousand times more than the angular size of a typical star. Hence, the need for the HAR studies to go below the *seeing* limit. This thesis comprises the application of HAR technique of Lunar Occultations to late-type giants.

1.2 Evolution of Late-type giants

In the Hertzsprung-Russell (H-R) diagram (Fig.1.2) the stars fusing hydrogen inside the core are arranged according to their masses. The stars spend most of their lifetime at this phase known as 'Main-sequence'. The thermonuclear process is very sensitive to the mass of the star. High mass stars burn the hydrogen fuel inside the core much faster than the low mass stars and hence, have shorter life-times.

The low mass stars with $M_\star \leq 0.5 M_\odot$ spend the longest time of about 10^{12} to 10^{13} years in the main-sequence and will finish their evolution as $Helium$ white dwarfs. They do not have enough gravitational energy to ignite helium and will never reach the red-giant branch. Our interest is in stars of 1-2 $M_\odot$ which evolve into red-giants and subsequently enter the AGB phase after leaving the main-sequence.

The stars, like our sun spend about 10^{10} years in the hydrogen burning phase. After exhaustion of the hydrogen fuel (to helium) inside the core, they contract under the influence of gravitational force. As the core temperature is

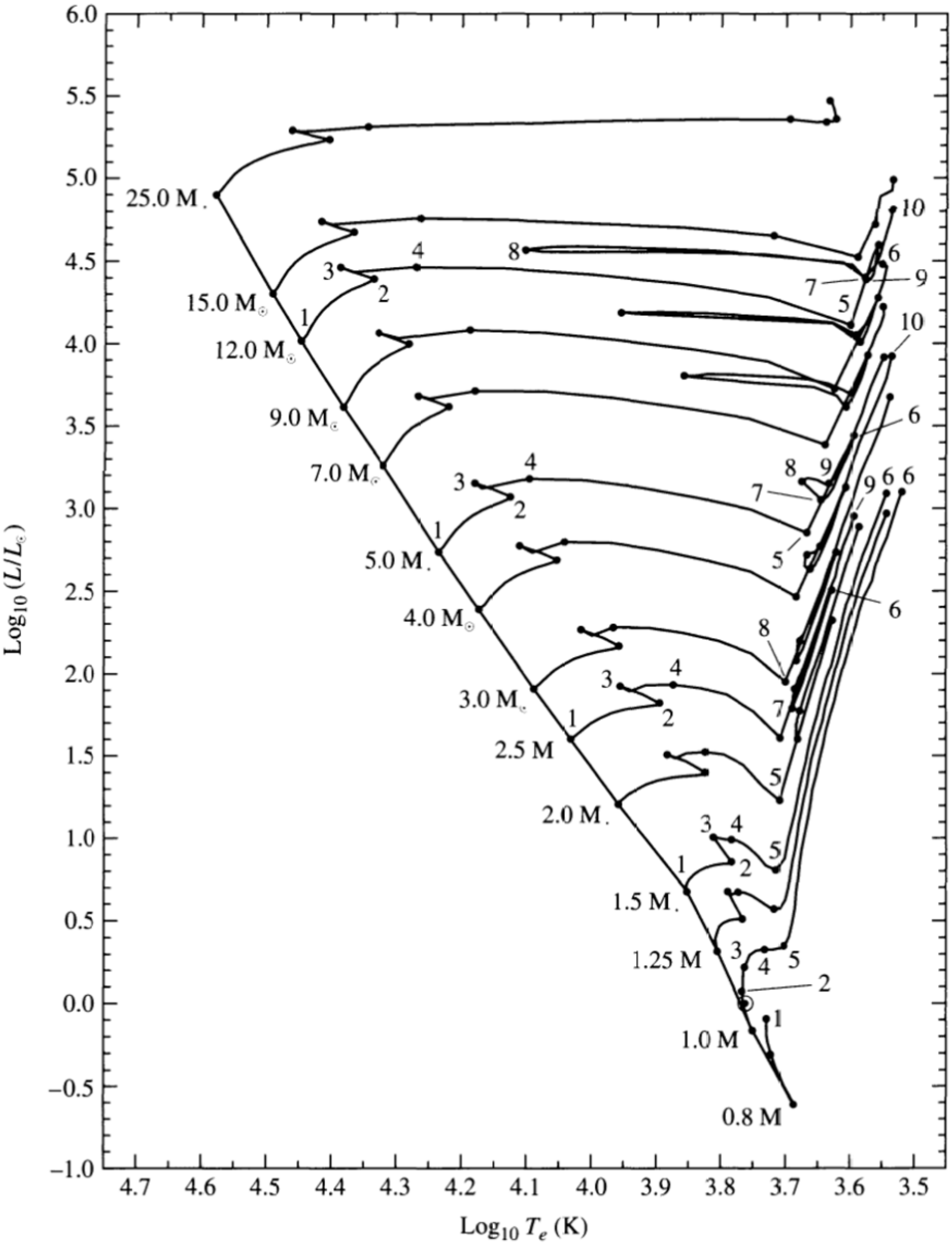

Figure 1.2: The Hertzsprung-Russle diagram adopted from Carrol & Dale (2007). The stellar evolution tracks from $0.8M_\odot$ to $25M_\odot$ stars are shown.

not sufficient to start the helium fusion (about 10^8 K), there is no radiation pressure to prevent the contraction. But the star burns hydrogen in a shell just outside the core which heats up the envelope making it expand. This eventually leads the star to leave the main-sequence and move up the red giant branch (RGB). Due to the expansion, surface temperature of the star decreases and it becomes cooler. At this phase the star becomes huge in size and also highly luminous due to the large surface area.

Meanwhile, the gravitational compression heats the core enough to start helium fusion (to carbon/oxygen). But during that period degenerate electron gas starts dominating the pressure inside the core. The electron degeneracy pressure is independent of temperature. So, the temperature increase due to the production of energy becomes a self-consistent process and leads to a rapid rate of helium fusion. This is known as helium flash. After the exhaustion of helium in the core, the star is left with carbon/oxygen-rich core, surrounded by helium fusing shell and a hydrogen burning shell above that. The energy from the burning shells again leads the star to giant branch but not following the same path it had taken after exhaustion of hydrogen. Hence, they are known as Asymptotic Giant Branch (AGB) Star. One solar mass stars are not massive enough to start carbon burning inside the core and hence, this is the end of their nuclear burning in the core. Pulsation and radiation pressure on dust cause a dense stellar wind of variable strength, obscuring the object from view at short wavelengths. At the tip of the AGB, mass-loss rates have risen to such high values that this essentially removes the hydrogen-rich stellar envelope, thus effectively terminating the AGB-phase. Due to the expansion of the outer layer optical depth decreases and enables observers to see deeper into the star. This phase is known as Planetary nebula and finally it ends as a white dwarf (the naked core).

The evolution of high mass stars is little different. These stars are massive enough to successively ignite helium, carbon, neon, oxygen and silicon in the core and follow a completely different evolutionary track than the low mass stars. The detail evolutionary tracks of stars with different mass ($0.8 - 25$

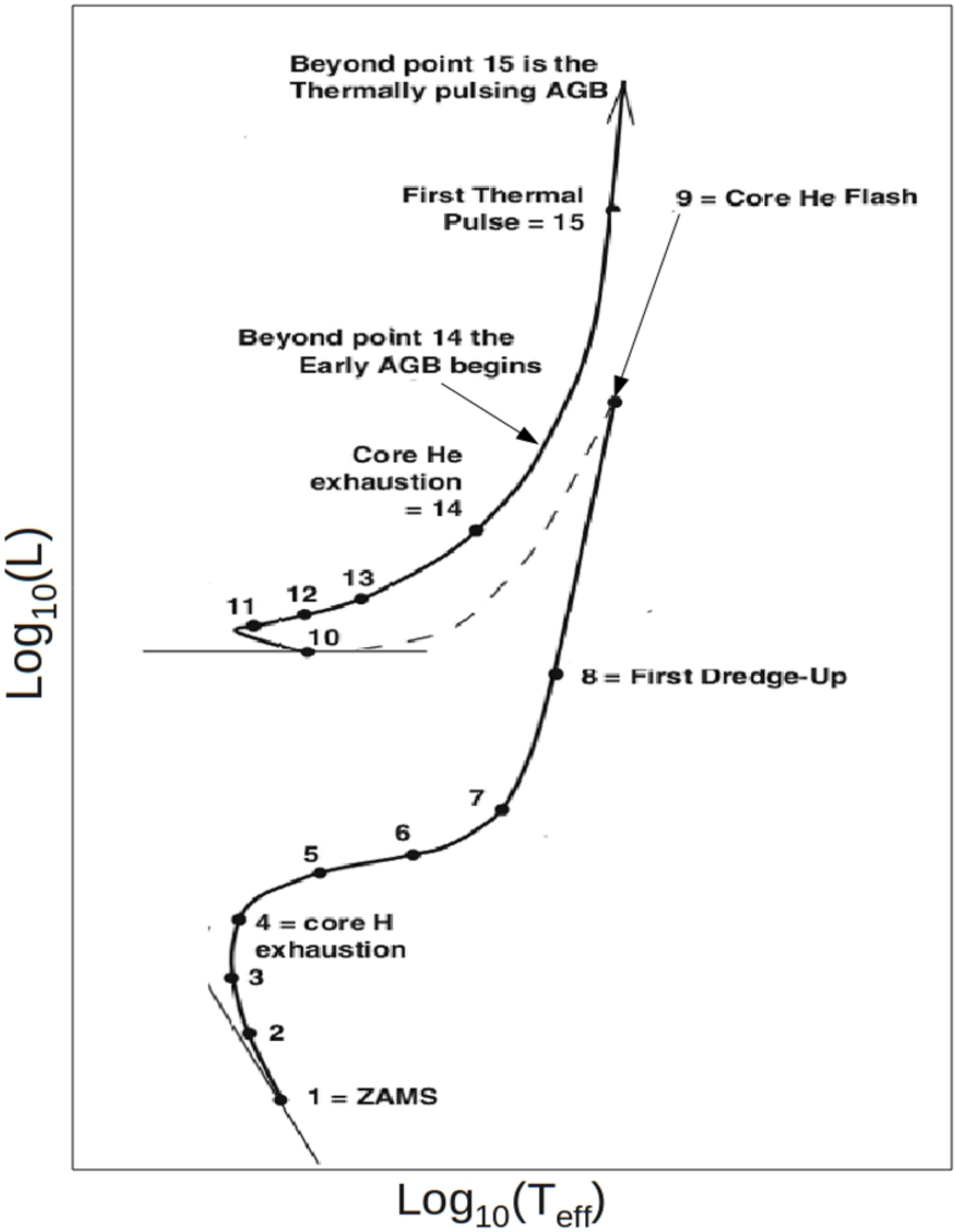

Figure 1.3: The Hertzsprung-Russell diagram adopted from Lattanzio & Peter (2003) and modified. The evolutionary track of $1M_{\odot}$ star is shown.

$M_\odot$) are shown in Fig.1.3. More details on the stellar evolution can be found in the book by Le Blank (2010). Details on AGB evolution is given in a review article by Herwig (2005).

1.3 Time line of High Angular Resolution (HAR) Studies

The main barrier in the acquisition of a direct detailed image of a star using ground based telescopes is the turbulence in the earth's atmosphere. In the absence of the atmosphere, the imaging performance of a telescope with perfect optics is also limited by the diffraction effect of the finite aperture. Any finite aperture produces a natural spread of the image due to diffraction effects of the wave nature of light. The point spread function of a perfect telescope is given by Airy disk pattern. If two point sources are separated by an angle θ then they will be just resolved if the centre of the Airy disk of one image superimposed with the first minima of the other source. This is called 'diffraction limit' or *Rayleigh* criterion. For a circular aperture the 'diffraction limit' is given by -

$$\theta = 1.22\frac{\lambda}{D} \text{ rad}, \tag{1.1}$$

where λ is the wavelength of observation, D is the diameter of the telescope aperture used in observation. At 2.2 μm, the diffraction limited resolution of a large 10m telescope is about 50 milliarcseconds (mas). It must be noted that measured angular diameter values of even the largest stars in the solar neighbourhood have been below 50 mas.

The distortion of the stellar images are caused by both temporal and spatial variation of the refractive index of air parcels above the telescope aperture. The distortion is quantified by the parameter called *seeing*. Due to differential temperature and wind flow in the different layers of the atmosphere, the atmosphere acts like a randomly changing lens. When a plane wavefront passes through, it randomly changes the phase of the incoming wavefront which finally leads to the distortion of the stellar images. The atmospheric parameters which cause the variations in the phase are characterized by spatial scale called Fried parameter (r_o) or coherence length (Fried, 1966), and the temporal scale as coherence time (t_o). Fried parameter is formally defined as the diameter of the circular aperture over which the rms variation of the phase of the incoming light wavefront is one radian.

These two atmospheric parameters perturb both phase and amplitude of the incoming wavefront. The phase variation is related to the *seeing* while the amplitude variation is related to the *scintillation* or twinkling of the image. Scintillation does not cause blurring of the image but changes the apparent brightness of it. The blurring of the image is related to the *seeing*.

The quest for achieving high angular resolution of distant stellar bodies started in the beginning of the 20^{th} century. The first angular diameter measurement is reported in the innovative work by Michelson & Pease (1921). However, the idea of measuring angular diameters using interferometry was introduced much earlier by Fizeau (1868). In Michelson stellar interferometer, two sub-apertures of the extended telescope are treated as two slits and light from them is made to interfere to produce fringe patterns. But this technique is limited to the large angular diameters only. Michelson & Pease (1921) reported the first uniform disk angular diameter measurement of Betelgeuse (α Ori) to be 47±5 milliarcsecond (mas) using a 20 ft stellar interferometer on 100 inch Hooker Telescope at Mt. Wilson, USA. They went on to report angular diameter of 6 cool giants and supergiants. Their attempts to extend the work in measuring angular diameters of more stars using longer baseline, failed due to mechanical limitations.

Next important development in HAR originated with the novel idea of intensity interferometry by Hanbury Brown & Twiss (1956). In this method intensity, rather than conventional amplitude interference, patterns were obtained. The second order correlation between the fringes, produced by two independent telescopes, which is a tiny effect was observed. Hence, this method was limited to observe brighter sources only with B-magnitudes (m_B) of 2.5.

In 1970 Labeyrie proposed that it is possible to extract the high angular information upto the diffraction limit of the source if the observed images are recorded fast enough to virtually freeze the atmospheric turbulence. For a typical wind speed of 10 m/s and the wavelength of 2.2 μm it demands for the image to be recorded faster than the *coherence* time of 50 msec to virtually freeze the atmosphere. For visible wavelengths the requirement is more stringent with a coherence time of $\sim$10 msec. In rapidly acquired images, within the seeing disk one can see smaller patterns called speckles which carry angular diameter informations upto the diffraction limit.

Speckle interferometry has been used for high angular resolution measurements upto the diffraction limit of telescope aperture. Hence, larger telescopes are required to extract finer angular diameter information. Speckle interferometry has been particularly successful in identifying close binaries in a large number of stellar systems. McAlister et al. (1987) had detected a total of 112 binaries after surveying on a sample of 672 stars. Hartkopf et al. (2000) reported 2017 measurements of 1286 binary stars observed using speckle interferometry in CHARA speckle program. A recent interesting study on exoplanet host stars confirming 'companions' using speckle interferometry can be found in Mason et al. (2011).

Adaptive Optics (AO) also provides angular resolution upto the diffraction limit in ground-based observations. In AO, atmospherically distorted wavefronts are compensated using a real-time feedback system. AO system consists of a wavefront sensor, which measures distortion in the parallel incoming wavefront. Then a correction signal is sent to the deformable 'segmented/rubber' mirror with fast computer system. The deformable mirror changes its shape to compensate atmospheric effects. An AO system requires a near-by bright reference star (point source) to provide adequate signal to wavefront sensor for point spread function. However, artificial (laser) guide star is also used because it is not always possible to get a bright guide star inside the field of view. In the NIR, corrections for only lower order image motion (tip-tilt) can often give diffraction limited images on moderate size 2-4 m telescopes (Mc-

Caughrean et al., 1994). Nowadays, AO system has become part of the optical system of large telescopes because it provides better imagery.

The field of HAR took a big leap after 1970, particularly after the optical/IR interferometers began operating at large telescopes at VLT and Keck. In 1975 Labeyrie first reported the interference fringes using Long baseline interferometry with separate telescopes, an extended version of Michelson interferometer, in Interfèrométre á Deux Télescopes (I2T) at Observatoire de la Cote d'Azur, France. In the first application, $Vega$ was the scientific target and reported that it has an angular diameter $< 0''.005$. The first application of Michelson interferometry in the infrared was carried out by McCarthy & Low (1975) at 5 μm and they observed 11 late-type stars.

A variant is aperture interferometry using a series of small openings in the closed aperture of a large telescope. In the aperture masking technique the smaller masks remove the atmospheric noise. The closure phase method is applied to the observed data. A recent study on two debris disk stars HD 92945 and HD 141569 using mask of 7 holes in VLT can be found in Lacour et al. (2011).

We briefly discuss the main high angular resolution technique of optical long baseline interferometry followed by the technique of lunar occultation used in this thesis.

1.3.1 Optical Long baseline Interferometry

Long baseline ($\geq$100m) interferometry (LBI) uses the principle of Young's double slit experiment (Young, 1803) which demonstrates the wave-nature of light. The coherent beams from two slits interfere under certain conditions and produce fringe patterns on the detector plane. As the separation between two slits increases the fringes lose contrast. In LBI the two telescopes serve as two slits and the angular resolution of the stellar source is determined by the separation between the telescopes where the fringe contrast reduces to zero.

The angular resolution of the interferometer can be written as -

$$\theta = \frac{\lambda}{2b}, \tag{1.2}$$

where λ is the wavelength of the observations and b is the projected baseline. If a star is observed at 0.5 μm with a 100m baseline then a resolution of ∼0.5 milliarcsecond can be achieved. The quantity which is the measure of the fringe contrast is called visibility. For simple two slit experiment the visibility is defined as -

$$V = \frac{I_{max} - I_{min}}{I_{max} + I_{min}} = \frac{FringeAmplitude}{AverageIntensity}, \tag{1.3}$$

where I_{max} and I_{min} are the maximum and minimum intensity of the fringe respectively. In optical Long baseline Interferometry more than 100m of baselines are needed and the beams have to be combined coherently. It is difficult to make the stellar optical beams coming over such long distance to interfere. Good observing sites as well as sophisticated electronics for accurate path difference are necessary. Currently several optical long baseline interferometers are operated worldwide.

The historical developments and the individual projects of the LBI can be found elsewhere [Quirrenbach (2001) and Saha (2002)]. LBI in association with the adaptive optics (AO) is being used in Keck and VLTI (Very Large Telescope Interferometer). The giant interferometer VLTI, associated with AO, has seen the first fringe in 2001. The four unit telescope is also operational from 2002 at VLT paranal (Paresce 2003).

The observed visibility is modelled considering the source as uniformly illuminated disk. But it is also possible to model actual brightness distribution of the observed source. Uniform disk model for the structure of a complex source is an over simplification. But proper definition of brightness profile requires phase information of the source from the observed fringes. It is not possible to extract phase informations with two interferometers. Atleast three telescope interferometers are basic requirements to obtain phase informations of the source using the method of *closure* phase measurement. The *closure* phase is defined as the sum of the observed phases for the three baselines made by the three elements of the interferometer. The Fourier transforms give a complex quantity which contains both amplitude and phase informations. The amplitudes define the visibility of the fringe while its position is related to the phase. But due to the turbulent air, the fringes are dynamic in position and hence, single fringe can only give the information about the amplitude. With three or more telescopes the observed sets of fringes move but not independently. The phase information can be extracted from the relative position of the fringes. A few recent interesting studies on special objects are as follows − (1) Exoplanet candidate using Center for High Angular Resolution Astronomy ($CHARA$) array (Huber et al., 2012), (2) Gravitationally bound hierarchical triple systems with a very eccentric wide out orbit (De Becker et al., 2012) with $VLTI$, (3) Asymmetry in the disk shaped dust shell in Be Star/X-ray transient object CI Cam (Thureau et al. 2009) using Infrared Optical Telescope Array ($IOTA$) and Palomar Testbed Interferometer (PTI) can be found in the literature.

Also, recent spectro-interferometric study with $VLTI$ on the AGB variables, as discussed in Section.1.1, is providing the detailed information of their photosphere and atmosphere (Wittkowski et al., 2011). A similar investigation has been carried out later on Super-giants using $VLTI$ (Wittkowski et al., 2012).

1.3.2 Lunar Occultations

Lunar Occultations (LO) are among the most rapid of celestial events. When the moon moves eastwards at a relative velocity of about $0''.5$/sec relative to stars, many of them in the path of the moon get occulted and disappear behind the lunar limb and reappear after about 1 hour or less. The star light coming to the observer experiences straight edge diffraction at the sharp airless lunar limb. The diffraction pattern then sweeps across the telescope. A schematic diagram of the lunar occultation event is shown in Fig.1.4.

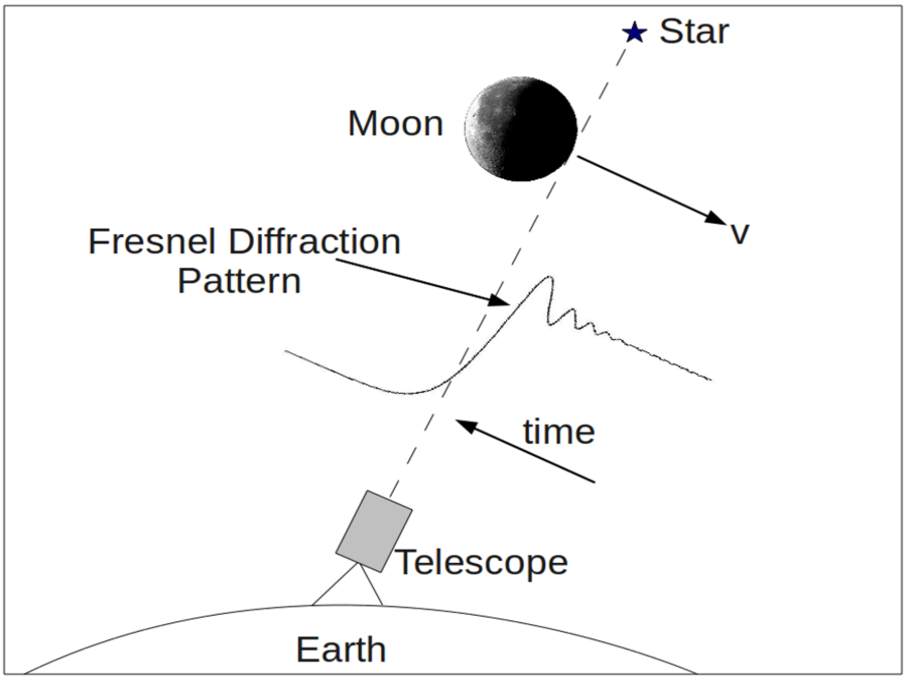

Figure 1.4: A schematic diagram of disappearance Lunar Occultation event as seen by the earth based telescope. Here, the telescope is tracking the star, not the moon.

1.3.2.1 History & Developments

The first mention of the lunar occultation goes back to Aristotle who had observed the LO of Mars in 357 BC and concluded that Mars is beyond the moon. The telescopic era of the lunar occultation started with Bullialdus who was first to observe an event through a telescope in 1623 AD. E.S. King first recorded a LO event on photographic film in 1898 at Harvard college. But the idea to determine the angular diameter of the occulted stellar objects using the LO was suggested by MacMahon (1909). However, MacMohan treated the problem with the methods of geometrical optics and hence, overlooked the diffraction effect the star light experiences at the sharp lunar limb. Eddington (1918) pointed out that the occultation is a diffraction process and it would mask the true diameter for all but the largest stars. Later Williams (1939) gave the theory of this diffraction in terms of the Fresnel's integrals and Whitford (1939) included the detector band-width in the theoretical calculation. In order to confirm their models, they also published the LO observations of β Cep and ν Aqr using high speed photosensitive photocells. Nather & Evans (1970) introduced the new technique of high speed digital recording and started the modern era of lunar occultations. The modeling of the LO light curves using the non-linear least squares was introduced by Nather & McCant (1970). A detailed historical outline of LO can be found in White (1987) and Warner (1988).

Lunar occultations have found wide application from X-rays to radio wavelengths. The observations of Lunar occultation of Crab Nebula in X-ray was carried out with the help of balloon based X-ray telescope by Ricker et al., (1975). Also spatial asymmetry in the X-ray flux distribution of the Crab nebula had been detected by Aschenbach & Brinkmann 1975. The reduction of errors in the positions of point like X-ray sources by LO had been performed by Born & Debrunner 1979. A study on the LO of the radio sources can be found in von Hoerner 1964 and Lyne 1972. A survey on 239 radio sources using LO at 327 MHz had been carried out by Singal (1987) using the Ooty radio telescope in India.

The observation of LO in the near infrared (NIR) was started in KPNO (Kitt Peak National Observatory) during 1974 using a single element InSb detector. Ridgway and his team measured many angular diameters using LO technique in the NIR (Ridgway et al., 1979 & 1982; Schmidtke et al., 1986). A further development in the NIR lunar occultation technique was carried out by Richichi and his co-workers at Arcetri observatory (TIRGO and Calar Alto telescopes) and then at ESO. Richichi (1989) introduced a model independent algorithm (MIA) in the model fit of the lunar occultation light curves which could reproduce the one dimensional brightness profile of the source to some extent.

The group at Physical Research Laboratory, India had started the Lunar Occultation program in NIR in early 90's with the availability of the 1.2m telescope as a flux collector at Mt. Abu. It has already produced three Ph.D. theses (Ragland 1996, Tej 1999, Mondal 2004). The group has used the model independent algorithm (MIA) on special sources like IRC +10216 & WR 104 and obtained good results (Chandrasekhar & Mondal, 2001; Mondal & Chandrasekhar, 2002). Earlier LO observations at PRL were carried out with an InSb fast photometer. The NICMOS HgCdTe sub-array is being used since 2007 to explore the high angular resolution capability of the LO using 1.2m telescope at Mt. Abu. **This thesis mainly deals with LO data of late-type giants obtained with NICMOS sub-array**.

The important fact in the success of the LO as HAR technique is that the fringes are produced near the lunar limb far beyond the earth's atmosphere. Also the distance between the earth and the moon is such that it is possible to sample the event in milliseconds. The observed fringes are treated as a convolution of diffraction patterns produced by many hypothetical point sources (discussed in Section.2.6). The fringes are smeared by many instrumental effects like – finite telescope aperture, finite filter band-width, system time response (for single element detectors). The simulated LO light curves for different uniform disk angular diameters in the NIR K-band (2.2 μm) assuming the lunar component velocity of 0.5m/msec is shown in Fig.1.5. It can be seen that no fringes are present for the extended sources (UD >20 mas) as diffraction patterns are merged and can be treated by geometrical optics.

The light intensity at any point of the diffraction fringes for a monochromatic point source can be written as -

$$F(\omega) = \frac{1}{2}\left[\left(\frac{1}{2} + C(\omega)\right)^2 + \left(\frac{1}{2} + S(\omega)\right)^2\right], \tag{1.4}$$

where C(ω) and S(ω) are Fresnel integrals and can be expressed as -

$$C(\omega) = \int_0^\omega cos\left(\frac{\pi t^2}{2}\right)dt, \text{ and } S(\omega) = \int_0^\omega sin\left(\frac{\pi t^2}{2}\right)dt, \tag{1.5}$$

ω is Fresnel number which is written as

$$\omega = \left(\frac{2}{\lambda d}\right)^{\frac{1}{2}} v(t - t_o) \tag{1.6}$$

where v is the component velocity of the lunar limb along the direction of the occultation, t_o is the time of geometric point of occultation where intensity

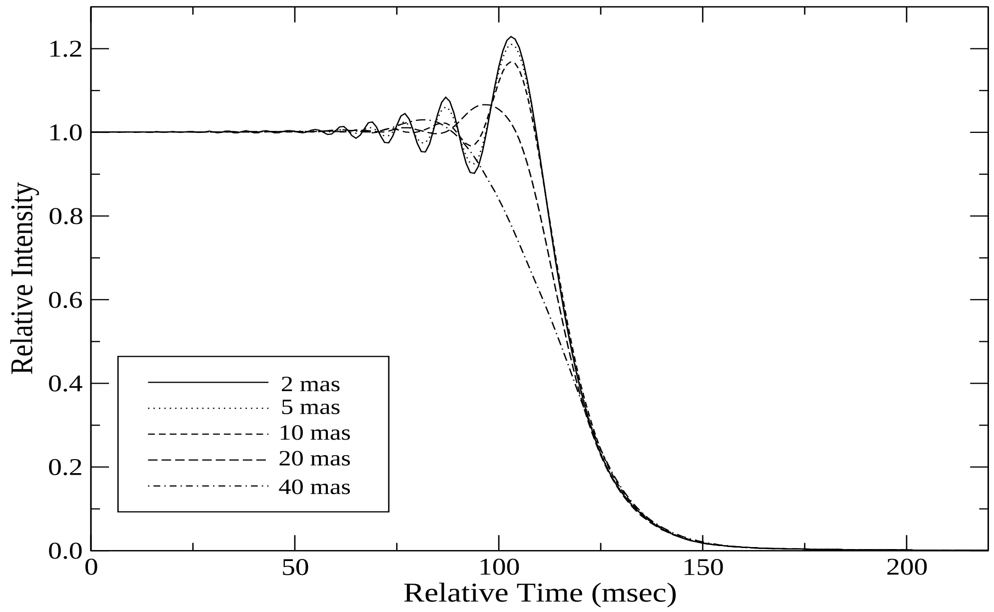

Figure 1.5: The simulated LO light curves for different UD angular diameters in the K-band assuming lunar velocity component of 0.5 m/msec. All the instrumental effects e.g. time response, filter bandwidth and telescope aperture (1.2 m here)are also taken into account.

of the source drops to 25% and t is any time, λ is the wavelength of the observations and d is the distance to the moon.

The maximum and minimum intensities in the Fresnel fringe occur at $\omega = \sqrt{(\frac{3}{2} + 4N)}$ and $\omega = \sqrt{(\frac{7}{2} + 4N)}$ respectively, where N = 0, 1, 2, ... etc. Assuming the distance to the moon as $3.8{\times}10^5$ km, component velocity v = 0.5 m/msec and the wavelength λ as 2.2 μm, it is found that the fourth maxima ($\omega = 3.67$) will occur at 150 msec before the geometric point of occultation. Hence, it requires fast photometry with millisecond sampling to acquire the proper LO light curve. The data duration of 1-2 seconds is adequate to model the light curve. It is difficult to record the LO fringes beyond 4^{th} maxima because of the noise level in the light curve.

The LO technique has been extensively utilized for its high angular resolution (HAR) capability in the visible and the NIR wavelengths. In the Catalog for High Angular Resolution Measurement (CHARM2 catalog; Richichi et al, 2005), a total of 6718 angular diameters determinations are reported and more than 5000 of them are late-type giants. Among them 1975 measurements are direct, including 1270 by LBI and 502 by LO. Though, the number of measured angular diameters has drastically increased in the last decade due to VLTI, Keck and other interferometers, the LO technique is still comparable to LBI in terms of milliarcsecond resolution and continues to provide useful scientific results with 1m class telescopes. In this thesis the use of a sub-array of a 2D detector array for resolving LO events is explored.

The main noise component in the LO light curves of bright objects (for m_K $\leq$3.5) is atmospheric scintillation modulating the source photon noise. Fainter source light curves are affected by the back-ground noise. It is difficult to remove the scintillation noise from the light curves because its frequencies nearly matches with the occultation fringe frequency. A polynomial is sometimes used to model this low frequency variation of the light curves. In this thesis, a process to improve the signal to noise ratio of the observed light curve using Fourier and Wavelet transforms has been tried out and is discussed in Chapter 5.

1.3.2.2 Advantages and Disadvantages

The optical LBI requires very long baselines, sophisticated electronics and also excellent sites (best seeing). In case of LO, fringes are produced far outside the earth's atmosphere and telescope merely serves as a light collector. It is not greatly affected by seeing considerations. The size and the distance to the moon is a lucky combination for the success of the LO technique. As explained by Richichi (1994) that nearer moon would have occulted many sources because of the increasing number of sources covered due to its larger angular size. But events would have occurred faster and hence, difficult to record with present instruments. If the distance to the moon had been more then LO events might be better sampled temporally but they would have been rare. Further a larger physical size of the moon would have led to a lunar atmosphere dense enough to smear out the fringes.

Lunar occultation as a technique has a few severe drawbacks. First of all, the sources are not the observer's choice. Observers can only predict for a event and record it accordingly. The limited lunar path covers only 10% of the total sky. Also deformations of the observed fringe patterns are sometimes seen due to unknown lunar slope which causes a variable component velocity of the moon along the direction of occultation. Also, the lunar occultation events are unique in terms of time and geometry. So, one needs to record the events at specific times only. Finally, any single LO event gives an one dimensional scan on the source. The repeated LO event of the same source, which rarely occurs, at different position angle or observations of the same event from different sites can reconstruct the 2-D image of the source to some extent.

It has been fortunate that lunar path covers a part of the highly dense Galactic centre region which is at the southern end of its declination swing (Declination :-29^o). The rare events towards the galactic centre are observed in the current Saros cycle from Mt. Abu observatory and are extensively discussed Chapter 3.

Tsuji had pointed out as early as in 1978 that it is difficult to study the photospheric diameter of cool stars in the visible wavelengths due to their scattering by the surrounded dust particles. In the visible bands scattered moon light is more than the NIR bands. On the other hand in mid-IR the moon itself is a bright source. Hence, good signal to noise (S/N) of the LO light curves are obtained in the NIR (1-5 μm) than in the visible region.

It can be seen from the Eqn.1.6 that $(t - t_0) \propto \sqrt{\lambda}$. So, the fringe spacing is wider by a factor of 2 in the NIR (2.2 μm) than the visible (0.5 μm). Hence, better spatial sampling of the LO fringes are obtained in the NIR than visible. Another advantage of LO observations is that being a very short duration event (1-2 sec), it can be successfully observed even if the weather conditions are not ideal i,e; partly cloudy but steady. In such cases though S/N will be reduced but event can be recorded successfully.

1.4 Layout of the thesis

The thesis comprises of six chapters.

Chapter 1 begins with a brief discussion on the evolution of late-type giants followed by an introduction to high angular resolution techniques. History and development of the Optical Long-Baseline Interferometry (LBI) and the Lunar Occultation (LO) technique are briefly covered.

Chapter 2 consists of details of the NICMOS sub-array used in LO observations and the description of analysis of LO light curves. A comparison between the earlier instrument, (the fast photometer) used for LO observations and the NICMOS sub-array detector, used in this thesis, has been made.

Chapter 3 details the study of the rare LO events towards the highly obscured and high stellar density galactic centre region, observed from Mt. Abu.

Chapter 4 describes observations of a few AGB variables observed from Mt. Abu. Further, a prediction method of UD diameter is developed using archival high angular resolution data and our own LO observations. The effect of the mass-loss on the uniform disk angular diameter measurements of AGB variables has also been examined.

Chapter 5 presents the study of the noise reduction method on the observed LO light curves using Fourier and Wavelet transforms, and a combination of the two. A description of types of noise encountered in LO light curves is also given.

Finally, summary of the present study and prospects for further work are outlined in **Chapter 6**.

Chapter 2

Instrumentation, Observations and Analysis

In this chapter the instrumentation used to observe the Lunar occultation (LO) events is described, the method of observations outlined and the analysis of the resulting LO light curves discussed. A comparison with an earlier version of LO instrumentation is also made. Almost all the LO sources presented in this thesis are observed with NICMOS (Near Infrared Camera and Multi-Object Spectrometer) sub-array operational mode.

2.1 Older Instrumentation

The earlier version of the LO instrumentation was a single channel fast photometer which has been later extended to a duel channel system for observing bright events in K (2.2 μm) and L (3.4 μm) filter bands simultaneously (Chandrasekhar, 2005). A single element InSb detector of 0.5 mm in diameter is housed inside a liquid nitrogen dewar along with filters, apertures etc. It has a wavelength response in the range of 1-5 μm. The preamplifier output from the detector could be sampled rapidly at 1 millisecond intervals. However, the detector system had enough sensitivity only to record the events of sources brighter than the Near infrared (NIR) K-magnitude (m_K) of 3.0. The Two Micron Sky Survey ($TMSS$) catalog (Neugebauer & Leighton, 1969) with

m_K ≤3.5 was used in the prediction program for the LO events observed by this photometer.

The number of sources in the lunar path (within the Declination of -30^o to +30^o) as a function of K-magnitudes upto m_K ∼6.0 existing in the 2MASS (2 Micron All Sky Survey) catalog is shown in Fig.2.1. A total 3,439 sources are present in the lunar path with m_K ≤3.0. This number rises to 29,221 for the magnitude limit of m_K ≤5.0. Using the NICMOS sub-array detector, occulta-

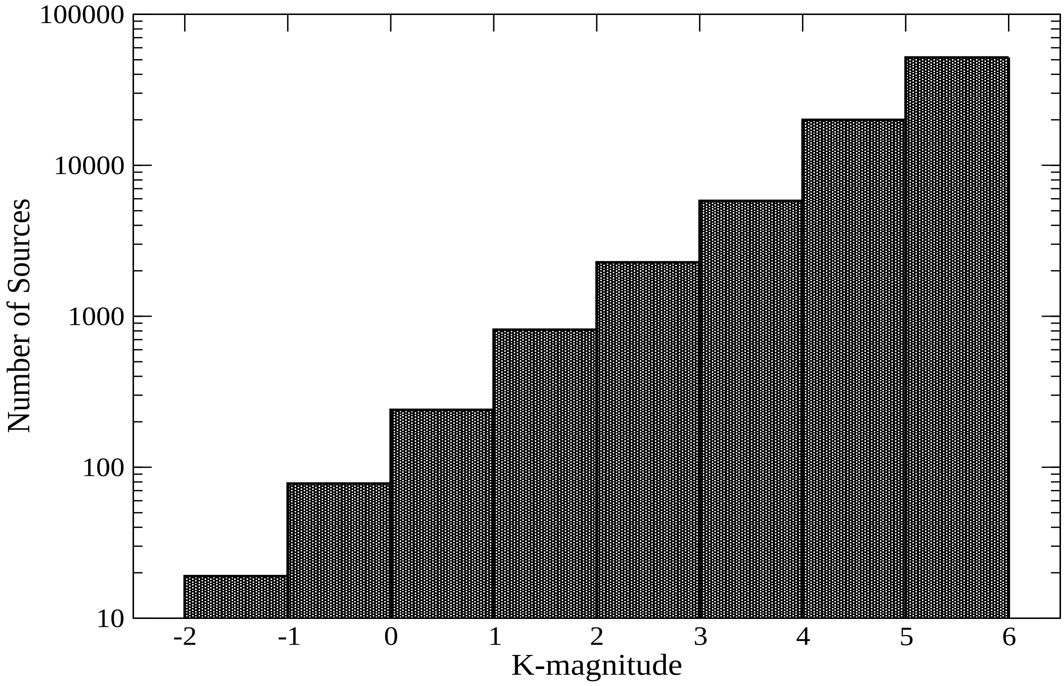

Figure 2.1: The number of sources in the lunar path increases sharply with K-magnitude (m_K). While the number of sources with m_K below 3 is few thousands, it rises more than 20,000 for magnitude limit m_K ∼ 5. All the sources are derived from 2MASS catalog.

2.2 NICMOS IR-camera

The NICMOS is serving as main IR instrument (Camera cum Spectrometer, named *PRLNIC*) at Mt. Abu observatory for more than a decade. The basic concept of PRLNIC was adopted from the NICMOS3 detector used in Hubble Space Telescope (HST). The detector is composed of 256×256 pixels Mercury-Cadmium-Telluride (HgCdTe) array. Each pixel is 40 μm in size. NICMOS array has a spectral coverage of 1 to 2.5 μm. The f/13 beam from 1.2m Mount Abu telescope focused on each pixel corresponds to $0''.5$ on the sky. Hence, the full-frame image (256×256 pixels) corresponds to a field of view of about $2' \times 2'$ on the sky. The detector and associated optics are kept in a dewar, cooled to liquid nitrogen temperature (77 K). The characteristic details of the array detector, collected from the NICMOS manual, are listed in Table.2.1. Photographs of Mt. Abu IR-observatory and the NICMOS camera attached to the telescope are shown in Fig.2.2 & Fig.2.3 respectively.

Table 2.1: Characteristic details of the NICMOS3 Camera attached to Mt. Abu telescope. (Ref. NICMOS manual)

Detector	256×256 HgCdTe
Wavelength Coverage	1-2.5 μm
Pixel size	40 μm
Read Noise	53 e^-
Dark Noise	$\leq$0.7 e^-/sec
ADC	32 bit
Bad pixels	~200
Total usable pixels	99.92%

The schematic diagram of the detector system is shown in Fig.2.4 & Fig.2.5. The f/13 beam from the 1.2 m primary and 0.28 m secondary mirrors, is directed to the detector systems. A beam-splitter, placed in between, reflects the visible wavelengths and transmits the NIR wavelengths. The reflected visible light is focused on the 'Auto-guider' CCD. The 'Auto-guider' system is used to correct the improper telescope tracking and guide on the source. The proper application of the Auto-guiding mode requires bright sources with $m_V \leq 7.0$ during the Lunar occultation observations. This is because during

Figure 2.2: Mount Abu Infrared Observatory, Rajasthan.

Table 2.2: Details of the cold Filters in two filter wheels inside the NICMOS IR-Camera. The filters used for LO observations in this thesis are marked in ***bold***.

Filter	Central Wavelength (μm) @77 K	Band-width (FWHM) (μm)
	Broad-band filters (Filter Wheel I)	
Block	–	–
J	1.25	0.30
H	1.66	0.29
K	**2.18**	**0.41**
$\mathbf{K}_S$	**2.12**	**0.35**
Block	–	–
Block	–	–
Block	–	–
	Narrow-band filters (Filter Wheel II)	
Block	–	–
FeII	1.65	0.04
H_2	2.12	0.04
Cont1	2.14	0.04
Br-γ	2.16	0.04
Cont2	2.22	0.08
CO	**2.37**	**0.10**
Open	–	–

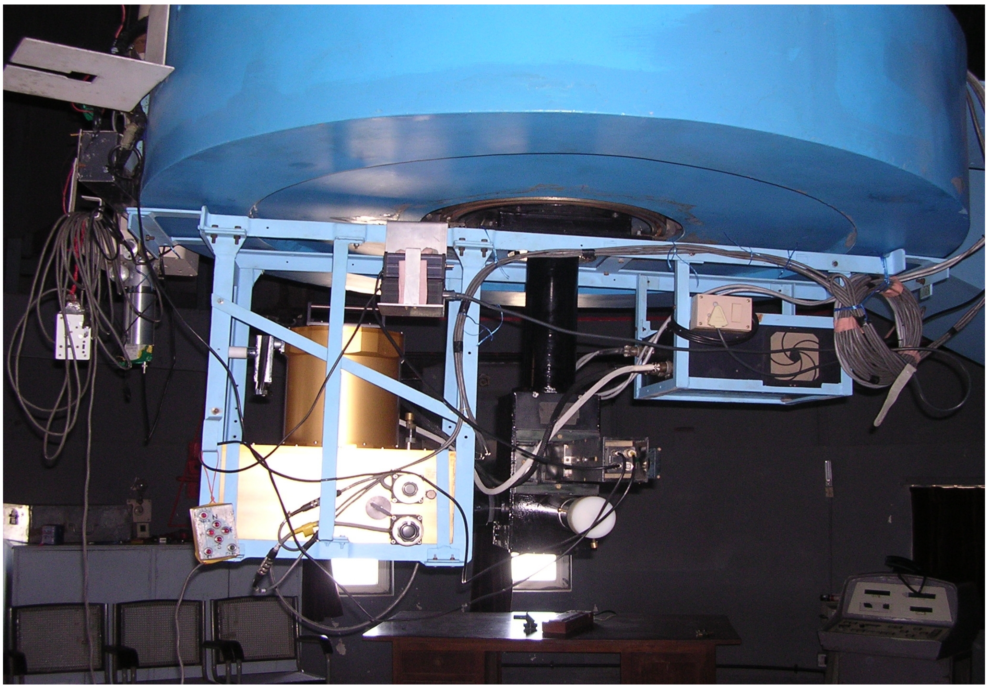

Figure 2.3: Near-IR Camera and Multi-Object Spectrometer (NICMOS) named PRLNIC (golden in colour) attached to the back-end of Mt. Abu telescope.

the LO events the back-ground level in the detector increases due to the scattered light from the moon and it is difficult to register sources with m_V >7.0 usually in the auto-guider CCD. But our natural choice of LO sources are cool late-type giants for which the Auto-guider generally could not be used during many of the LO observations. We recorded the LO events of SAO 109252 (m_K ∼3.74 & m_V ∼6.98; Alt. ∼ 74^o) on January 11, 2011 and SAO 77915 (m_K ∼2.18 & m_V ∼4.15; Alt.∼ 22^o) on January 17, 2011 keeping the telescope in 'auto-guiding' mode. In both the cases good light curves have been obtained. Though, both the sources are unresolved with our system, the binary components of the source SAO 77915 have been detected. Sometimes the corrections to the telescope position from the 'Auto-guider' system results in telescope oscillations and it is seen in one fainter (in V-band) object, SAO 75706 (m_K ∼3.71 & m_V ∼8.38; Alt.∼ 34^o) during the LO event on January 14, 2011.

After the beam-splitter, the telescope beam is directed to the liquid nitrogen (LN_2) cooled dewar by 45^o gold coated mirror. NICMOS has an effective field of view (FOV) of $2^{'}\times2^{'}$ which can be transformed to $4^{'}\times4^{'}$ using the 'Focal Reducer' switch. The 'Focal Reducer' system contains a plano-convex lens. Sliding the plano-convex lens in the path of the f/13 beam converts it to f/6.5 and hence, alters the effective FOV from $2^{'}\times2^{'}$ to $4^{'}\times4^{'}$. Normally, the $2^{'}\times2^{'}$ FOV is only used as it provides the best imagery. Also it is not possible to switch between the two fields of view when the dewar is in cold condition. Two filter wheels are present inside PRLNIC, one is to accommodate the NIR broad-band filters and other is for the narrow-band filters. The details of all the filters are listed in Table.2.2. In the lunar occultation observations, the broad K- & K_S- and narrow CO-band filters are only used depending on source brightness and characteristics. Inside the cold dewar after passing though the focal reducer and filters, the beam is focused at the cold aperture and then collimated towards the 'Mirror/Grating' assembly. One side of the 'Mirror/Grating' assembly has a plane mirror while the other side has a reflection grating. Hence, 180^o rotation of it changes the mode of the detector system from imaging to spectroscopic or vise versa. After reflecting from the 'Mirror/Grating' assembly the beam is refocused on the detector by the camera mirror (deflection) and a 45^o mirror.

The NICMOS is operated with a DOS-based system. The old hardware system associated with NICMOS also does not allow to operate it with 'Windows' based operating system which could have made the observation process easier. The block-diagram $PRLNIC$ is shown in Fig.2.6. The pre-amplifier output from the detector is transferred to the *upper* electronics box. The analog to digital conversion (ADC) of the collected electron charges occurs in the upper electronics box kept near the detector system. The digitized signal from the *upper* electronics box is transmitted to the *lower* electronics box in the control room via optical fibers. The lower electronics box is connected to NICMOS computer where the observed data are saved to disk, along with header files which contain the GPS (Global Positioning System) time informations collected from the telescope control system.

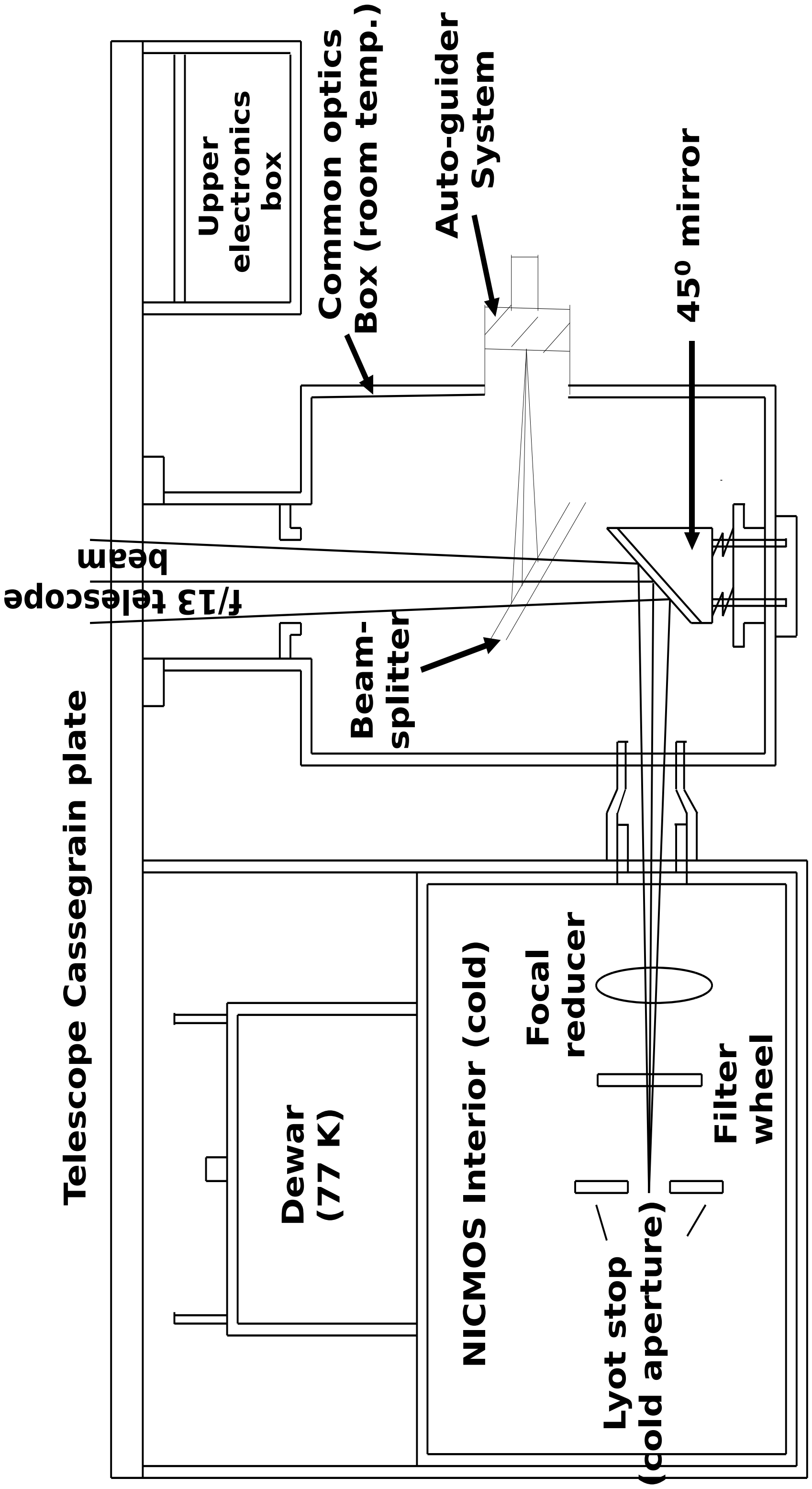

Figure 2.4: Schematic diagram of the optical system coupled with the 1.2 m telescope at Mt. Abu Observatory (Not to scale).

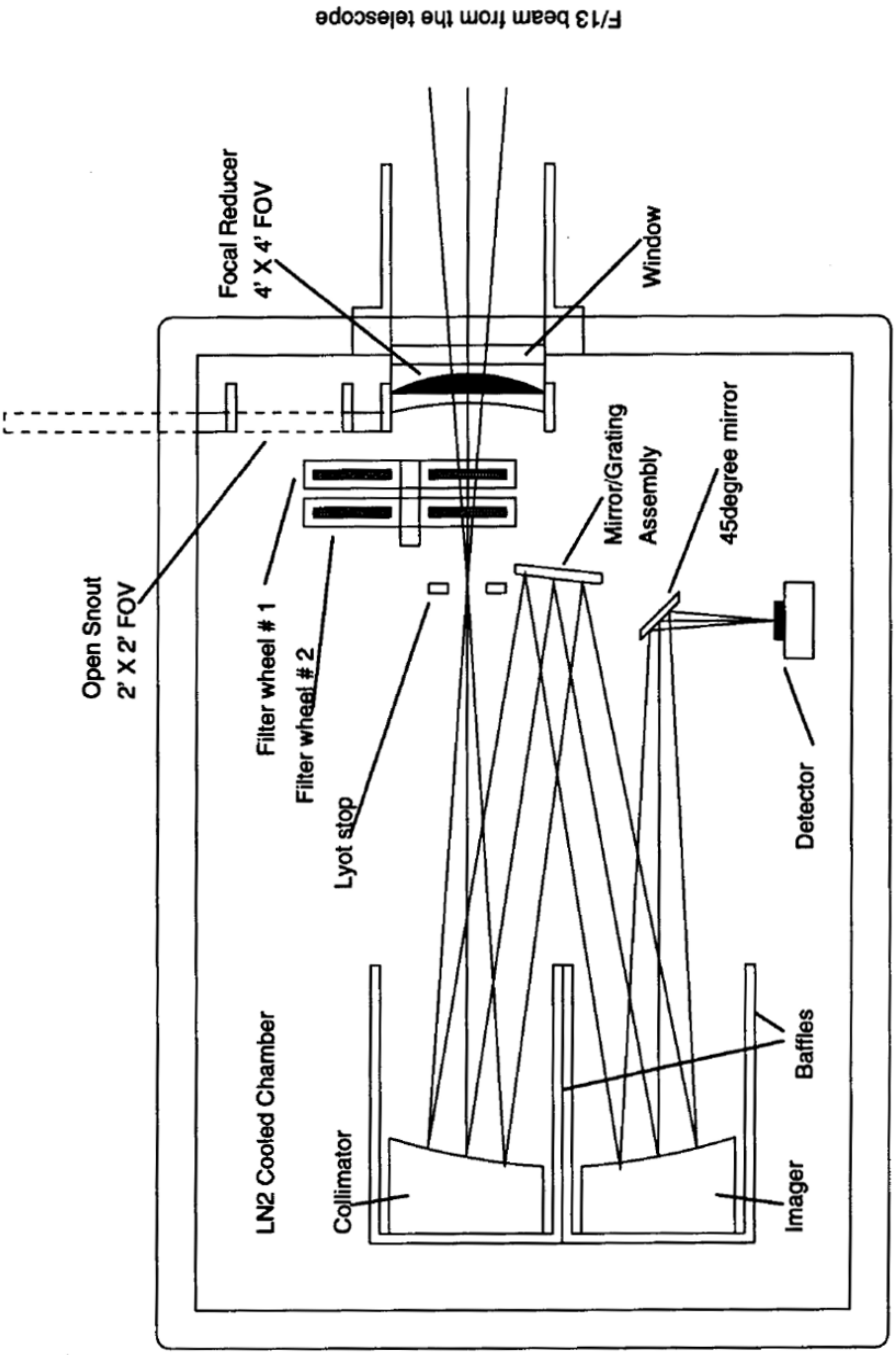

Figure 2.5: Schematic diagram of the optical system inside NICMOS dewar (Nanda Kumar, M. S., 1999).

2.2.1 Imaging with NICMOS

The full frame imaging of the NICMOS camera requires two input times - one for integrating the signal counts (*integration time*) and another to 'reset' the array (*reset time*). The data acquisition process also includes an electronic dead time, when the collected electron charges are transferred from the array to the detector electronics and readout. The sampling time of a frame acquisition is composed of 'reset', 'integration', and the electronic 'dead time'. The full frame imaging is performed using a technique called "Correlated Double Sampling" (CDS). In this method the signals in the pixels are digitized twice - once (A-frame) during the reference level period (just after 'reset' the array) and again after the integration of the signal (B-frame). The difference between them is then performed digitally to remove the previous residual counts from the new frame (D-frame). For illustration the A, B and D-frames with Jupiter images are shown in Fig.2.8. The upper-left image is the A-frame and upper-right figure is the B-frame. The lower image is the subtracted (B-A) frame (D-frame). NICMOS has a provision to save all three, A, B and D-frames in slow mode (full-frame). But generally the D-frames are only saved during the photometric observations.

An average of about 33,000 counts per pixel has been measured in the 'raw' images (A & B-frames) even if they are exposed to the liquid nitrogen temperature (77 K) in the closed filter conditions. The average count level increases a little when it is exposed to the sky. But inspite of the very large detector background ($\sim$ 33,000/pixel) present in the A and B-frames, it is possible to extract a small star signal of a few tens of counts per pixel by taking the difference between them. This is because the large average counts in the A and B-frames can be treated as a large but steady off-sets.

Now, it can also be observed in the 'raw' frames that vertically fringe like patterns are present in the images (upper two in figures Fig.2.8). They have alternative bright and dark rows and columns (faintly seen). This pattern is present even when the detector is exposed to LN_2 temperature. However, these fringe like patterns are completely removed in the subtracted images (lower image in Fig.2.8). It is found that the difference between the consecutive bright and dark columns have an average standard deviation of about 8 counts only, which is much less compared to the huge back-ground ($\sim$ 33000) counts. Further positions of the bright and dark columns do not change from frame to frame which makes it possible to remove the patterns completely in the subtracted frames. Also low standard deviation implies that the noise contribution due to large detector back-ground at 2.2 μm is very less due to the subtraction process. As the subtracted (D-) frames are only saved during the full-frame observations in the NICMOS computer, so the acquired images are already processed to free from all these effects.

2.3 NICMOS Sub-array

The imaging of the NICMOS full array (256×256 pixels) has an inherent limitation in integration time. A minimum 'integration' of 60 msec and corresponding 'reset' time of 60 msec, are essential to record a usable full frame. But recording of proper LO light curve demands for sampling in milliseconds. Hence, experiments were performed to study the minimum sampling times possible with sub-arrays in NICMOS.

2.3.1 Sub-array Mode: Experiments

Table 2.3: The details of the sub-array experiments.

Sub-array Size (pixels)	Integration Time (msec)	Reset Time (msec)	Sampling Time (msec)
20×20	3.0	3.0	13.958
15×15	3.0	3.0	10.625
10×10	3.0	3.0	8.926
7×7	3.0	3.0	8.125

As the NICMOS full (256×256 pixels) frames are not suitable to record

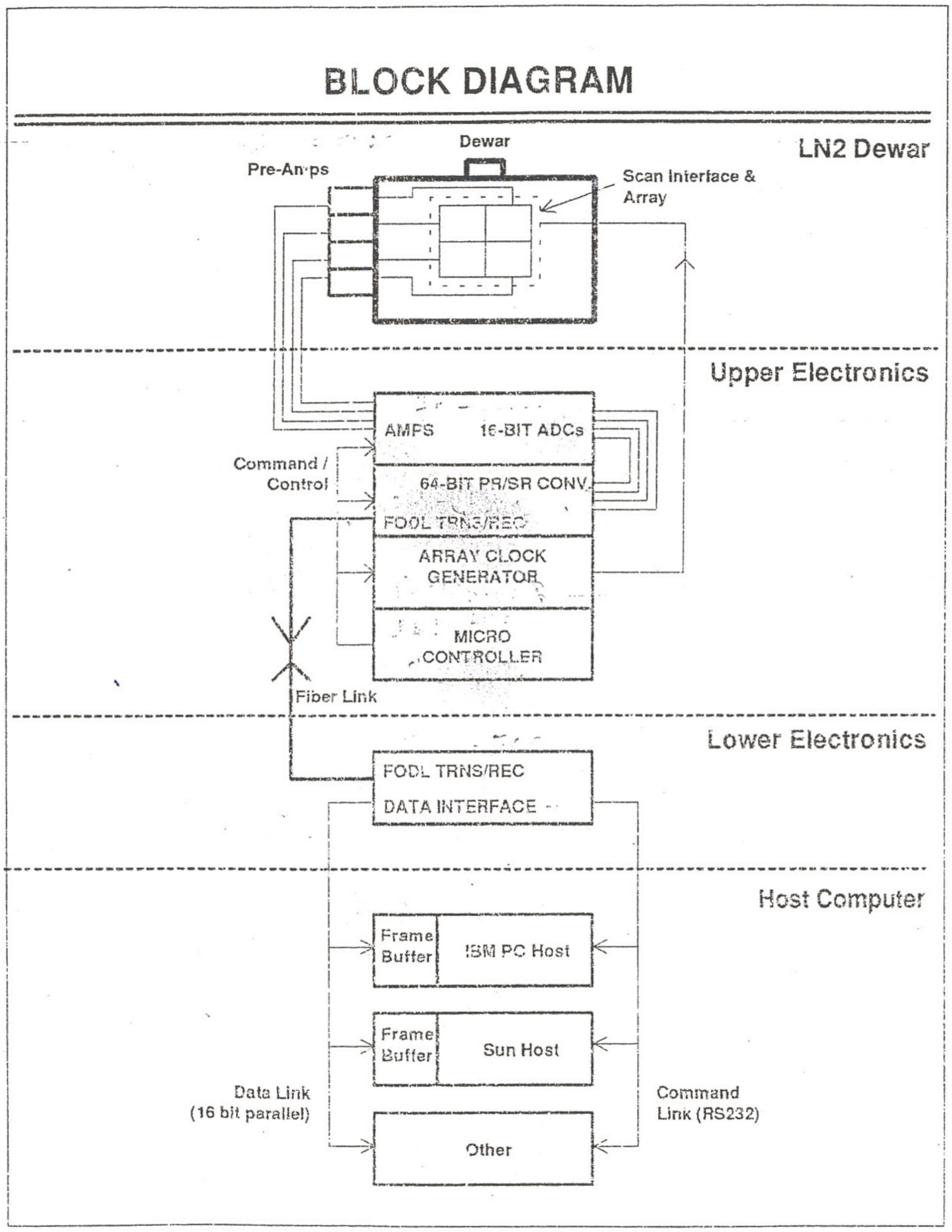

Figure 2.6: NICMOS Electronics Block diagram

the LO events, reduction of sampling time by choosing an Area of Interest (*AOI*) sub-array within the full array has been studied. *AOI* software had to be specially written in house and integrated with array operations. The name *AOI* is given because the sub-array can have different sizes as well as different positions inside the full frame. Our choice of the sub-array is such that the bad pixels are kept out of this sub-array. The first use of the sub-array mode in this camera was with 20×20 pixels with the present NICMOS array was reported by Chandrasekhar, Shah & Mondal (2003). They reported a sampling time of 15.8 msec for an integration time of 3 msec. However, recent modifications in the software of the detector electronics system have reduced the sampling time to 13.958 msec for 20×20 pixels sub-array. To reach the critical time limit

Table 2.4: The details integration and sampling times with 10×10 pixels sub-array.

Integration Time (msec)	Reset Time (msec)	Sampling Time (msec)
1.0	1.0	6.250
2.0	2.0	7.500
3.0	3.0	8.926
4.0	4.0	11.042
5.0	5.0	12.917

as well as the sub-array size many trials have been carried out with 20×20, 15×15, 10×10 and 7×7 pixels sub-arrays. The changes in sub-array sizes are made by modification of the NICMOS data acquisition scripts. The NICMOS sub-array operational script is written in *C*-language. The full script has a length of 3868 lines. The part of the script where the changes have been made to examine different sub-arrays is given in the Appendix A.

The summary of the study on sub-arrays is listed in Table.2.3. All the studies have been performed with equal integration and reset times. Reset times less than integration times lead to incomplete removal of charges from the detector and hence, errors. It can be seen that the sampling times are reduced for smaller sub-array sizes, but not drastically. The inherent restriction of electronics dead time limits the reduction of sampling times. It is not possible to go below 3 msec integration.

The 20×20 and 15×15 pixel sub-arrays are not presently being used in regular LO observations because of their much longer sampling times. The 7×7 ($3''.5 \times 3''.5$ on the sky) pixels sub-array has a little lower sampling time that 10×10 sub-array and can accommodate *seeing* limited stellar image in the best 'seeing' conditions ($\leq 1''$) at Gurushikhar. But it is not used in regular LO observations because of the difficulties to retain the star images within the sub-array, particularly when the star image drifts due to minute telescope oscillations or low altitudes and jerks in tracking due to heavy wind. Hence, it is found that the 10×10 pixels sub-array is the best to record the LO events in present condition. Most of the LO events in this thesis have been observed with 10×10 pixels sub-array with a mean sampling time of 8.926 msec. Attempts to reduce integration time to 1 msec was also not successful. The sampling time is deduced by auto-recording 'start' and 'stop' times of the run consisting of 4800 frames and is accurately known. Recent modification in the acquisition program is able to write GPS (Global Positioning System) UT times in the header file for both start and stop of the recording. It provides the third decimal accuracy of the milliseconds sampling time. No attempts to record the occultation event with absolute accuracy of 1 millisecond or better is made though it is inherently possible. Though 10×10 sub-array is normally used for LO events, but for special events like LO of known close binary stars or asteriods occultations, the 20×20 sub-array is used to accommodate both the components. One source in this thesis (IRC +20177) which has a visual binary component (Separation 700±50 mas) was observed with 20×20 pixels sub-array to accommodate both the components.

2.3.2 Patterns in the sub-frames

The typical 'raw image' of the 10×10 and 20×20 pixels sub-arrays are shown in the Fig.2.9. Both of them show the vertical fringe like patterns which have also been observed in the full 'raw' frames. The subtraction of two images (before integration and after integration) during the acquisition itself (as discussed for full-frames) requires an additional electronics dead time. But the lunar occultation demands fast sampling and hence, any unnecessary time consuming procedure is to be minimized during the recording of events. Therefore, the raw frames (B-frame), which have fringe like patterns, are only saved in the sub-frame mode of the NICMOS camera. It is also observed in Fig.2.9 that the last columns of both the sub-array images are darker as seen in the last column of each quadrants in the full 'raw' frames (upper images in Fig.2.8). But they appear in all the frames similarly and almost with same statistical differences respective to the other columns in the image. Hence, those effects are also completely removed along with the vertical patterns in the subtracted frames which is clarified in the next paragraphs.

The upper-left image in the Fig.2.10 shows a 'raw' 10×10 pixels sub-frame of the source HD 249571 ($m_K = 4.5$) during its LO event on March 13, 2011. The image of the star cannot be seen as the star counts are buried under the huge stationary background level($\sim$ 33,000 counts). The upper-right sub-frame is a sky frame acquired after the same event. This also looks similar to the previous one. The lower sub-frame is after subtraction of the sky frame (upper-right) from the first frame (upper-left). Here star image is clearly visible.

To examine the effect of the subtraction process on LO light curves, we also generated the light curves (event of HD 249571) from both 'raw' sub-frames as well as 'sky subtracted' sub-frames (Fig.2.11). The mean counts/pixel of each sub-frames are used to generate the light curves. The upper one represents the light curve generated from 'raw' sub-frames, while the lower one is derived from the 'sky subtracted' sub-frames. It can be seen that both the light curves are identical except a shift of about 33,930 counts. So, this implies that the huge backgrounds in the raw frames are stationary in nature and they are

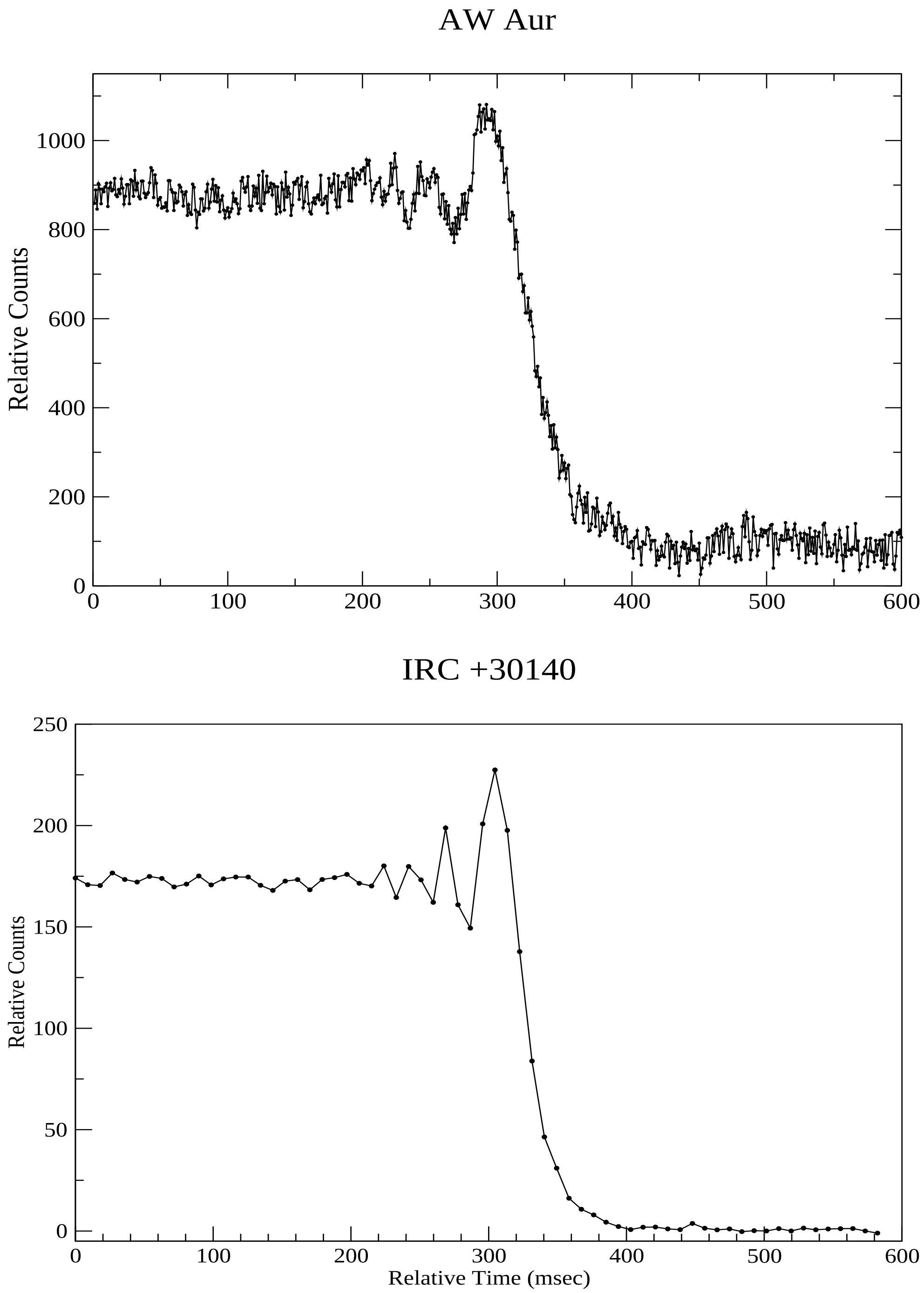

Figure 2.7: Comparison of light curves of photometer and NICMOS sub-array. Upper figure is the LO light curve of AW Aur (m_K = 2.34) recorded using the fast Photometer with a sampling time of 1 msec and lower figure is the light curve of IRC +30140 (m_K = 2.70) recorded using NICMOS sub-array with a integration time of 3.0 msec. The source AW Aur has a S/N∼12 compared to 35 for IRC +30140.

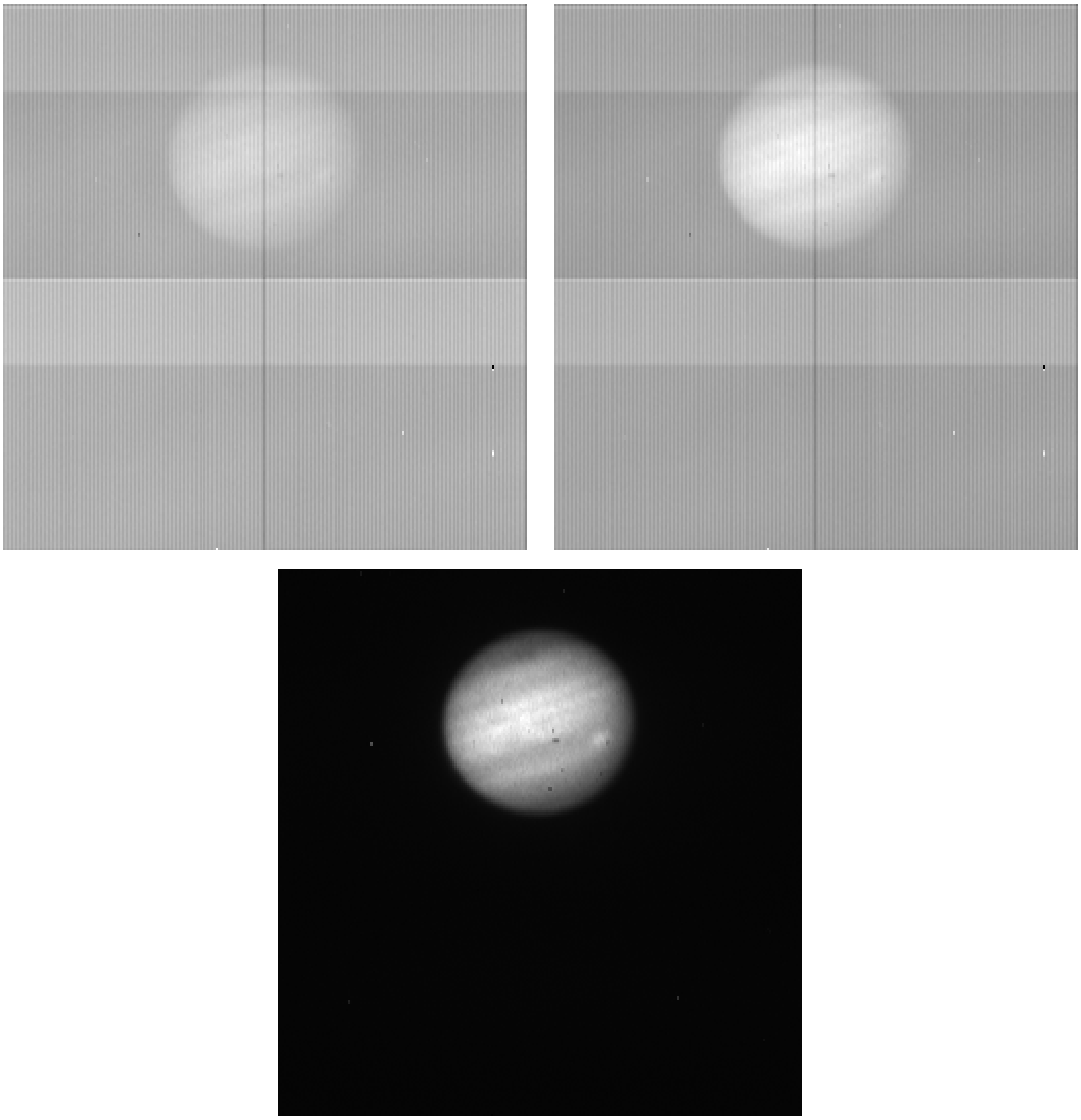

Figure 2.8: Raw frames with Jupiter's image after reset and before integration or A-frame (upper-left) and after integration or B-frame (upper-right). The back-ground patterns are clearly visible in the A-frame. The lower figure is the subtraction of the A-frame from the B-frame and represents the corresponding D-frame. The fringe like vertical patterns are visible in the two upper images but it has been completely removed after subtraction. These full frame NICMOS images are recorded in a narrow Br-γ band (2.16 μm/ BW 0.04 μm) with an integration time of 65 msec and the corresponding reset time is 65 msec.

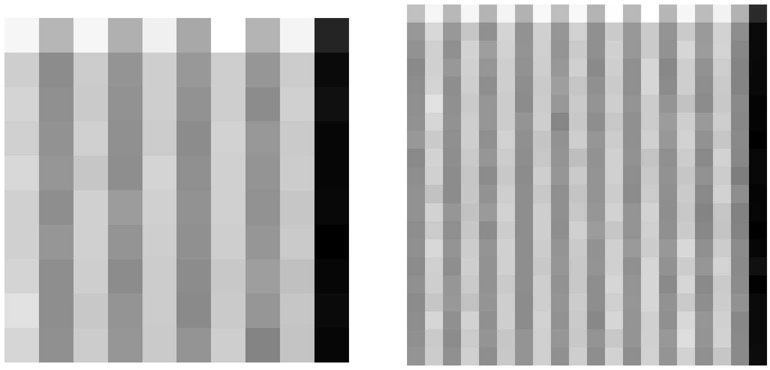

Figure 2.9: Raw Sub-frames of 10×10 pixels (left) and 20×20 pixels (right). Both the sub-frames show alternative patterns (bright and dark strips) which were observed in the 'Raw full frame' also (Fig.2.8).

completely removed in the subtraction process without any distortion of the light curve. Linear response of the full NICMOS array in NIR K-band has been studied upto ∼11,000 sky subtracted counts/pixel with an integration time of 1 sec. The response of the detector is fairly linear in this count range (0 − 11 000). In LO mode a maximum of ∼1200 counts/pixel is obtained in this thesis, for the source RT Cap (m_K ∼0.5) which was observed in presence of day light with an integration time of 3 msec. So, saturation effect is unlikely to occur in LO mode.

2.3.3 Comparison of NICMOS sub-array with Fast Photometer

It has already been discussed that the fast photometer is capable of observing any LO event with sampling time down to 1 msec. But the fast photometer has the inherent limitation on the brightness of the observable source. It can observe only sources with $m_K \leq 3.0$. On the other hand 10×10 pixels sub-array has coarser sampling compared to the fast photometer but capable of recording LO fringes of sources with $m_K \leq 5.0$. The example LO light curves observed with the fast photometer (up) and NICMOS sub-array (down) are shown in Fig.2.7. The light curve of the source AW Aur (m_K ∼2.34) was recorded using the fast photometer with a sampling time of 1 msec and it has a Signal to Noise ratio (S/N) of 12. While the similar magnitude source IRC +30140 (m_K ∼2.70) was observed in 10×10 pixels sub-array with integration time of 3 msec and has a signal to noise ratio (S/N) of 35. So, the higher S/N is achievable with NICMOS sub-array than fast photometer. The 1σ detection limit (i.e, S/N ∼ 1) of LO light curves, observed using NICMOS sub-array with an integration time of 3 milliseconds is $m_K \sim 6.5$ under best sky conditions. This is nearly in accordance with expectations using 1.2 m telescopes. According to Richichi et al. (1994), S/N of ∼50 is achievable on a m_K ∼6.0 source observed with 2 msec integration using 1.5m telescope in best sky condition. The successful recording of the LO fringes, however is possible with 1.2m Mt. Abu telescope, for sources upto magnitude of m_K ∼5.0 with a S/N ∼20.

Almost all the light curves used in this thesis are observed using NICMOS sub-array except three (discussed in Chapter 4). Those three light curves were observed earlier with fast photometer at Mt. Abu. Observations of the rare LO events towards the Galactic centre, in which most of the sources are fainter than m_K ∼4.0, were only been possible because of fainter detection limit of the NICMOS sub-array. Further fast switching (∼ 3 min) between two occulting sources with the fast photometer would not have been possible.

As mentioned in Section.2.1, in case of the InSb photometer (earlier system) faster sampling (upto 1 millisec) is possible for brighter sources ($m_K \leq 3$) but the system time response has to be taken into account explicitly in the analysis. While in case of the sub-array the time response function can be neglected in the model fit. Point source LO light curves obtained by the two modes of operation (fast photometer and sub-array) are shown in Fig.2.12 along with fitted model curves. Insets in the figure show error curves indicating the level of angular resolution achievable. Typically the limiting resolution of the technique with sub-arrays is about 3 milliarcsec though single element detector operation can do slightly better for bright sources ($m_K \leq 3$).

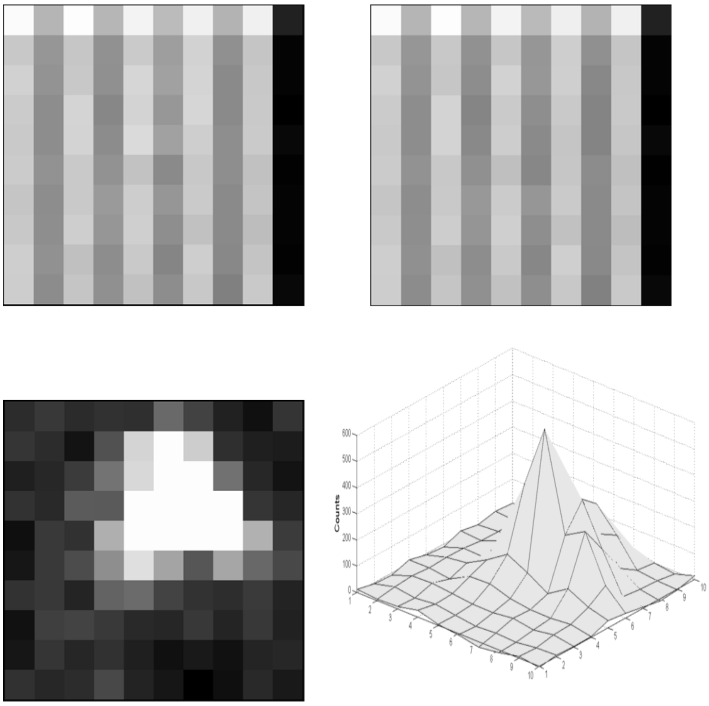

Figure 2.10: Upper-left is a raw sub-frame of LO event of the source HD 249571. The (star+sky) signal is buried in the huge back-ground of ∼33,000 counts/pixel. The upper-right sub-frame is the 20 frames averaged sky, observed after drifting to the nearby sky (discussed in Section 2.5) during the recording of the event. Lower-left sub-frame is the sky subtracted frame and the star is visible inside the frame and lower-right is the its 3D representation.

2.3.4 Sub-array detectors for LO observations by others

Use of the NICMOS sub-array to record LO events by other group can also be found in Richichi et al. (1996). It was operated in TIRGO observatory, Switzerland. They performed LO observations with 16×16 pixels ($16'' \times 16''$) sub-array and achieved a sampling time of 8 milliseconds (msec) for an integration of 7 msec. The sampling time of 20 msec was obtained with the sub-array of 32×32 pixels. The sub-array mode had been operational since October, 1995. In a period of 5 months they recorded 30 LO events.

Extensive use of sub-array operational mode in VLT is found in Richichi et al. (2008a, 2008b). They have used the Aladdin detector of ISAAC instrument

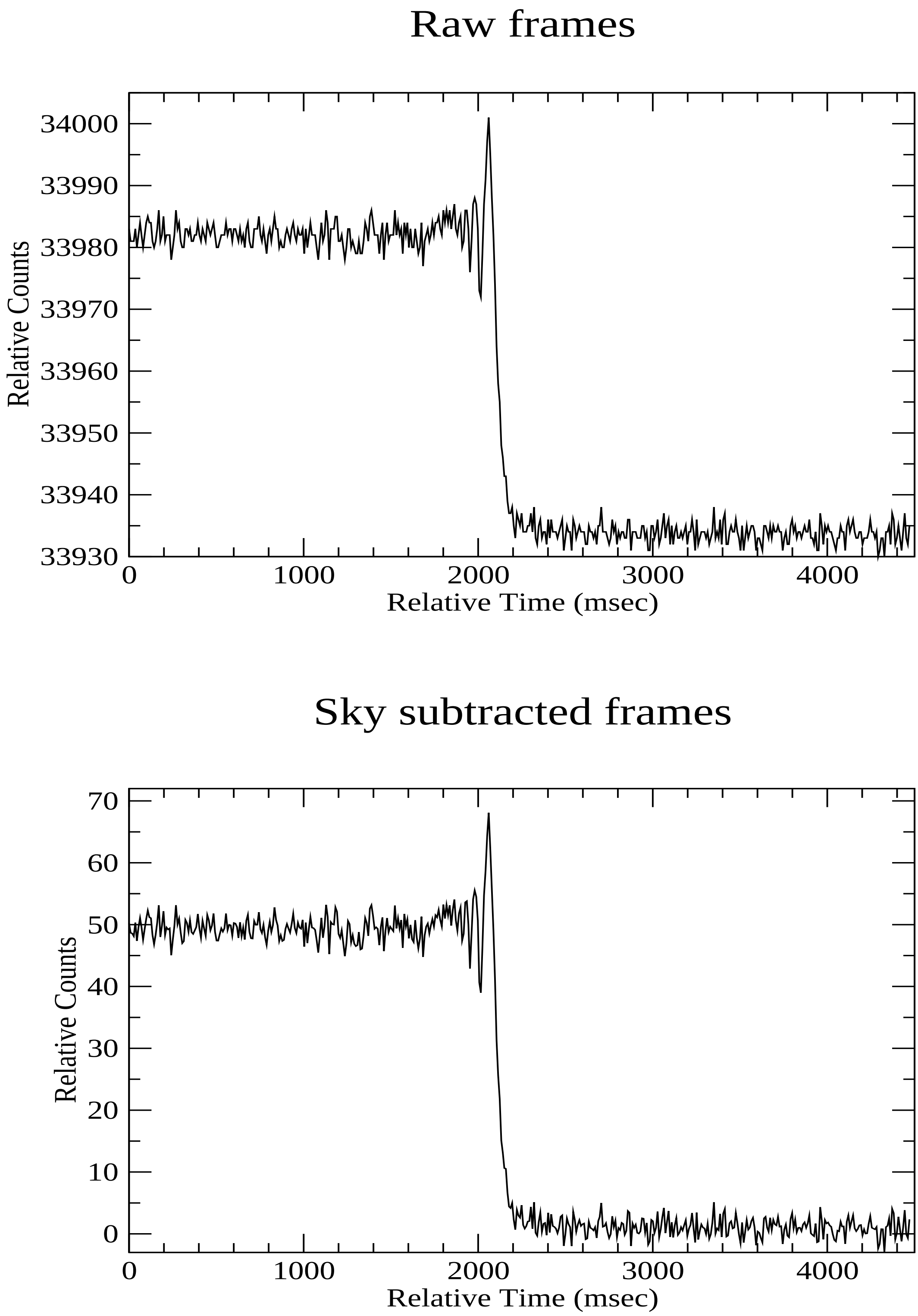

Figure 2.11: Both the light curves represent same event of HD 249571 observed on March 13, 2011. The upper one is generated from the raw frames while the lower one is generated from the sky subtracted frames. There is no detectable difference in the relative counts of the light curve showing thereby that detector back-ground at 77 K and is a steady level with very low fluctuations as discussed in text.

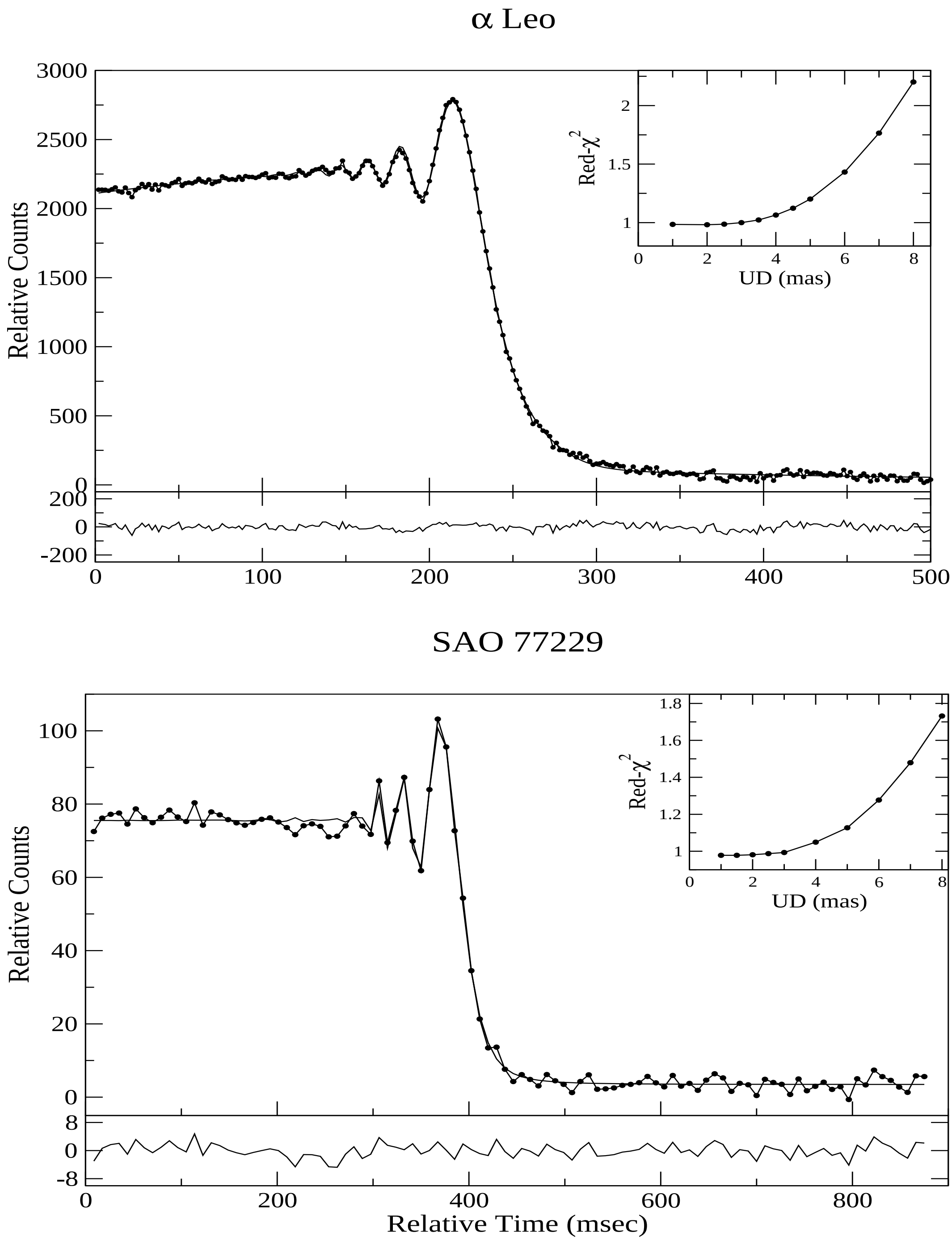

Figure 2.12: Model fits to light curves of point sources observed by the two different detector systems. The light curve of α Leo was obtained using fast photometer while the light curve of SAO 77229 was recorded with NICMOS sub-array. The inset shows the error curve of the UD angular diameter determination and the lower panel shows the residuals (data − model) of the best fit. The S/N for α Leo (K = 1.6) light curve is ∼100 and the same for SAO 77229 (K = 3.9) is ∼40. The limit of resolution in both the cases is ∼3 mas.

in a specially devised burst mode to record numerous Galactic centre events in a smaller time span using 8m VLT. Two modes of sub-arrays were used to record events – (1) 32×32 pixels ($4''.7 \times 4''.7$) with an effective sampling time of 3.2 msec, and (2) 64×64 pixels ($9''.5 \times 9''.5$) with an effective sampling time of 6.4 msec. They recorded a total of 129 events in two subsequent runs in a total time span of about 13 hrs. The use of this burst mode again can be found in Richichi et al., 2011. They observed a total of 184 LO events on September 25 & 26, 2009. We also observed several rare LO events towards the Galactic centre in a time span of about 4 hrs using 10×10 pixels sub-array operational mode of NICMOS camera. They are presented in next chapter.

2.4 Prediction of the LO events

Predictions for the LO events are made for Mt. Abu observatory at Gurushikhar (Long: 72^o $46'$ $47''$ E; Lat: 24^o $39'$ $09''$ N; Altitude: 1680m above mean sea level). Earlier the Two-Micron Sky Survey (TMSS) catalog (Neugebauer & Leighton, 1969) was used to predict the events observed with fast photometer ($m_K \leq$3.0). But NICMOS sub-array has a capability to go beyond $m_K \sim 3.0$. A modified version of 2 Micron All Sky Survey (2MASS; Cutri et al., 2003) catalog is being used in the prediction program. The 2MASS catalog includes sources with 3σ limiting sensitivity of $m_K \sim$15.3. The Lunar path is restricted to the zodiacal belt. Hence, a subset catalog has been generated which includes the sources within the Declination limit of -30^o to +30^o. Only sources brighter than $m_K \sim$6.0 are used in the prediction program. This catalog contains 188 517 sources with $m_K \leq$6.0. The generated subset catalog with sources brighter than $m_K \sim$6.0 has 80 934 sources. In the prediction program the daily lunar polynomials from 'The Astronomical Almanac' (online version) are given as input for exact Geocentric coordinates of the moon for every instant. Prediction for the event is computed using the topocentric coordinate of the moon for Mt. Abu observatory and the updated coordinates of the star for the day of the event by taking into account 'precession' and 'proper motion' of the star. The LO events generally found to occur within ±2 seconds of the predicted event time. The error in the time could be due to incorrect position of the source which may be because of unavailability of 'proper motion' measurements. SIMBAD source query is used to get J2000 coordinates and 'proper motion' values. After the execution of the prediction program the $SIMBAD$ database is again searched for the details of the sources (Spectral type/class, references, etc). Important sources are shortlisted for telescope time request and subsequent observations.

2.5 Recording of the events

Typically, an event run with NICMOS sub-array consists of a total of 4800 sub-frames. In case of disappearance events, first the star is identified and the telescope is pointed to the source properly. Then the star image is maintained inside the 10×10 pixels sub-array and monitored in *continuous display* mode of the NICMOS IR-camera with an integration time of 100 msec. This is required because the star image may drift out of the small sub-array due to improper telescope tracking, particularly at lower altitudes. Corrections for the drift is done manually or by auto-guider till 2 minutes before the predicted event time. About 2 minutes before the predicted event time, we come out of the *continuous display* mode and initiate the sub-array for data acquisition process with 3 msec integration and 3 msec reset time (corresponding sampling time is 8.926 msec). It takes 30 seconds to initialize the 10×10 pixel sub-array for data acquisition. The recording of the sub-frames starts 21 seconds prior to the predicted event time. It takes about 43 seconds to record 4800 sub-frames. After recording of 4500 frames, the telescope is rapidly switched to the east (in case of disappearance) by about 1 arcminute to record a few sky frames. Then the sky subtracted sub-frames are used to generate the light curve.

First, 20 good sky frames are selected from the end part of the light curves and then averaged out. The averaged sky frame is subtracted from all 4800 sub-frames using $IRAF$ interface (command: *imarith*). The mean counts per pixel (or total counts in sub-array) for each sub-frames are calculated (*IRAF* command: *imstat*). The plot of the 'mean counts per pixel' (or the total counts) in each of the sub-frames against the time represents the light curve.

In the case of reappearance event we have to observe a source which is coming out of the lunar limb and hence, it cannot be seen even when the recording is started. A near by guide star is chosen for monitoring which is not going to be occulted. A test of the switching performance of the telescope between the guide star and the program star is usually done one day before the event at approximately same altitude, and the required offsets in the coordinates (if any) are noted down. About 3 minutes before the predicted event time, the telescope switched to the program star, which is behind the lunar limb, along with the required offsets (noted on the previous day). About 2 minutes before the predicted event time we come out of the *Continuous display* mode and follow the same procedure as mentioned above in the case of disappearance events. Here, the sky frames are recorded by moving the telescope to the west after recording of about 4500 sub-frames.

All the LO events reported in this thesis are disappearance events except one (CW Oph). A total of seven reappearance events have been tried for recording. Among them three were found to be outside the sub-array after the event. Hence, their light curves were not recorded. The light curves of the remaining three sources have been recorded but they are noisy. These light curves are not reported in this thesis.

The observational details of the LO events recorded with NICMOS sub-array and studied in this thesis are listed in Table.2.5 in chronological order. The Table lists 66 sources. The distribution on spectral type is - (*i*) <K-type: 3, (*ii*) K-type: 15, (*iii*) M-type: 31, (*iv*) C-type: 5 & (*vi*) S-type: 1. Among these sources most of them are giants with 10 AGB Semi-regular variables (according to SIMBAD database). The columns are arranged in the following way. Column 1: Date of the LO event, Column 2: Source designation, Column 3 & 4: Right Ascension (RA) and Declination (Dec) of the source at epoch 2000.0 respectively, Column 5: NIR K-band (2.2 μm) magnitudes of

the sources obtained from 2MASS catalog, Column 6: Spectral type of the source obtained in the SIMBAD database, Column 7: Altitude (in deg) of the source during the event, Column 8: lunar phase (in fractional days from the previous new moon), and Column 9: The sky conditions(/Remarks) during the observations of LO events.

2.6 Modeling of the occultation light curves

The Fresnel diffraction pattern is produced during the disappearance (or reappearance) of the distant star behind (or from) the sharp airless lunar limb. The observed light curve is analyzed treating the source as a combination of point sources which produce diffraction patterns along the direction of occultation. The source is assumed to be uniformly illuminated circular disk and sliced perpendicular to the direction of occultation (Fig.2.13). Each strip is treated as an equivalent point source with intensity proportional to its area. The final fringe is a convolution of the diffraction patterns produced by all these point sources separated in time. The observed fringes are smeared by different instrumental effects like finite telescope aperture, finite filter bandwidth, system response time of the detector etc. The final intensity profile of the light curve can be written as -

$$I(t) = \int_{-\infty}^{+\infty} S(\phi)d\phi \int_{-A/2}^{+A/2} O(\alpha)d\alpha \int_{\lambda 1}^{\lambda 2} \Lambda(\lambda)d\lambda \int_{-\Delta\tau}^{0} T(\tau)d\tau F(\omega) + \beta(t) \quad (2.1)$$

Where S(ϕ) is the stellar brightness profile, O(α) is the parameter due to averaging effects of the telescope, T(τ) is the electronics time response of the detector and preamplifier (not required for NICMOS sub-array in use now), $\Lambda(\lambda)$ is spectral response of the source, F(ω) is the Fresnel expression of straight edge diffraction of a monochromatic point source and β(t) is the temporal variation of the background level. The background level ($\beta(t)$) in the lunar occultation light curves is often variable due to scattered light from the moon. The variation depends on the lunar phase, atmospheric conditions, twilight etc. In disappearance events the moon approaches the detector field and hence, positive gradients are usually observed (but not always) in the light curves, while the negative gradients are generally found during reappearances.

The Fresnel function is written as -

$$F(\omega) = \frac{1}{2}\left[\left(\frac{1}{2} + C(\omega)\right)^2 + \left(\frac{1}{2} + S(\omega)\right)^2\right] \tag{2.2}$$

where C(ω) and S(ω) are Fresnel integrals and ω is Fresnel number which is written as

$$\omega = \left(\frac{2}{\lambda d}\right)^{\frac{1}{2}}\left[v(t - t_o) + d\ tan(\phi) + \alpha\right] \tag{2.3}$$

where λ is the wavelength, d is the distance to the moon, t_o is the geometric time of occultation when the intensity of the occulted source reduces to 25%, v is lunar velocity component along the direction of occultation and α is the linear displacement term due to averaging effect of the telescope aperture.

The occultation group in PRL had earlier developed a Nonlinear least squares (NLS) method based on the work of Nather & McCants (1970) and this program, suitably modified for NICMOS sampling time and filter response, has been used to analyze the light curves. In LO the one dimensional profile of the uniformly illuminated stellar disk, perpendicular to the tangent of the lunar limb is being obtained. This process involves simultaneous estimation of five free parameters - (i) geometric time of occultation, (ii) star signal counts, (iii) back-ground counts, (iv) component velocity of the moon along the direction of occultation and (v) uniform disk angular diameter of the star. All the parameters, except angular diameter are generally known for any particular event and given as initial inputs to the model fit program. Finer correction of those four values are also done by the model fit program along with the estimation of uniform disk (UD) value. A chi-square (χ^2) minimization test is involved in the model fit to have the best estimation of those parameters. Many other instrumental parameters like Filter response profile, telescope aperture function are also given as input to the model fit. The time response of the detector is not an issue for NICMOS sub-array because the instrumental time response is much smaller compared to the sampling time used to record the events.

Table 2.5: Log of observations of Lunar Occultation events at Mt. Abu Observatory.

Date of obs (dd/mm/yyyy)	Source	Coordinates (J2000.0)	m_K	Sp. type	El (°)	Lunar Phase	Sky Conditions /Remarks
19/09/2007	17335651-2857472♯	17 33 56.514 -28 57 47.22	4.92	–	35.1	7.97	Partly Cloudy
19/09/2007	HD 159089	17 33 54.309 -29 13 24.04	4.13	K5III	35.3	7.98	,,
19/09/2007	17341641-2908352♯	17 34 16.414 -29 08 35.21	4.96	M6.5III	35.6	7.98	,,
19/09/2007	17343467-2901595♯	17 34 34.676 -29 01 59.52	3.30	M8III	36.0	7.99	,,
19/09/2007	HD 159212	17 34 39.992 -29 15 21.03	4.72	K3III	36.9	8.00	,,
19/09/2007	17344692-2852318♯	17 34 46.922 -28 52 31.82	4.45	–	36.5	8.01	,,
19/09/2007	HD 315980	17 35 49.551 -28 56 35.03	4.23	K5III	35.7	8.03	,,
19/09/2007	17354808-2854448♯	17 35 48.086 -28 54 44.84	4.01	M6.5	35.6	8.03	,,
19/09/2007	17370629-2852556♯	17 37 06.293 -28 52 55.67	4.81	M7	31.7	8.07	,,
19/09/2007	17380397-2854555♯	17 38 03.977 -28 54 55.52	4.42	M6.5	28.2	8.10	,,
19/09/2007	C* 2463	17 38 31.064 -28 45 13.52	3.82	C	23.4	8.12	,,
19/09/2007	17393838-2847171♯	17 39 38.389 -28 47 17.17	3.64	M5	19.3	8.14	,,
06/11/2008	IRC -10564	21 30 37.105 -14 10 18.85	2.22	M4III:	16.7	8.78	Photometric, star drift
07/11/2008	SAO 145992	22 16 52.574 -09 02 24.45	3.22	K3III:	35.7	9.75	Photometric

Table 2.5 – continued from previous page

Date of obs (dd/mm/yyyy)	Source	Coordinates (J2000.0)	m_K	Sp. type	El (°)	Lunar Phase	Sky Conditions /Remarks
02/12/2008	RT Cap	20 17 06.516 -21 19 04.30	0.31	C	42.3	4.70	Day time, clear
03/12/2008	RS Cap†	21 07 15.428 -16 25 21.50	-0.22	M6-7III	45.8	5.82	Partly cloudy, slow wind
07/01/2009	IRAS 03333+2359	03 36 22.250 +24 09 27.75	5.07	–	55.9	10.03	Clear
09/01/2009	TU Gem	06 10 53.107 +26 00 53.32	0.82	C	18.5	12.46	Clear
05/02/2009	IRAS 05212+2655	05 24 19.176 +26 58 22.04	3.74	–	75.9	10.27	Clear, West wind
05/02/2009	SAO 77229	05 31 56.397 +26 41 05.94	3.87	K2	44.0	10.46	Clear, West wind
07/02/2009	IRC +20186	07 40 58.525 +23 01 06.75	2.18	K5III	84.4	12.39	Clear & Calm
03/03/2009	V1134 Tau	04 04 11.955 +25 23 56.61	3.84	M0	43.3	6.60	Clear, windy
04/03/2009	IRAS 05013+2704	05 04 30.698 +27 08 26.29	4.12	–	74.1	7.54	Clear, windy
04/03/2009	SAO 76965	05 07 05.162 +26 59 45.30	4.40	F5V	57.8	7.59	Clear, windy
05/03/2009	IRC +30140	06 09 20.095 +26 31 42.25	2.70	M1	88.1	8.54	Hazy, slow wind
05/03/2009	BD+26 1131	06 12 22.576 +26 20 03.86	4.06	M3IIIe...	65.1	8.61.	Hazy, calm
06/05/2009	SAO 157613	12 56 43.052 -11 56 37.14	3.24	K5	52.8	11.59	Partly cloudy
31/05/2009	IRC +00202	11 06 02.226 +01 12 38.34	2.59	M...	38.5	7.19	Clear, windy
29/11/2009	SAO 92697	01 55 31.157 +17 11 21.72	2.03	M6	70.9	12.83	Thin cloud

Table 2.5 – continued from previous page

Date of obs (dd/mm/yyyy)	Source	Coordinates (J2000.0)	m_K	Sp. type	El (°)	Lunar Phase	Sky Conditions /Remarks
29/11/2009	SAO 92755	02 01 30.386 +17 57 13.79	2.50	M...	47.0	13.02	Thin cloud
30/11/2009	UZ Ari	03 01 34.722 +21 48 12.19	1.25	M8	40.8	14.08	Partly Cloudy
29/12/2009	IRAS 04320+2519	04 35 05.617 +25 26 00.46	4.30	–	46.0	13.35	Partly Cloudy
30/12/2009	SAO 77271	05 34 51.086 +25 53 03.80	3.27	K7	75.6	14.21	Photometric
23/01/2010	SAO 92755	02 01 30.386 +17 57 13.79	2.50	M...	82.9	8.25	Photometric
23/01/2010	IRC +20037	02 03 42.621 +18 15 11.69	2.90	K4III	61.4	8.33	Photometric
24/01/2010	UZ Ari	03 01 34.722 +21 48 12.19	1.25	M8	46.4	9.41	Photometric
25/01/2010	SAO 76350	03 57 26.391 +24 27 43.05	3.20	K0	85.2	10.33	Photometric
25/01/2010	SAO 76450	04 06 04.684 +24 43 55.51	3.06	S:v...	21.2	10.54	Photometric
26/01/2010	C* 3246	04 57 20.878 +25 37 44.35	3.58	C	60.0	11.26	Photometric
27/01/2010	BI Gem	06 05 49.697 +25 14 41.56	3.17	M6	71.9	12.34	Clear, calm
28/01/2010	IRC +20177	07 20 07.367 +21 58 56.12	2.56	F0IV	51.2	13.57	Clear, calm
29/01/2010	VV Cnc	08 11 16.298 +19 08 54.59	0.94	M5	20.7	14.27	Clear, slow wind
22/02/2010	IRAS 04320+2519	04 35 05.617 +25 26 00.46	4.30	–	78.5	8.48	Partly cloudy
23/02/2010	SAO 77357	05 39 32.010 +25 18 45.07	4.39	M0	69.8	9.55	Clear, slow wind

Table 2.5 – continued from previous page

Date of obs (dd/mm/yyyy)	Source	Coordinates (J2000.0)	m_K	Sp. type	El (°)	Lunar Phase	Sky Conditions /Remarks
23/02/2010	SAO 77474	05 44 07.749 +25 22 25.59	4.14	K5	38.6	9.65	Clear, slow wind
24/02/2010	IRAS 06395+2409	06 42 35.253 +24 06 41.56	3.66	–	87.7	10.54	Clear, slow wind
23/03/2010	IRAS 06165+2431	06 19 37.503 +24 30 25.59	4.87	–	80.1	7.71	Clear, slow wind
22/04/2010	CW Cnc†	09 08 26.526 +13 13 13.64	0.11	M6	18.3	8.28	Clear, windy
23/04/2010	SAO 118044	10 00 12.812 +08 02 39.13	0.49	M2III	45.3	9.23	Clear
20/05/2010	IRC +10210	09 41 09.022 +09 53 32.11	2.50	A5V+..	64.5	6.56	Clear, moderate wind
11/12/2010	SAO 145698	21 50 35.452 -08 58 57.26	3.80	K0	52.7	5.80	Clear, calm, day light
11/01/2011	SAO 109252	00 31 37.360 +09 09 40.26	3.74	K2	57.8	7.22	Clear & slow wind
13/01/2011	UY Ari	02 05 49.064 +17 29 34.53	3.69	M5	80.4	9.22	Photometric, moderate wind
13/01/2011	AU Ari	02 08 56.711 +17 34 45.95	3.68	M0	52.0	9.31	Clear, windy
14/01/2011	SAO 75669	02 58 48.237 +20 35 39.75	3.35	M0	78.1	10.26	Clear, windy
14/01/2011	SAO 75706	03 03 03.525 +21 10 23.84	3.71	M0	34.0	10.40	Clear, windy
15/01/2011	IRC +20066	03 53 54.698 +23 07 47.36	2.60	M...	87.3	11.27	Clear, tel. oscltn in RA
15/01/2011	NSV 1406	03 54 43.086 +23 19 12.13	2.93	M4	73.9	11.31	Clear, slow wind
17/01/2011	SAO 77792	05 58 38.163 +23 39 57.94	2.97	M2	58.5	13.44	Clear, windy

Table 2.5 – continued from previous page

Date of obs (dd/mm/yyyy)	Source	Coordinates (J2000.0)	m_K	Sp. type	El (°)	Lunar Phase	Sky Conditions /Remarks
13/02/2011	IRAS 05232+2400	05 26 16.887 +24 02 58.82	3.94	–	72.2	10.58	Clear, windy
12/03/2011	SAO 76952	05 05 12.039 +23 47 56.26	4.70	K0	44.3	7.81	Photometric
13/03/2011	HD 249571	05 57 38.274 +23 33 28.98	4.50	M0III	84.7	8.69	Clear, calm, day light
13/03/2011	IRAS 05551+2305	05 58 10.549 +23 06 20.76	4.18	–	88.0	8.71	Clear, windy, day light
13/04/2011	6 Leo	09 31 57.591 +09 42 57.04	1.98	K2.5IIIb	42.9	10.16	Clear, windy
18/05/2011	CW Oph	16 55 39.099 -23 52 25.91	2.65	M7:	37.5	15.50	Clear, windy
06/11/2011	TX Psc†	23 46 23.520 +03 29 12.15	-0.51	C	68.9	10.83	Clear, hazy but calm

[1] [2]

[1]† sources were observed in Narrow CO-band (2.37μm; BW 0.1 μm). Also V* RS Cap and V* VV Cnc were observed with 2 ms and 1 ms integration respectively.

[2]♯ :2MASS designations.

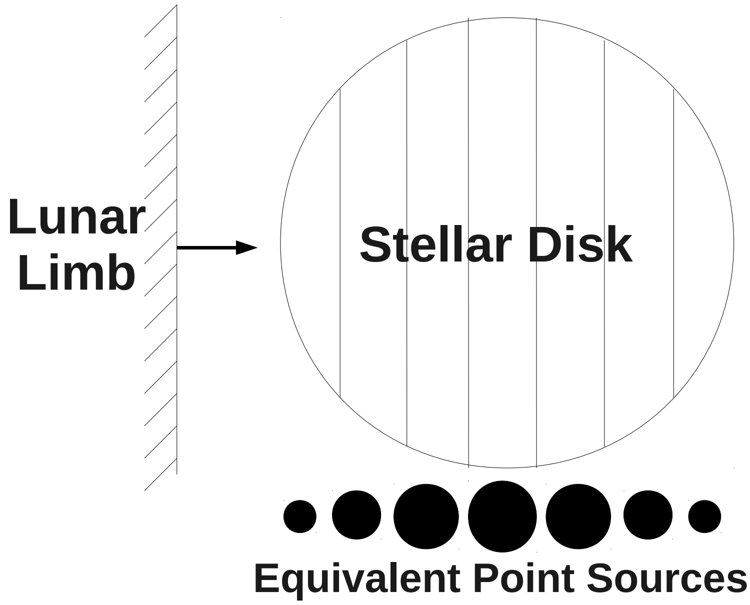

Figure 2.13: Uniformly illuminated stellar disk is sliced along the direction of occultation. Each slice represents point source with different brightness depending on its area (depicted by filled circles of different sizes).

2.6.1 Source brightness profile

The observed source is assumed to have circular disk and hence, the brightness profile of the source in the direction of occultation is modelled using a circular disk model. The brightness profile of a star can be written as (Diercks & Hunger, 1952) -

$$S(\phi) = I_o \frac{\frac{2}{\pi}\left[1 - \left(\frac{\phi}{\Omega}\right)^2\right]^{\frac{1}{2}} + \frac{\kappa}{2}\left[1 - \left(\frac{\phi}{\Omega}\right)^2\right]}{\left[1 + \frac{2}{3}\kappa\right]} \tag{2.4}$$

where ϕ is the angular resolution of the model, I_o is the intensity of the star while unocculted, Ω is angular radius of the disk, κ is the limb darkening coefficient. In Fig.2.14, the uniform disk (UD; solid line) profile for $\kappa = 0.0$ and fully darkend disk (FDD; dotted line) profile for $\kappa = 1.0$ is shown. The LO light curves are modelled assuming the disk is uniformly illuminated (UD

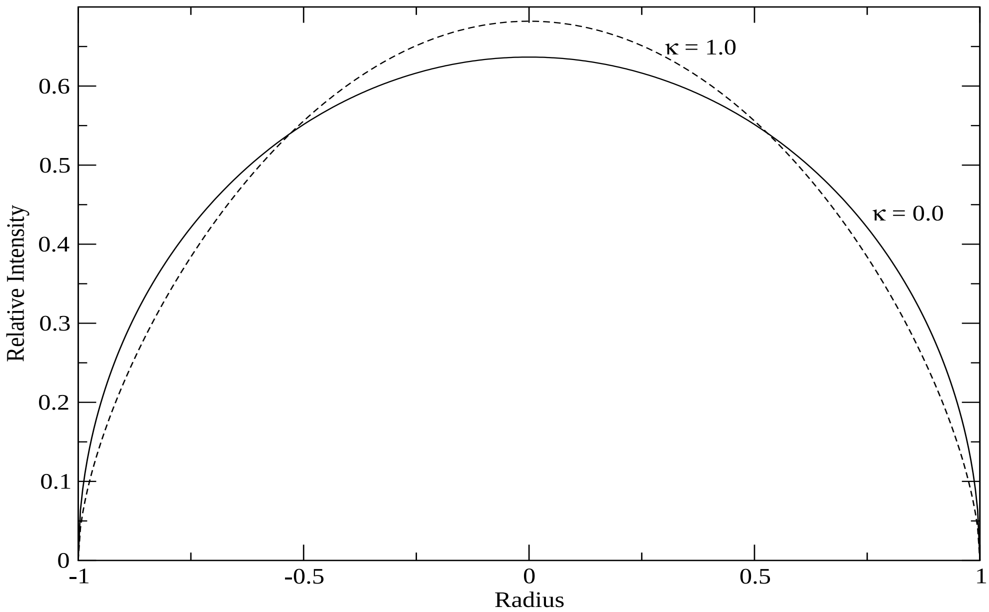

Figure 2.14: The modelled brightness profile of uniform disk (UD; solid line) and fully darkend disk (FDD; dotted line). The profile shows the relative intensity of the stellar disk as it moves from away from the centre for UD and FDD. Our modeling of all the light curves have been performed with the UD profile only.

profile). The limited signal to noise ratio of the LO light curves do not permit use of limb darkening coefficient (κ) as a free parameter in the model.

2.6.2 Filter response

The diffracted star light passes through a specific filter band during observations and it has a finite band-width. The wavelength response of the detector system depends on the (1) filter response curve $f(\lambda)$ and (2) detector response at specific wavelengths $l(\lambda)$. All these effects has to be taken into account in the model fits. So, the resultant wavelength response curve can be written as -

$$\Lambda(\lambda) = f(\lambda) \times l(\lambda)) \tag{2.5}$$

The broad K-band filter+detector response curve ($\Lambda(\lambda)$) used in the analysis is shown in Fig.2.15. However, in this thesis light curves are also observed with

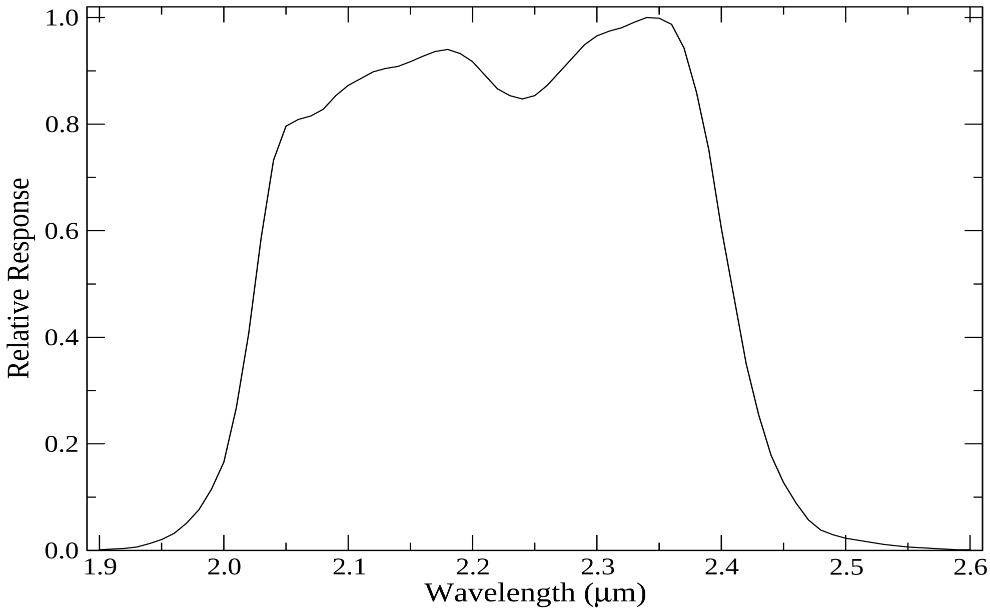

Figure 2.15: The wavelength response curve of the system in NIR K-band (2.2 μm; FWHM 0.4 μm) used in model fits.

broad K_S- and narrow CO-bands (Table.2.2). The corresponding response curves have been used in the model fits of those light curves.

2.6.3 Finite telescope aperture

The diffraction pattern of the occulted source produced at the lunar limb, sweeps across the telescope aperture. The LO fringes are averaged by the finite aperture of the telescope. The effect is proportional to diameter of the telescope aperture. It is small in moderate size 1m class telescopes but for larger apertures it needs to be taken care. For Cassegrain telescopes the secondary mirror obscuration has to be considered. The Mt. Abu telescope has a Cassegrain mount with primary mirror of 1.2m and a secondary mirror of 0.28m. If the telescope aperture sliced into small pieces of width (α) equal to the shadow displacement along the direction of occultation for any respective sampling time (Fig.2.16), then corresponding telescope aperture function can be written as -

$$O(\alpha) = \left[1 - \left(\frac{\alpha}{R_P}\right)^2\right]^{\frac{1}{2}} - \left[1 - \left(\frac{\alpha}{R_S}\right)^2\right]^{\frac{1}{2}} \text{ when } \alpha \leq R_S \tag{2.6}$$

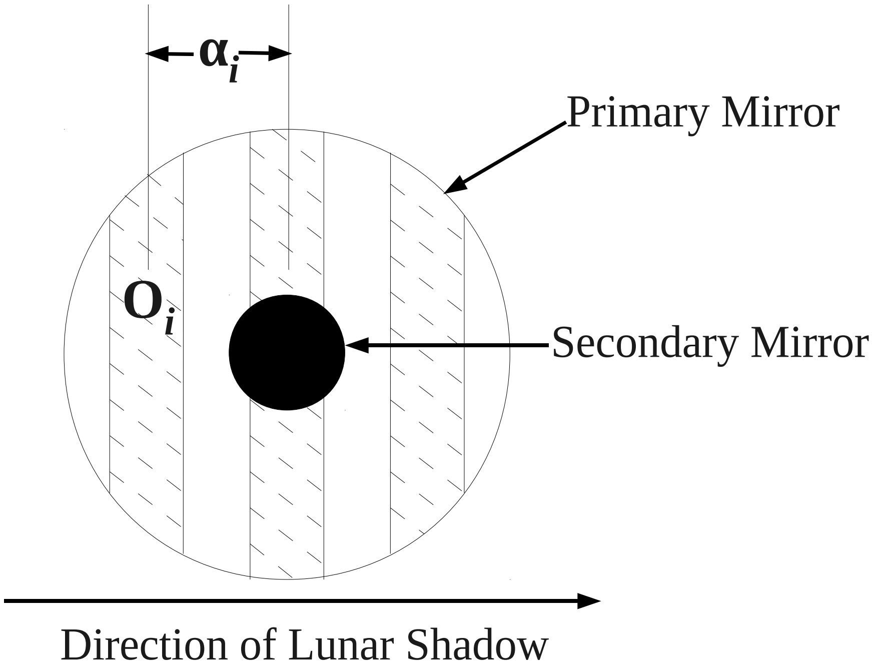

Figure 2.16: Modeling of the telescope aperture function.

$$= \left[1 - \left(\frac{\alpha}{R_P}\right)^2\right]^{\frac{1}{2}} \text{ when } R_S < \alpha \leq R_P \tag{2.7}$$

where R_P and R_S are radius of the primary and secondary mirror respectively.

We now take up in the next two chapters, the discussion on results using the LO technique pertaining to - (i) Sources in the direction of the Galactic Centre (GC) and (ii) AGB variables, including Semi-regular variables, Miras and also a few Carbon stars.

Chapter 3

Sources towards the Galactic Centre

3.1 Introduction

The restricted lunar path covers about 10% of the total sky as seen from the earth. Due to the precession of the lunar orbit the moon follows exactly the same path after a period of 18.03 years which is known as Saros Cycle. The Galactic centre is at the southern end (Dec: -29^o) of the lunar path which is not covered every lunation. Hence, the lunar occultation (LO) towards the Galactic centre is a rare but periodic phenomena. A rare passages of the moon in the vicinity of the Galactic centre during 2006-2007 provided an opportunity of studying the sources at high angular resolution using the technique of lunar occultations. The region has higher density of the stellar objects than other parts of the sky. So, the number of observable sources in a specific time increases substantially. But the Galactic centre region suffers heavy obscuration in the visible than in the NIR. Hence, lunar occultation observations in the near infrared at 2.2μm are particularly fruitful.

Lunar occultation Observations towards the Galactic centre were carried out during earlier Saros cycles. During the 1986-89 series considerable effort was made by Simon et al. (1990) to observe LO events at 2.2 μm using large telescopes in Mauna Kea. Both single element high speed photometers as well as early versions of small IR arrays were used to record the events. The sizes of several sources including IRS 16 region were estimated and photometry derived.

During the current Saros cycle, Richichi et al. (2008a) have successfully used ESO's (European Southern Observatory) 8m Very Large Telescope (VLT) in a specially devised burst mode of operation at 2.2 microns to obtain good signal to noise ratio on a large number of occulted sources towards the galactic centre. During the lunar occultation of March 21, 2006 a total of 51 events were recorded in the space of a few hours upto a magnitude limit of $m_K \leq$7.5. Of the 51 events, 30 events had good signal to noise ratio permitting resolution of two binaries and an optically thin shell around another source. In a subsequent run on August 5, 2006 using the same system Richichi et al. (2008b) recorded 78 more LO events of highly reddened sources in the central regions of the Galactic bulge over a period of 8.5 hours. The results include detection of six binaries, one triple star, two carbon stars and the central star of a planetary nebula. Later, in two more subsequent runs on September 25 & 26, 2009 Richichi et al. (2011) observed 184 sources towards the Galactic bulge. They detected 24 unknown double or multiple stars and the resolved nature of two more stars along with indications of circumstellar emission around them.

Apart from ESO, the group at Physical Research Laboratory (PRL), India also recorded the LO events towards the galactic centre region in the current Saros cycle and that is the context of this chapter.

3.2 Observations from Mt. Abu observatory

The lunar occultation observations in the vicinity of the Galactic centre region were carried out on September 19, 2007 from Mt. Abu observatory. The minimum approach to the Galactic centre during the observing run spread over four hours was about 1°.0 (Fig.3.1). Due to the rarity of the Galactic centre events, a subset of the 2MASS catalog with sources $m_K \leq$7.0 was used for predictions of LO events rather than the subset catalog with $m_K \leq$6.0

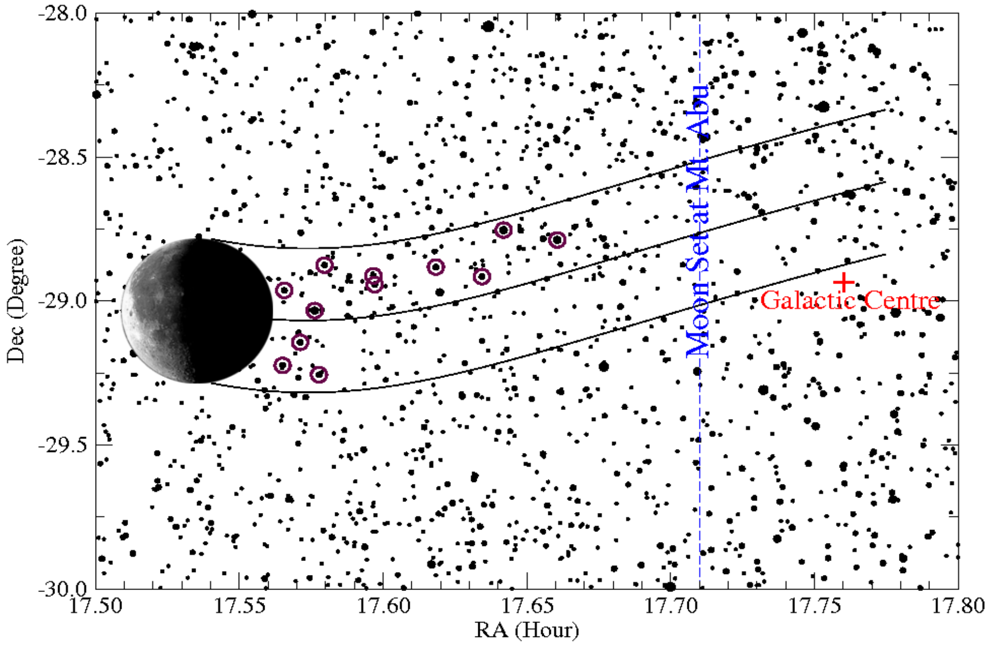

Figure 3.1: Lunar path on the sky from Mt. Abu observatory on September 19, 2007. The stars with increasing magnitudes ($m_K \leq$7.0) are plotted in circle with decreasing size. Successfully observed sources are marked with circle.

normally used. Predictions of occultation times for the observatory site show there were a total of 216 sources in the list in a span of about 4 hours. Several events were found to be happening within a few minutes of each other. After trials of the telescope for quick pointing, it was realised that the minimum switching time from one source to another was about 3 minutes. This restriction reduced the number of the observable sources to 68 with $m_K \leq 7.0$. But proper recording of the LO light curves require fast sampling otherwise it may result in unacceptable smearing of the fringes. Hence, it was not desirable to increase the integration time beyond 5 millisec (msec) which corresponds to a sampling time of 12.917 msec. Further Signal to Noise considerations also did not permit occultation observations fainter than m_K ∼5.0. The signal to noise ratio of a m_K ∼5.0 star at a typical elevation of 35 degrees (during this run) with 5 millisec integration was ∼ 15. Finally, it was found that in the few hours that the moon was available over the observatory, there were 17 possible disappearance events with $m_K \leq$5.0.

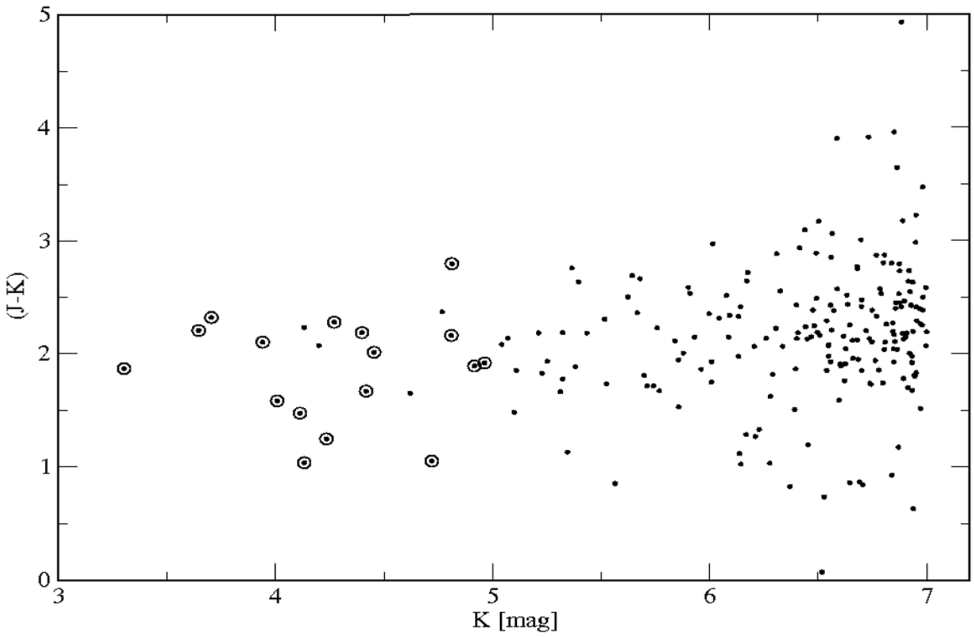

Figure 3.2: $(J-K)$ vs. K Colour-Magnitude diagram of stars upto $K = 7.0$ occulted by the Moon from Mt. Abu. Observed occultations are marked $\odot$. Almost all events brighter than $K = 5.0$ in the path have been observed.

All the lunar occultations were carried out in the NIR K_S filter band ($2.12\mu m$ /Band-width $0.35\mu m$) using the sub-array mode of the NICMOS camera. A special sequential mode of operation of the sub-array program for rapid observations was used. In this mode all the 4800 sub-frames of a run is saved in a single file. The system is then ready for next observations. This mode specifically saves time while there are numerous events to observe in smaller time intervals.

Lunar Occultation observations of the 17 predicted events were carried out in a prearranged sequence of operation. The integration time for the sources ranged from 3 millisec to 5 millisec. The corresponding data sampling time varied from 8.750 to 12.917 millisec. At the end of recording of 4800 frames the exact times of start and end of data acquisition were displayed and noted down. Details of the observations made are listed in Table.3.1.

Table 3.1: Observational details of Lunar Occultation events on 19^{th} *September, 2007*

Event No.	Source 2MASS ID	Time (UT)	Alt. (°)	m_K (2MASS)	Int. time (in msec)	Samp. time (in msec)	V_{comp} (m/ms)	PA (°)	CA (°)
Event2	17335651-2857472	12:02:19	35.1	4.92±0.02	4.000	10.833	0.580	72.88	21.63
Event3	17335430-2913240	12:12:37	35.3	4.13±0.19	4.000	10.833	0.470	135.05	41.08
Event4	17341641-2908352	12:18:05	35.6	4.96±0.02	5.000	12.917	0.592	111.35	17.80
Event5	17343467-2901595	12:28:11	36.0	3.30±0.27	3.000	10.000	0.614	85.23	7.79
Event6	17343999-2915210	12:51:17	36.9	4.72±0.02	4.000	10.833	0.407	139.32	48.78
Event7	17344692-2852318	12:53:30	36.5	4.45±0.28	4.000	10.833	0.430	44.53	45.83
Event8	17354955-2856350	13:29:42	35.7	4.23±0.04	3.000	8.750	0.575	63.75	23.69
Event9	17354808-2854448	13:32:21	35.6	4.01±0.26	3.000	8.958	0.520	53.33	34.21
Event12	17370629-2852556	14:29:59	31.7	4.81±0.02	4.000	11.042	0.584	53.66	29.64
Event13	17380397-2854555	15:03:20	28.2	4.42±0.02	3.000	8.958	0.678	66.15	15.64
Event14	17383106-2845135	15:40:52	23.4	3.82±0.10	3.000	8.958	0.478	29.18	50.98
Event17	17393838-2847171	16:09:02	19.3	3.64±0.23	4.000	10.833	0.722	53.66	25.80

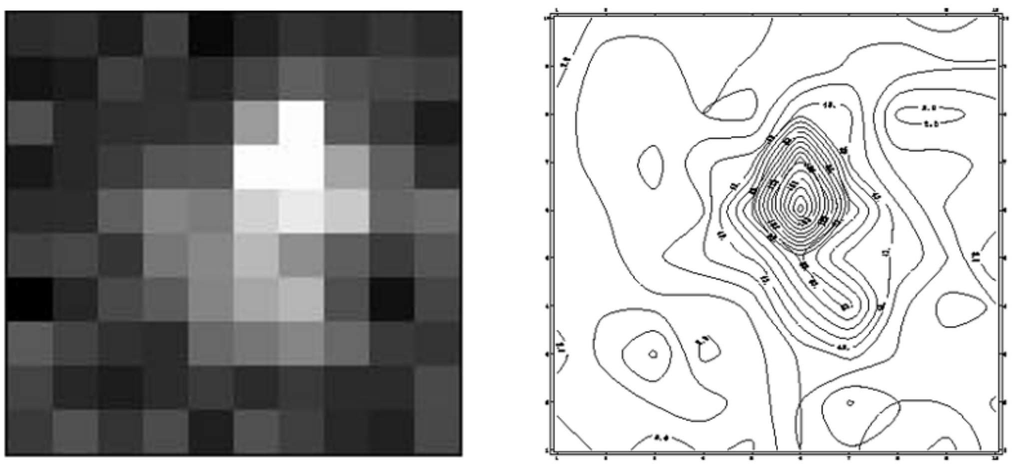

(a) (b)

Figure 3.3: Averaged sky subtracted star frame and its intensity contour map. Each sub-frame is 10×10 pixels and covers $5'' \times 5''$ *on the sky.*

3.3 Analysis

First the individual sub-frames are extracted from the single saved file for each event. The occultation light curves from the recorded sub-frames are generated in the following manner. The star is buried in a large sky background and can not be "seen" in the individual sub-frames of raw data. The sky sub-frames, acquired during each event run after the recording of the occultation, are averaged and subtracted from the data frames to generate the sky subtracted sub-frames in which the star is visible. Fig.3.3*a* shows a typical averaged sky subtracted sub-frame and Fig.3.3*b* exhibits its intensity contour map. It can be seen that the star, though not centered, is well contained within the sub-frame and occupies about 6×4 pixels ($3''\times 2''$). This star size is worse than the normal *seeing* at Gurushikar which is typically better than $2''$. The contribution of each sub-frame consists of star counts and residual sky counts within it after sky subtraction. The total counts in sky subtracted sub-frames are used to generate the light curves.

It was found that of the 17 LO events observed only 12 had recorded occultation events properly. Among the missed events, in one case the telescope was wrongly pointed and in another case the data acquisition started too late to

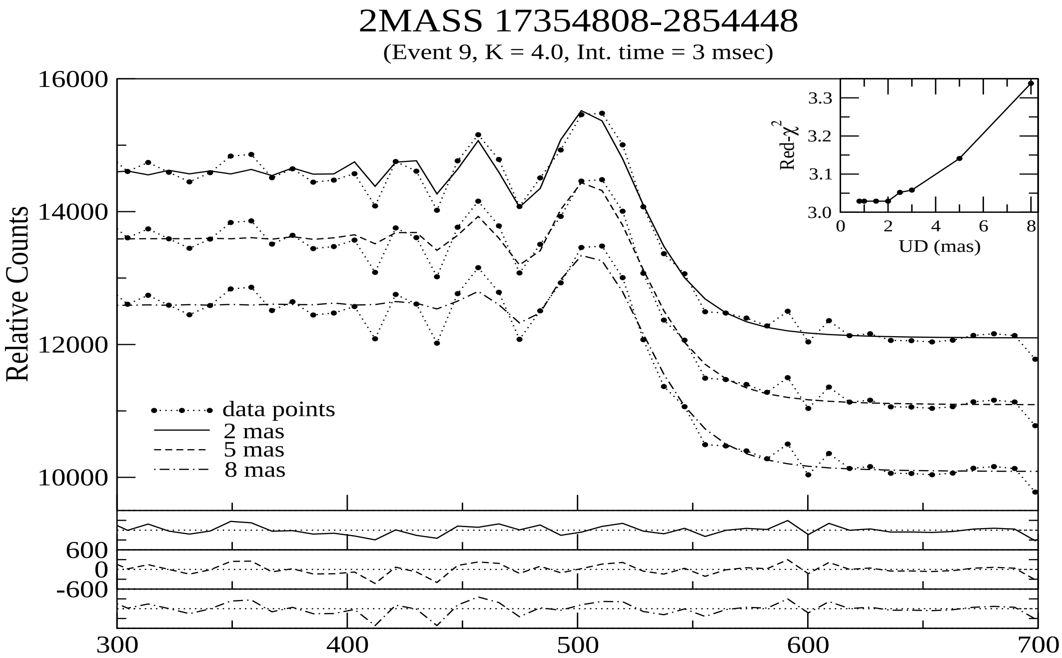

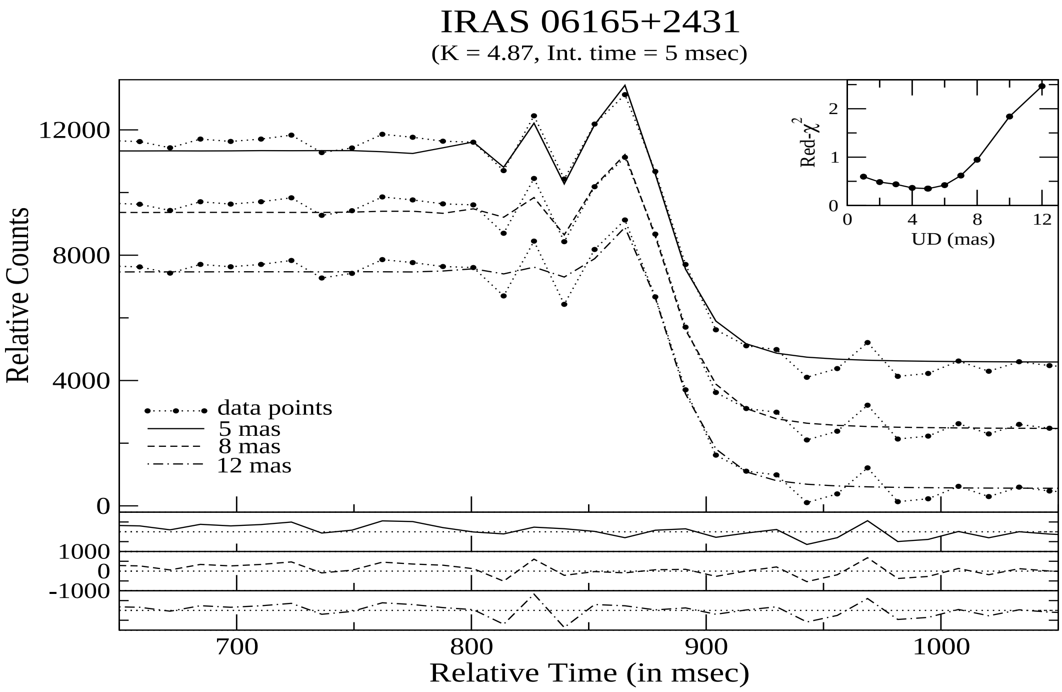

Figure 3.4: Occultation light curves and modelled fits for determining limiting angular resolution at the two integration times of 3 msec (up) and 5 msec (down) used. Number of points used in the analysis is 250 (up) and 397(down).In both cases only a portion of the light curve in the region of fringes is shown for clarity. Insets to the figures show angular diameter error curves. Modelled fits at the limiting angular resolution along with two higher angular sizes are also shown in each case. The axes are displaced to show them clearly. Residuals (Data − Model) are shown at the bottom in each case.

record the event. In the other cases the star was not positioned properly inside the sub-array and hence the registration of the occultation was incomplete.

3.3.1 Determination of the resolution limits

A serious effort has been made to determine the limiting angular resolution achievable using the present observing system for the integration and sampling times used in the observations. For this purpose the light curve of *Event* 9 and also the occultation light curve of an unresolved source IRAS 06165+2431 (m_K =4.87) observed on March 23, 2010, in a different region of the sky are used.

Event 4 has been sampled differently with an integration time of 5 millisec and the corresponding sampling time is 12.917 millisec. The event of IRAS 06165+2431 was also observed with the same integration and sampling times as for *Event* 4. Then the model fits to the light curve have been carried out. Fits with 3 different UD values along with their respective residuals are shown in Fig.3.4 (lower). The UD angular diameter error curve derived for this source is shown in inset of the figure. It can be seen that the reduced χ^2 values increases rapidly beyond 5 mas. Conservatively, the limiting angular size resolvable for the 5 msec sampling time is decided as 8.0 mas.

The source corresponding to *Event* 9 has m_K =4.0 and was observed with an integration time of 3 millisec and a sampling interval of 8.958 millisec. The model fits to the observed light curve are shown in Fig.3.4 (upper). To verify the goodness of the fit the chi-square values for different angular diameters for this source are determined and plotted (inset). It can be seen that the curve is flat till 2.5 mas and then begins to rise slowly upto 3 mas and then rapidly beyond it. The fits to the data of event 9 at various fixed UD angular sizes and the corresponding residuals (Data − Model) are also shown in the figure. The best achievable resolution is 3.0 mas for this Signal to Noise ratio and sampling time.

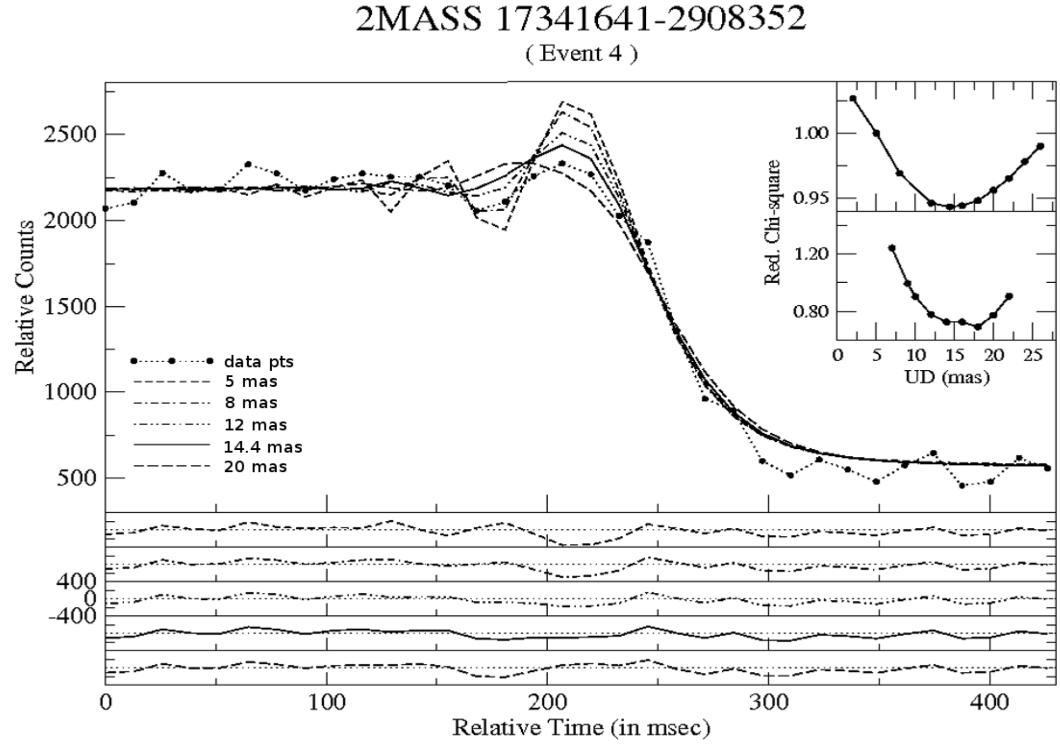

Figure 3.5: Occultation light curves and modelled fits for event 4. Upper inset shows the directly calculated error curve for angular diameter determination, while the lower inset shows error curve calculated indirectly as mentioned in the text. Modelled fits to the data at UD angular diameters of 5, 8, 12, 14.4 and 20 mas are also shown. Residuals (Data − Model) are shown for each of the modelled fits at the bottom. Number of points used in the analysis is 397. Only a portion of the full light curve in the region of fringes is shown to bring out the effect of different angular sizes. The source is clearly >8 mas which is the conservative resolution limit for the sampling time used. It is also clearly <20 mas model light curve. The best fit gives a value of 14.4±2.0 mas.

3.3.2 Extinction correction

A search in SIMBAD and other data bases like *IRAS*- and *Spitzer*- archives has been made for these sources to obtain fluxes at different wavelengths. This direction has higher extinction values than other portion of the sky. Hence, if spectral type is known an attempt has been made to derive the extinction upto the source following the procedure outlined in López-Corredoira et al. (2002) using (J−K) colour and unreddened $(J-K)_o$ values as listed in Koorneef (1983). The expression to calculate the K-band extinction upto the source is given as -

$$A_K = \frac{(J-K)-(J-K)_o}{1.52} \tag{3.1}$$

The extinction at different bands have been calculated using the ratio of relative extinction given by Nishiyama et al.(2009) applicable for the directions towards the galactic centre. They have reported the relative extinction for 2MASS bands also separately and are listed in Table.3.2.

Table 3.2: The extinction ratio for the 2MASS bands reproduced from Nishiyama et al. (2009).

Filter	Wavelength (μm)	A_λ/A_{K_S}
J_{2MASS}	1.240	2.89±0.08
H_{2MASS}	1.664	1.62±0.04
K_{S2MASS}	2.164	1.012±0.002

The unreddened values are used for the distance estimations. The absolute magnitudes of different spectral types have been adopted from Wainscoat et al. (1992). Then the distance upto the sources have been calculated using the apparent and absolute magnitudes relation. However, the method is prone to serious errors due to imperfectly determined spectral type, errors in absolute magnitude calibration. There may be errors upto 50% in the distance determinations.

3.4 Results

Of the 12 sources successfully observed three are clearly unresolved (Events 2, 3, 9). They have angular sizes less than 3.0 mas which is the limit of our resolving capability (with 3 msec integration) in the fast sub-array mode of operation used presently. Three other sources (Events 6, 7 and 17) initially appeared resolved but a careful analysis has revealed that their angular sizes are also consistent with our resolution limit of 3.0 mas within the errors of observation. The source corresponding to Event 8 has a noisy light curve but binary nature is discernible in the light curve. The ratio of intensities is $3.8\pm$ 0.2. The individual sources cannot be resolved in this event but the projected binary separation in the direction of occultation of 30 ± 5 mas is derived from the fitted light curve. There is no report of binarity in the literature for this source. Two other sources (Event 12 and Event 13) appear resolved but have large errors in the angular sizes derived. These sources are not included in the further discussion. The remaining three sources (*Event* 4, *Event* 5, *Event* 14) show UD angular sizes larger than our resolution limits for the respective sampling times.

3.4.1 Event 4:2MASS 17341641-2908352

The light curve of *Event* 4 along with the model fits are displayed for comparison in Fig.3.5. Here the fitted light curves for various angular sizes indicated are explicitly shown. In addition the residuals are shown at the bottom. It can be readily seen that the source of *Event* 4 corresponds to a UD angular size much larger than our limiting angular resolution of 8 mas for this sampling time.

In order to verify that the source has angular size larger than the resolution limits of our method, an alternative analysis using IRAS 06165+2431 as starting point source for *Event* 4 has been carried out. After normalization and velocity correction the best fit model curve for the point source is used to generate model light curves for a series of fixed angular sizes in the range of 7 to 22 mas. These model light curves are used to compare with the data of *Event* 4 and thus derive a new UD angular diameter error curve. The new error curve though not identical to the error curve shown in the upper inset of Fig.3.5 nevertheless is in good agreement giving minima in a similar range. Considering both the direct and indirect methods we conclude that *Event* 4 has angular size larger than our instrumental limits for this sampling time (UD>8 mas). Also, from inset of Fig.3.5 UD value is clearly less than 20 mas.

Among these three sources 2MASS 17341641-2908352 (*Event* 4) is particularly intriguing. Its best fit occultation light curve shows a large uniform disk angular diameter 14.4±2.2 mas. It is classified as a late M type star (M 6.5) and listed in a catalog of M-type stars (Rahasto et al. (1984)). The source has a (J−K) colour of 1.92±0.02 which is highly reddened for its spectral type. Assuming a unreddened (J−K) value of 1.34 for a M 6.5III star interpolated from Koorneef (1983), we obtain a value for extinction in K-band upto the source of 0.29±0.02 following the method discussed in Section.3.3.2. Using an interpolated absolute magnitude in K of −8.5 from Wainscoat et al. (1992), the estimated distance to the source is 4.3±1.0 Kpc. Using this distance as representative, it is found that the measured angular size corresponds to linear extent 62±15 AU which is much larger than the size of the star. From interferometric measurements of van Belle & Thompson (1999), for a M6.5III star the radius would be 156 $R_\odot$, which implies that what is seen in our observations in K band is an extended emission around the star with a radius of 43±10 $R_\star$.

The spectral data are examined, mainly in optical and Infrared available in the literature (DENIS, 2MASS, MSX6C, GLIMPSE II etc.) for the source of *Event* 4. In Fig.3.7 the Spectral Energy Distributions (SED) of the source for *IR* wavelengths are plotted, along with the SEDs of *Event* 5 and *Event* 14. *MSX6C* satellite survey of the Galactic plane shows a large flux 17.37±4.22 Jy at 4.3 μm for *Event* 4. The data suggests substantial excess at 4.3 μm of about 1.5 magnitudes but there is no excess at longer wavelength. No *IRAS* data is available for this source.

3.4.2 Event 5: 2MASS 17343467-2901595

The source corresponding to *Event* 5 (2MASS 17343467-2901595) is listed as a variable source in Terzan et al. (1991). The source has a classification of M8 in the Tokyo Catalog (Rahasto et.al 1984). By the method discussed in Section.3.3.2, the K-band extinction value to the source is derived $A_k = 0.21 \pm 0.13$. Also with a similar argument as for *Event* 4, the estimated distance to the source is 4.2 $\pm$1.0 Kpc. The measured UD angular diameter of 9.5$\pm$1.0 mas translates to a linear size of 40$\pm$4.0 AU. As a M8 III star has a radius of 215 R (van Belle et.al 1999a), so the source has an extended emission with a radius of 20$\pm$2.0 $R_\star$. The source corresponding to *Event* 5 also exhibits an IR excess, but at longer wavelengths around 10 μm (Fig.3.7).

3.4.3 Event 14: 2MASS 17383106-2845135

The source of event 14 (2MASS 17383106-2845135) is listed as a carbon star (C* 2463) in the Tokyo catalog (Rahasto et al., 1984). From its IRAS fluxes at 12 and 25 microns the derived ([12]$-$[25]) colour is 0.62 which according Wainscoat et al. (1992) would correspond to a AGB CO7 type star with a (J$-$K) intrinsic colour of +1.33 and a absolute K magnitude of -7.64. Following procedure similar to that for earlier cases the obtained value of A_k is 0.28$\pm$0.05 and a distance to the source of 1.6 $\pm$0.1 Kpc. The measured uniform disk angular size of 8.5$\pm$2.0 mas translates at this distance to a linear diameter of 13.8$\pm$0.6 AU. According to van Belle et al. (1999b) Carbon stars have a linear diameter of 350 $\pm$70 $R_\odot$, which would imply that we are resolving a shell around this star with a radius of 4.2$\pm$1.2 $R_\star$. Such close shells have been detected earlier around the carbon star TX Psc (Richichi et al. 1995) by Lunar Occultations and also by adaptive optics methods (Cruzalebes et al. 1998). This source also exhibits an IR excess at longer wavelengths around 10μm (Fig.3.7) like *Event* 5.

In all the three resolved cases the uniform disk angular sizes derived from our observations are not consistent with the stellar disks at the estimated

.

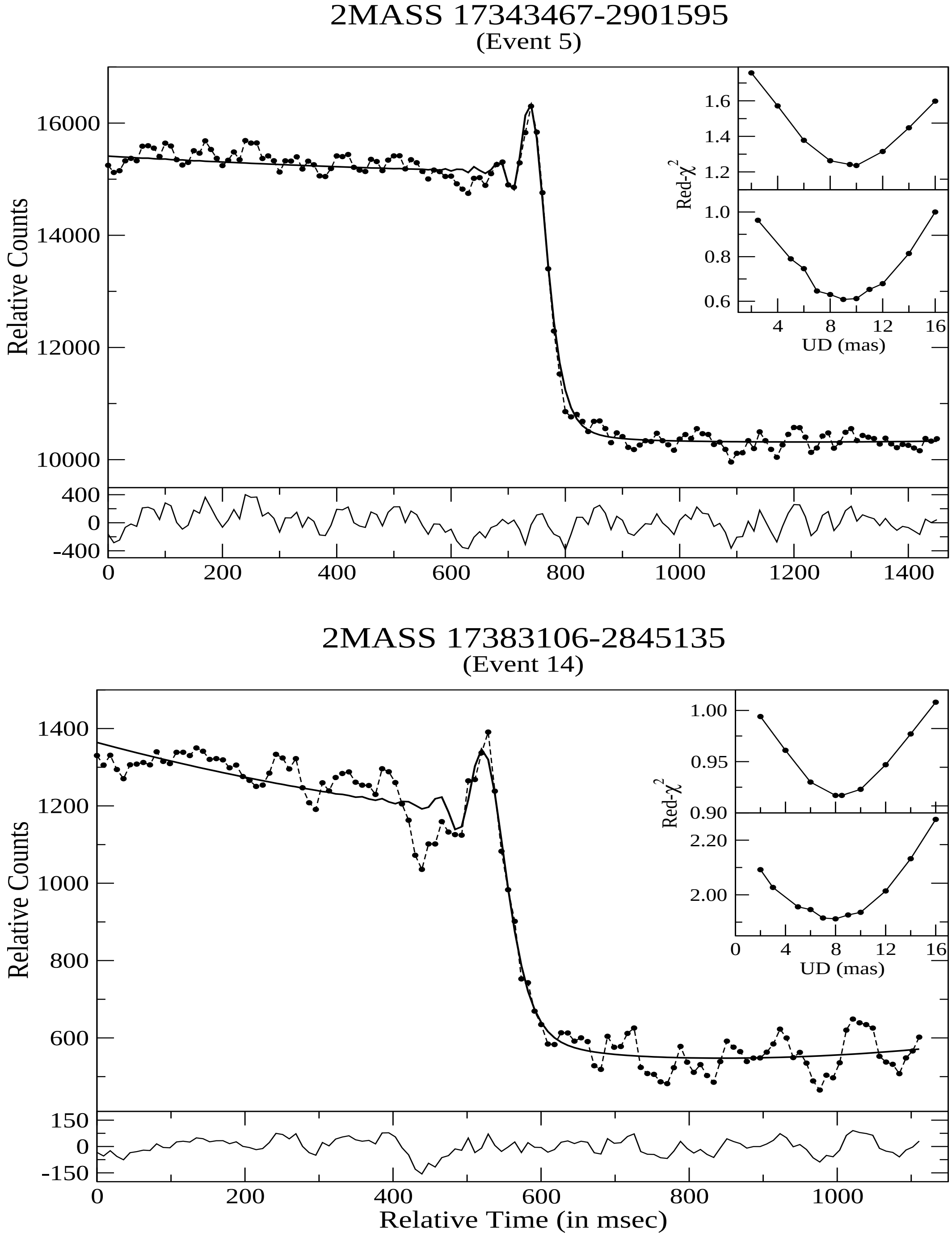

Figure 3.6: Occultation light curves and modelled fits for Event 5 (up) and Event 14 (down). Upper insets of both the figures show the directly calculated error curve for angular diameter determination, while the lower insets show error curve calculated indirectly as mentioned in the text. Residuals (Data − Model) are shown at the bottom.

Table 3.3: Results of Resolved Sources

	Spectral Type	(J-K)	A_K	S/N	Distance Estimate (kpc)	UD range (mas)	Best-fit UD (mas)
Event4	M6.5III	1.92±0.02	0.28±0.02	15	4.3±1.0	$8< UD <20$	14.4±2.2
Event5	M8III	1.87±0.27	0.21±0.13	31	4.2±1.0	$3< UD <15$	9.5±1.0
Event14	C	1.89±0.10	0.28±0.05	20	1.6±0.1	$3< UD <15$	8.5±2.0
					Brightness Ratio	Binary Separation (mas)	
Event8	K5III	1.25±0.04	0.16±0.02	7	3.8±0.2	30±5	

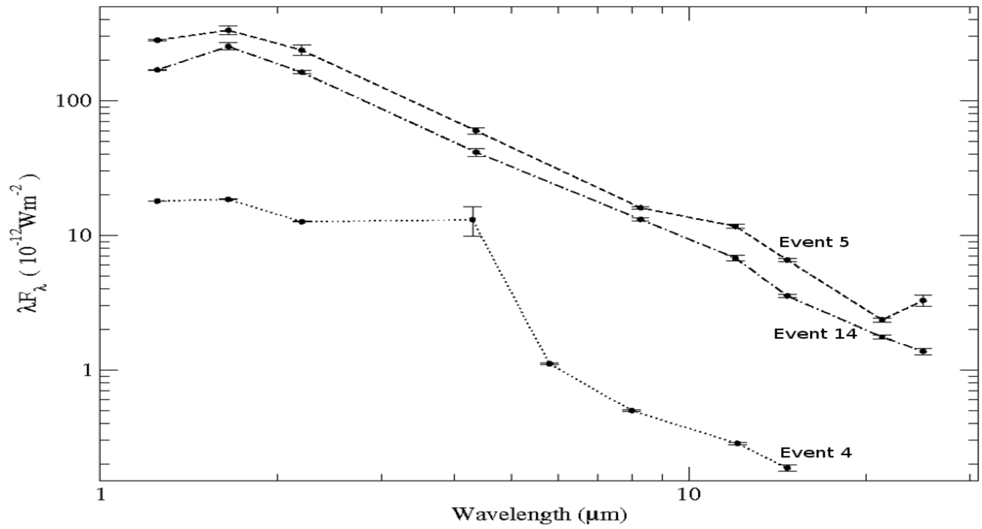

Figure 3.7: Spectral Energy distribution (SED) in the near IR and mid IR regions for the three resolved sources. Y-axis is in units of $10^{-12}Wm^{-2}$. *For event 5 and event 14 the fluxes are multiplied by 5 to displace their SEDs upwards for clarity. It can be seen that event 4 exhibits strong IR excess at 4.3μm (MSX6C measurement) while event 5 and 14 show IR excess in the 10 μm region.*

distance to these sources and suggest the presence of circumstellar material around these objects. However it must be pointed out that our Signal to Noise in any of these sources is not adequate to resolve the star and the circumstellar shell separately. The concept of UD angular diameter used may not be a good approximation for stars with substantial circumstellar emission. Further the distances to the sources have been inferred indirectly and could have large absolute errors which in turn would affect the linear sizes derived. Nevertheless the three sources are clearly resolved beyond observational errors and need to be explored further. The results are summarised in Table.3.3.

3.5 Conclusions

Lunar Occultation observations of 12 sources in the galactic centre region carried out in the near infrared K_S band show that while majority of the sources are unresolved (angular sizes < 3.0 mas), three sources appear clearly resolved with uniform disk angular diameters ranging from 8 mas to 14 mas. In addition there is a signature of binarity in one of the unresolved sources. Two of the resolved sources are late M-giants while one is a carbon star. The resolved structures are interpreted as circumstellar emission from these sources and using available extinction and spectral data estimate their linear extent are calculated in units of respective stellar radii, subject to errors involved in distance determination.

Chapter 4

Mira and Semi-regular variables

4.1 Introduction

Asymptotic giant branch (AGB) stars are highly evolved cool stars in the last stages of their stellar evolution before turning into planetary nebulae. The high mass loss rates ($10^{-7} - 10^{-6}\ M_{\odot}yr^{-1}$) and relatively low surface temperatures of these stars provide a habitable zone for several molecules like TiO, VO, H_2O and CO in their extended atmospheres. The molecule-rich atmosphere of AGB stars are main source to enrich the interstellar medium by mass-loss mechanism. A very common characteristic of AGB stars is the long period variability of their radiative output, mainly, due to pulsation of their atmospheres, though episodic ejection of dust can also contribute to the variability (Lattanzio & Wood, 2003). Traditionally AGB stars have been classified according to their visual variability amplitude in magnitude as (1) classical Mira variables (visual amplitude > 2.5), clearly defined periodicity in the range 100-1000 days, (2) Semi-regular variables (SRV): SRa - visual amplitude < 2.5 and periods in the range 35-1200 days; SRb - visual amplitude < 2.5 with poorly defined periods, (3) Irregular variables with small amplitude and no definite periods. In addition there is also a class of Super-giant semi-regular variables (SRc). Micro-lensing surveys such as $MACHO$ (Alcock et al., 1995), $EROS$ (Aubourg et al., 1993) and $OGLE$ (Udalski et al., 1993) during the last 15 years have produced many high quality light curves of the

AGB stars upto V-mag $\sim$ 20 which have discerned distinct periodicities in objects hitherto classified as irregular variables.

A recent important class of AGB variables too faint to be found in GCVS (General Catalog of Variable Stars; Samus et. al., 2009) consist of dust enshrouded infrared variables, found in Infrared surveys, which pulsate with larger amplitude in K-band (2.2 μm) (K-amp $\sim$ 3) and longer period ($\geq$ 600 days) than optical Mira Variables (Whitelock et al., 1994; Wood, Habing & McGregor, 1998). The dust enshrouded IR variables are considered to be in a more advanced state of evolution than classical Miras.

High angular measurements of angular sizes of Mira variables at different phases of their pulsation cycle provide an important direct means of understanding their atmospheric extension and pulsation properties. However, large opacities due to absorption by molecular species in their atmospheres mask the dominant continuum radiation from the photosphere. Consequently, photospheric angular size measurements are affected differently in different filter bands which has been known for sometime (Haniff, Scholz & Tuthill, 1995). In recent years there have been many high quality measurements of Mira variables at IR wavelengths but measurements of SRVs are relatively few. Mennesson et al. (2002) found L'-band (3.8μm) diameters of several oxygen rich Miras were much larger (25% to 100%) than those measured in the broad K-band and ascribed it to a wavelength dependent transparency of an optically thin gaseous shell around the star. In a multi-epoch interferometric study of two Mira variables spread over several pulsation cycles, Thompson, Creech-Eakman & van Belle (2002) report variations in narrow band angular sizes within the K-band (2.0 - 2.4 μm) and attribute them to molecular absorptions. Perrin et al. (2004) observed several Miras in the narrow bands around 2.2 μm and found systemically larger diameters in bands contaminated by water vapour or CO. Millan-Gabet et al. (2005) report from simultaneous measurements in J, H and K'-bands of 23 Miras, a systematic increase of angular size with wavelength (25%) from J to H to K'. Mondal & Chandrasekhar (2005) find a 20% increase in their K-band Lunar Occultation (LO) measurement of one

Table 4.1: Observational details of Lunar Occultation events.

Source	JD Obs. 2450000+	Phot. Phase†	Lunar Phase (days)	Alt. (°)	Detector used	Samp (msec)	S/N	$V^{\ddagger}_{comp}$ (m/ms)	PA§ (°)	CA♮ (°)
AW Aur	3802.082	0.95	7.6	85.5	InSb	1.00	14	0.616	71.3	16.4
BS Aur	3775.306	0.83	10.2	45.1	InSb	1.00	20	0.807	87.0	13.9
GP Tau	2710.251	0.43	8.6	29.5	InSb	2.00	19	0.486	148.1	55.2
RS Cap	4804.023	0.43	5.8	36.0	MCT	7.29	39	0.339	-5.7	58.2
RT Cap	4802.908	0.72	4.7	36.9	MCT	8.75	48	0.516	91.0	27.5

† Photometric phase is derived for the epoch of our observation from GCVS or ASAS catalogs. It varies from 0 to 1 with 0.5 signifying minimum light.

‡ V_{comp} refers to the predicted velocity component of the moon in the direction of occultation.

§ PA is the position angle of the point of occultation on the lunar limb measured from North to East.

♮ CA is the contact angle between the direction of lunar velocity and the direction of occultation.

Table 4.2: Observed Source details

Source		Spectral	Variability	m_K	m_V		$(K-[12])$	Period	Ref.
IRC No.	Name	Type	Type		max	min	colour excess	(days)	cat.
+30123	AW Aur	M5-M9	Mira	2.34±0.07	10.10	17.10	1.1	445±10	GCVS
+30136	BS Aur	M8-M9	Mira	2.15±0.06	10.20	>15.00	2.6	467±05	GCVS
+20116	GP Tau	M7	SRb	0.29±0.07	9.57	10.40	0.9	109±10	ASAS
−20596	RS Cap	M6/M7	SRb	-0.39±0.04	7.90	8.36	1.2	193±15	ASAS
−20585	RT Cap	C	SRb	0.55±0.06	7.66	8.61	0.2	389±10	ASAS

Mira (U Ari) compared to a reported H-band measurement at the same phase. These authors have also reported that two SR variables do not show any phase variation in their K- and L'-band angular diameters.

In a detailed three telescopes interferometric study in the H-band Ragland et al. (2006) find that almost all Miras show an asymmetry in their brightness distribution and attribute it to the formation of an inhomogeneous translucent molecular screen located at about 1.5 to 2.5 stellar radii. A multi-spectral lunar occultation of the dust-enshrouded carbon star AFGL 5440 with high-speed spectro-photometer in the wavelength range 1-4 μm has been observed by Harvey & Oldag (2007). They separately resolved the photosphere and inner edge of the circumstellar dust shell, and also strongly constrained the inner radius of the dust shell surrounding the star as well as the near-infrared optical depth. Earlier, Eisner et al. (2007) using higher spectral resolution interferometric observations of a Mira (R Vir) also find the measured radius of emission varies substantially from 2.0 to 2.4 μm. They infer that most of the molecular opacity arises predominantly due to H_2O at about twice the stellar photospheric radius. Propagating shocks associated with Mira pulsation provide a mechanism for lifting the molecular layer to the observed location. Woodruff et al. (2009) in a spectro-interferometric study of 3 Miras from 1.1 to 3.8 μm report strong size variations with wavelength probing zones of H_2O, CO, OH and dust. The variation in UD angular diameters by a factor of two from 1.0 to 3.0 μm consolidates the picture of a Mira atmosphere consisting of molecular shells and time dependent densities and temperatures. In a recent NIR K-band spectro-interferometric study of a carbon-rich Mira variable (R Cnc) using $VLTI$, Wittkowski et al. (2011) have found that the angular diameters are about 70% enhanced in the wavelength region of >2.29 μm than the angular diameter at the continuum (2.25 μm).

4.2 Observations and Data Analysis

The LO observations of all but one of these sources were carried out in the near-Infrared broad-K-band (2.2 μm/0.4 μm). The bright source RS Cap was observed in narrow CO-band filter (2.37μm/0.1 μm) to avoid saturation effects. The details of the observations are listed in Table.4.1. All are disappearance events at lunar phase measured in days after new moon as listed in Table.4.1. Among the five sources, three (AW Aur, BS Aur and GP Tau) were observed with the single element fast InSb detector with an effective field of view about 10 arcsec on the sky. The remaining two sources were recorded using the 10×10 pixel ($5'' \times 5''$) sub-array mode of the NICMOS IR-camera. The light curve is carefully analysed to extract the uniform disk (UD) angular diameter of the stellar source using the method of non-linear least squares (NLS) discussed in Section.2.6.

4.3 Source details

The individual source details are listed in Table.4.2. and discussed below. UD angular diameters derived from our observations are given for each of the sources and also listed in Table.4.3.

4.3.1 AW Aur

AW Aur is an oxygen-rich Mira variable with spectral type ranging from M5 to M9. According to GCVS the reported period is 443.2 days with the epoch of maximum light at JD 2453823.0. The V-band magnitude variation is from 10.10 to 17.10 and Spectral type variation from M5 to M9. Using Lomb-Scargle normalized periodogram formula (Scargle, 1982) we verified that the maximum power in the light curve is at the period of 445($\pm$10) days in good agreement with the reported GCVS value. We adopt this value of periodic variability for AW Aur.

No Hipparcos parallax measurement is available for this source. However, we can make an estimation of the distance to the source using the Period-Luminosity (PL) relation for Galactic Miras as given by Whitelock, Feast & van Leeuween (2008). We obtain an absolute K-magnitude value -8.18 ± 0.28 and the distance to the source 1.02 ± 0.11 kpc (without extinction correction). This value is in agreement with the value of 1063 pc reported by Le Bertre et al. (2003) who also reported a mass loss rate of 3×10^{-7} $M_{\odot}$ yr^{-1} for this star. We adopt a value of 1 kpc as distance to the source.

The occultation of AW Aur was recorded close to the maximum (phase 0.95) using the InSb photometer. Following the NLS procedure outlined earlier the observed light curve is fitted with the Uniform Disk (UD) model, which is shown in Fig.4.1 along with the residuals (data-model) in the lower panel. Inset in the figure shows the error curve for different UD sizes. The minima of this curve indicates our best estimate for the UD angular diameter. For AW Aur we derive UD angular size of 4.33 ± 0.50 milliarcsec. There is no previous measurement of angular size of this source.

4.3.2 BS Aur

BS Aur is a late M-type (M8-M9) oxygen-rich Mira variable with a pulsation period of 466.7 days as reported by GCVS. The V-band magnitude varies from 10.20 to $>$ 15.00 with the epoch of maximum light at 2441255.0 JD. Following a similar procedure as in the case of AW Aur we find the maximum power refers to the period 480($\pm$5) days which is close to the value reported in the catalog. Using the Period-Luminosity relation as in the case of AW Aur we calculate the absolute K-magnitude of the source as -8.27 ± 0.20 and estimate a distance of 1.2 kpc (without extinction correction). The LO light curve observed in NIR K-band from Mt. Abu using single channel photometer under good sky conditions is shown in Fig.4.1. The derived UD angular diameter of the source is 5.00 ± 0.70 mas at the photometric phase of 0.83.

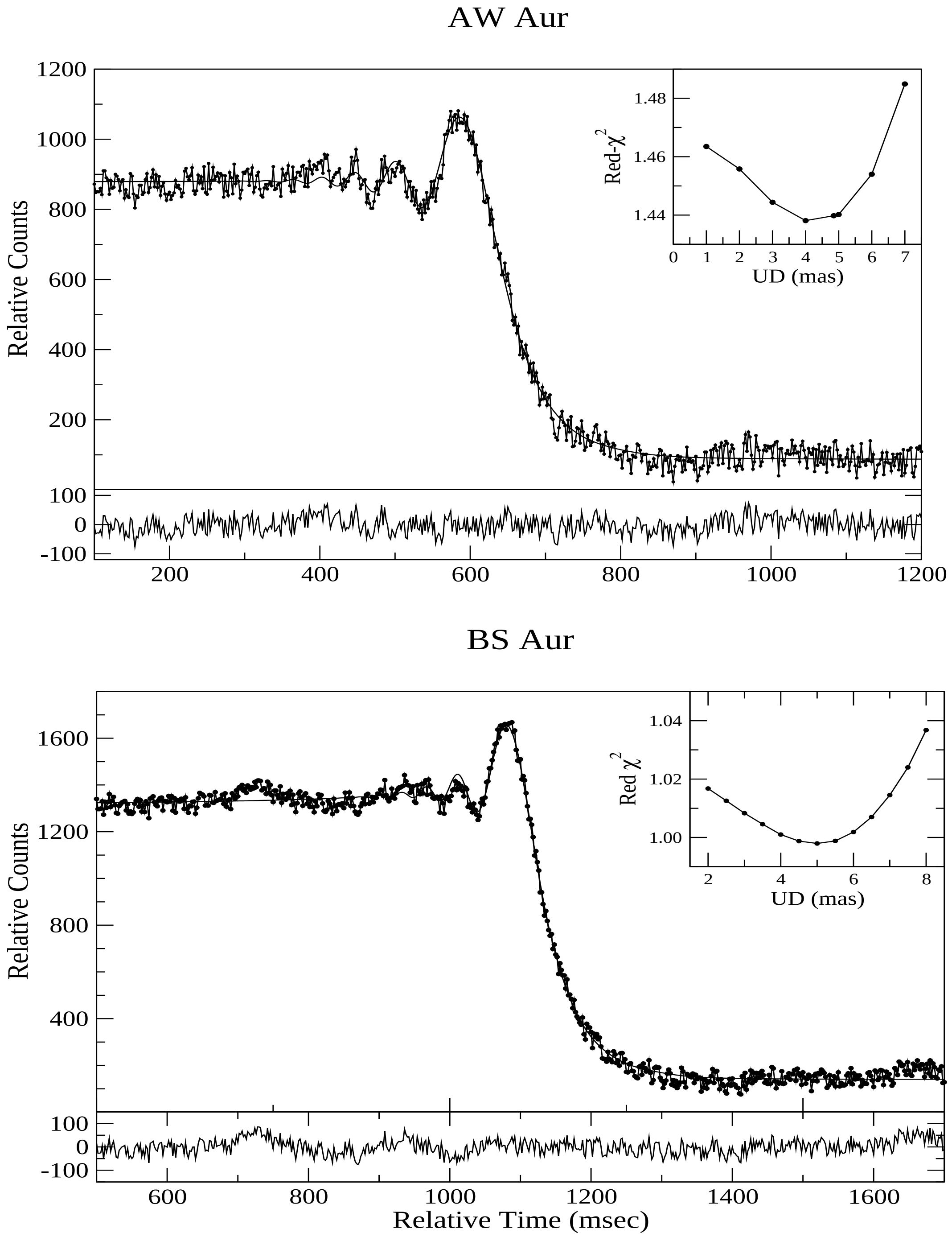

Figure 4.1: Observed and model fitted light curves of two Mira variables, AW Aur and BS Aur. The inset shows the error curve of the UD angular diameter determination and the lower panel shows the residuals (data − model) of the best fit. Both Miras have been observed in broad K-band.

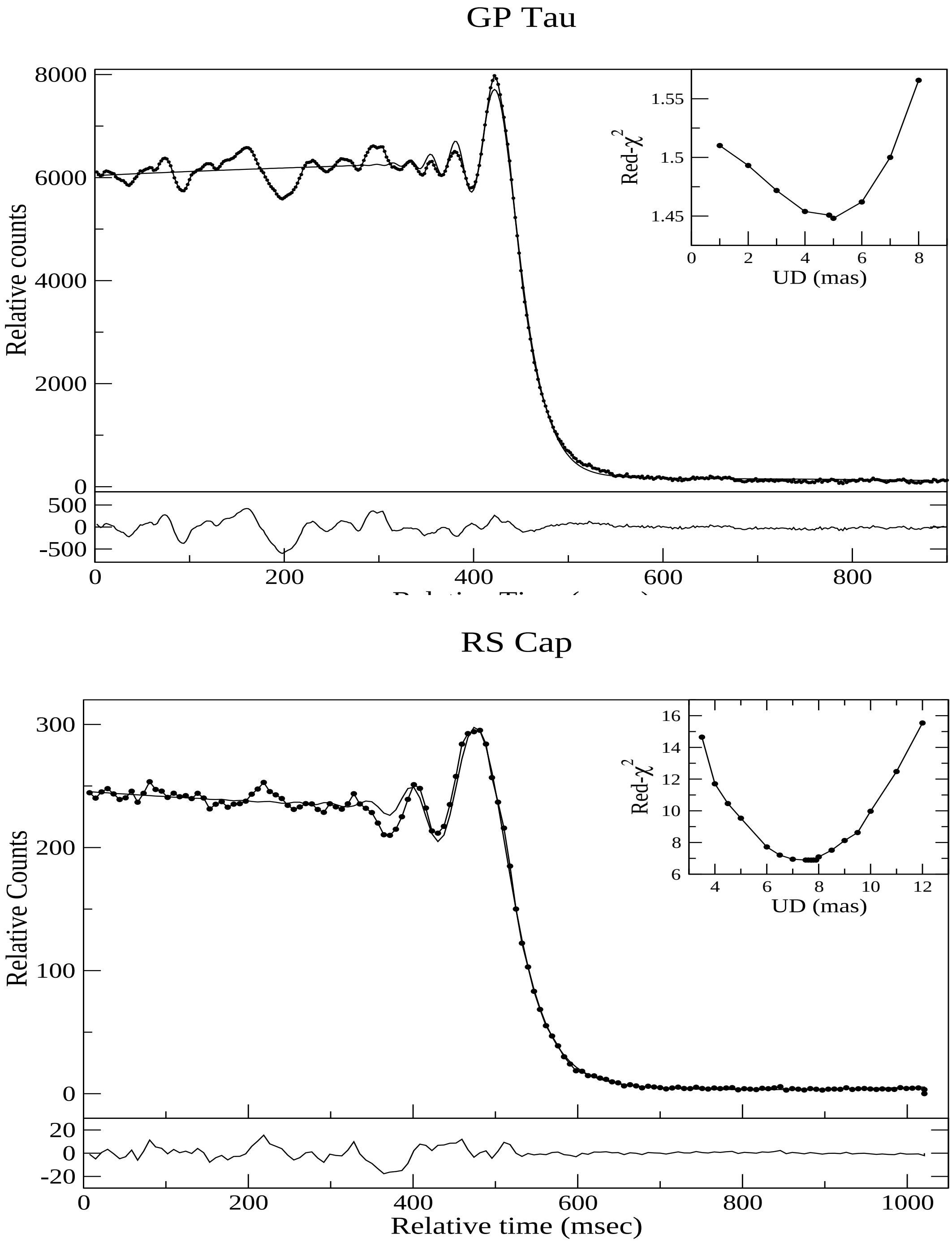

Figure 4.2: Observed and model fitted light curves of GP Tau and RS Cap. The inset shows the error curve of the UD angular diameter determination and the lower panel shows the residuals (data − model) of the best fit.

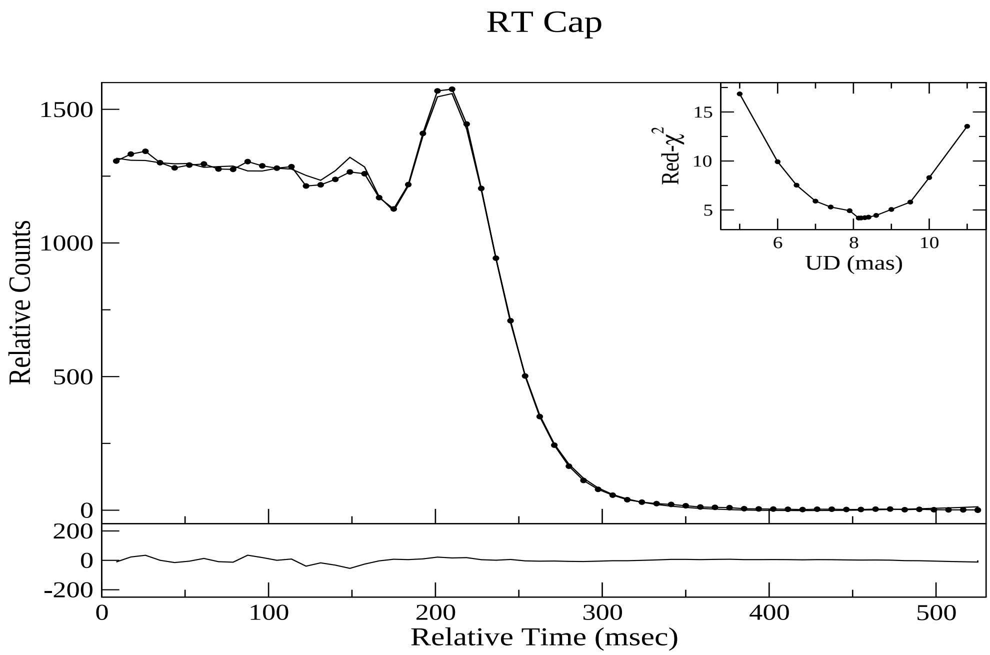

Figure 4.3: Observed and model fitted light curves of RT Cap. The inset shows the error curve of the UD angular diameter determination and the lower panel shows the residuals (data − model) of the best fit.

4.3.3 GP Tau

GP Tau is a M7-type giant. According to ASAS catalog it is a semi-regular (SRb) variable with a period of 109 days and a visual magnitude amplitude of 0.83 (Pojmanski et al., 2005). It is known from IRAS measurements (Helou & Walker, 1986) that GP Tau has a thin circumstellar shell (Sloan & Price (1998). H_2O maser has also been reported on the source (Han et.al 1998; Kim J et.al 2010) at a distance of 10-20 stellar radius from the centre.

The only parallax measurement of GP Tau reported has very large error 10.80±38.30 mas (Hipparcos & Tycho Cat.). No previous angular size measurement is available on this source. Our observed lunar occultation light curve along with its best fit is shown in Fig.4.2. We obtain the UD angular diameter of 4.85±0.50 mas. We estimate the distance to the source to be ∼270 pc, using the absolute K-magnitude of -9.04 for M7 giants as reported by Wainscoat et al. (1992).

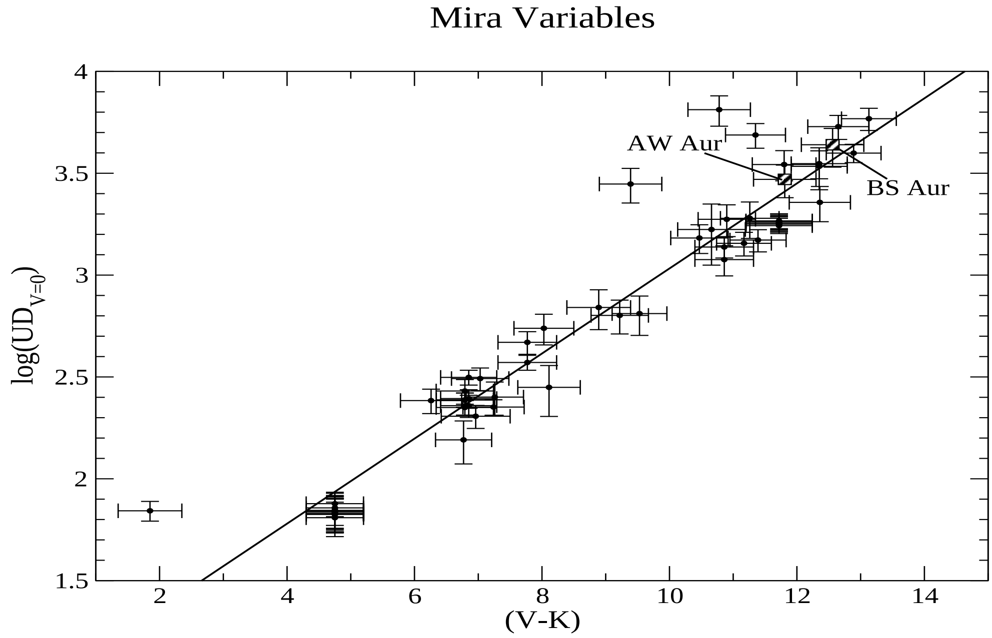

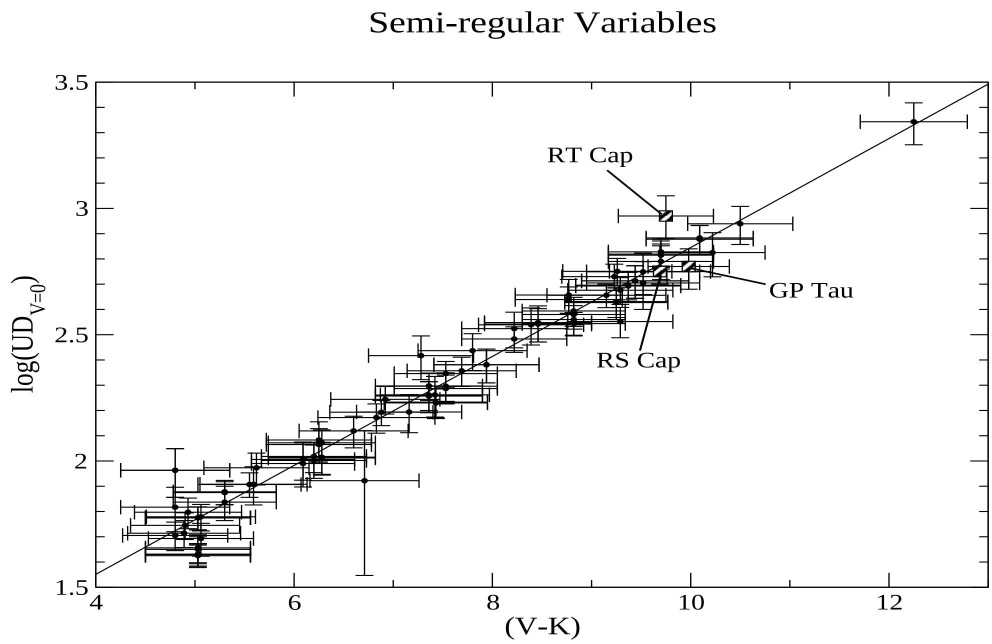

(b)

Figure 4.4: The (V−K) colour vs. zero-magnitude angular diameter of o-rich Mira variables (54 measurements) and SRVs (83 measurements). The solid line represents the least squares fit to these points. [correlation coefficients are 0.94 (Miras) and 0.98 (SRVs)]. Position of sources in our sample is also indicated.

4.3.4 RS Cap

RS Cap is a late M-type source with a spectral type M6-M7III. It is a semi-regular (SRb) variable. According to the catalog of variable stars in the southern hemisphere (Pojmanski et al., 2005) the period of the source is 193 days with a V-amplitude 0.46 mag. Kahane & Jura (1994) using millimeter-wave observations estimated distance to RS Cap of 280 parsecs. Winters et.al (2003) from CO observations report a distance of 277 parsecs and a mass loss rate of $\dot{M} = 1.08 \times 10^{-6} M_{\odot}$ /yr. Earlier angular diameter measurements of RS Cap are also available. Richichi et .al (1992) obtained from LO methods the UD angular diameter value of 7.75±0.67 mas and derived the effective temperature of the source to be $T_e = 3560$ K. No circumstellar shell was detected, though the spectral energy distribution indicates the presence of a weak shell around the source with less than 1% strength of the stellar signal. Later Dyck, van Belle & Thompson (1998) reported from interferometric observations at 2.2 μm an angular diameter of 7.0±0.8 mas.

We obtain the best fit UD angular diameter of 7.70±0.50 mas which is consistent with earlier measurements. We adopt a distance to the source of 280 pc.

4.3.5 RT Cap

According to Bergeat & Chevallier (2005) RT Cap is a carbon-rich, non-Mira giant with photospheric carbon to oxygen ratio (C/O) 1.10. The periods derived from V-band light curves are 393 days (GCVS) and 389 days (Pojmanski et. al. 2005). The distance to the source is estimated to be 560 pc using apparent and absolute bolometric magnitudes 3.80 and −4.95 respectively (Bergeat, Knapik & Rutily, 2002). They also derived an effective temperature $T_e = 2480$ K and a mass-loss rate of $2.3 \times 10^{-7} M_{\odot} yr^{-1}$.

There are two high angular diameter measurements reported for this source earlier. One earlier measurement by Schmidtke et al. (1986) using the Lunar Occultation technique in narrow K-band (2.173 μm/BW 0.032 μm) yielded a uniform disk value of 7.72±0.16 mas at a photometric phase of 0.98. Another UD value reported using long-baseline interferometry in broad K-band (van Belle et al., 2000) is 8.18±0.21 mas.

From our observed light curve (Fig.4.3) we derive a UD value of 8.14±0.50 mas at a photometric phase of 0.72.

4.4 Results and Discussion

Uniform disk (UD) Angular diameters of the five sources derived from our observations and analysis are listed in second column of Table.4.3. A prediction method to estimate the uniform disk angular diameter of the AGB variables has been derived. The effect of the mass-loss/circumstellar shell on the UD diameter values has been investigated.

4.4.1 UD Angular Diameter predictions using $(V - K)$ colour

We have first made an attempt to compare our results with the predictions of angular sizes generated by us following the approximate methods devised by Di Benedetto (1993) and van Belle (1999). The methods use the observed K and V broad band photometry to predict a zero magnitude ($m_V = 0$) angular size using $(V - K)$ colours through a calibration. The zero magnitude angular sizes are then scaled to the apparent angular sizes using V-band photometry. We have generated a new calibration using the 54 measured K-band angular diameter determinations of oxygen-rich Miras available in the literature (Richichi et al., 2005), scaled to the zero-magnitude angular diameters, and plotted against their respective $(V - K)$ colours (Fig.4.4). Actually the (V-K) colour of a source corresponds to its spectral type. The zero magnitude UD angular diameter ($\mathrm{UD}_{V=0}$) of sources for a particular spectral type, should be equal theoretically. This is because the sources with same spectral types have a constant absolute magnitude and their linear diameters will also be same. Hence, the zero magnitude angular diameter of a source can be derived from

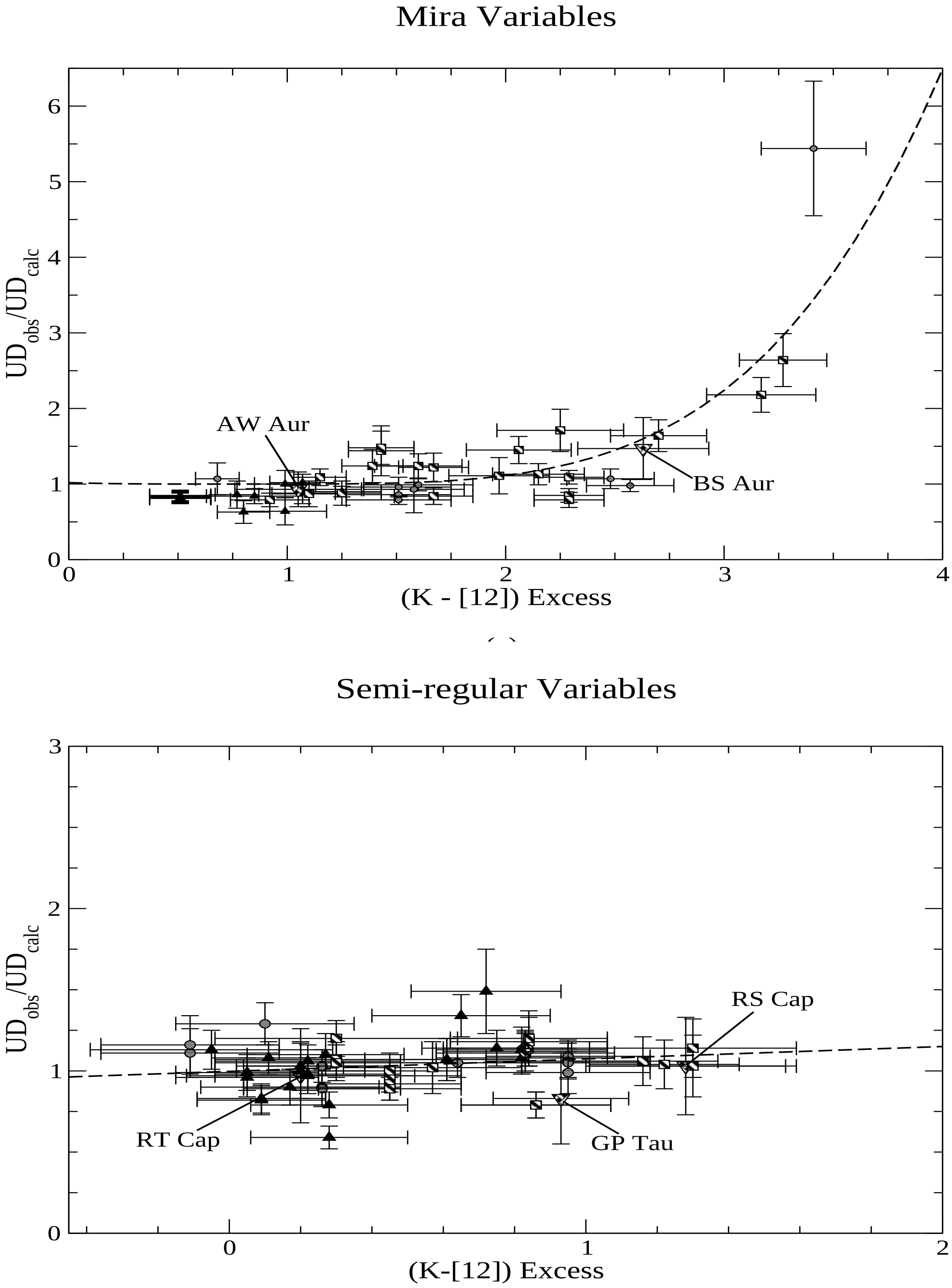

(b)

Figure 4.5: The $(K-[12])$ colour excess vs. the ratio of observed and calculated angular diameters for both Mira variables (a) and Semi-regular variables (b) as described in the text. The dotted lines show a polynomial through the points to indicate the rising trend. Our observed sources are also plotted and labeled.

the linear regression of the plot of (V-K) vs. $UD_{V=0}$. We have also derived a similar relationship for SRVs using 83 sources from the same catalog (Fig.4.4). We obtained a good linear least squares fit in both the cases and a good correlation is obtained in both cases (correlation coefficients of 0.94 (Miras) and 0.98 (SRVs)). It must be pointed out that the errors involved in the angular diameter predictions by these methods is in the range 20 to 25 % due to difficulties of obtaining contemporaneous photometry. Nevertheless the method outlined appears to have a good predictive value for angular diameters using only $(V - K)$ colour for both Miras and SRVs.

The predicted UD angular diameters for our 5 sources are listed in third column of Table.4.3. It is seen that there is a good agreement in general between our measured values and predictions. However, in case of RT Cap the prediction gives a lower value. It must be pointed out that RT Cap is a carbon rich semi-regular variable, and so it cannot be readily compared with generally oxygen rich SRVs used in the calibration curve.

4.4.2 Enhancement of Angular diameter due to Mass loss/shell effects in Miras

As mentioned before that the AGB variables suffer from the huge mass-loss rates in the range of about 10^{-7} to 10^{-6} $M_{\odot}$/yr. It finally results in the circumstellar shells around these stars. In the model fit of the lunar occultation we assume that the source is uniformly illuminated circular disk which is not entirely realistic. The circumstellar shell also contributes to the observed K-band flux. Hence, there is a possibility to over estimate the stellar angular diameter of the source if substantial amount of material is present around the star. So, an investigation on the possible enhancement in UD values due to the mass-loss/circumstellar shell has been carried out. However, this aspect of enhancement of UD angular size of Mira variables due to mass loss was discussed earlier by van Belle, Thompson & Creech-Eakman (2002). These authors had derived, for a sample of Miras, the ratio of linear radius (obtained from angular size measurements and distance estimates) to the theoretical (Rosseland) radius assuming that Miras are all fundamental mode pulsators. A plot of this ratio as a function of $(K - [12])$ colour excess which is indicative of mass loss showed that Miras with higher colour excess were systematically 120 $R_\odot$ larger than their counterparts with lower colour excess, independent of the periods.

We have adopted a slightly different approach using a sample of 43 oxygen rich Miras with spectral types later than M5. In order to avoid the large errors involved in distance measurements we plot the ratio of observed and calculated angular diameters against $(K - [12])$ colour excess. The K-band (2.2 μm) magnitudes and 12 μm fluxes are collected from 2MASS catalog (Cutri et al., 2003) and IRAS catalog (Helou & Walker, 1986) respectively. The K-band and 12 μm is selected for the investigation because the K-band fluxes are radiated from the hotter region near the photosphere, while substantial 12 μm fluxes come from the cool circumstellar dust, if present. Hence, if a source has an excess in the (K-[12]) colour than its black-body radiation corresponding to its photospheric temperature (T_{eff}), it indicates the presence of the circumstellar shell around the star.

First the effective temperatures for all the sources were collected according to their spectral type from Alvarez & Mennessier, 1997. Then, the (K-[12]) colour and angular diameter has been calculated for the corresponding temperatures. The excess in (K-[12]) colour ($(K - [12])_{excess}$) is obtained by subtracting the $(K - [12])_{bb}$ from $(K - [12])_{obs}$. The angular diameters are obtained from the temperature (T_{eff}) and bolometric flux (F_{bol}) by using the formula -

$$UD_{cal} = \left[\frac{4F_{bol}}{\sigma T_{eff}^4}\right] \tag{4.1}$$

The calculated UD angular diameter (UD_{cal}) is independent of the distance. The bolometric fluxes are calculated using the mean relation between bolometric flux, K-band flux and $(V - K)$ colour as reported by Dyck, Lockwood & Capps (1974) Finally, the ratio of the ${}^{UD_{obs}}/_{UD_{cal}}$ is plotted against $(K - [12])_{excess}$ (Fig.4.5) to see if any trend is being followed. The UD angular diameters are collected from the CHARM2 catalog (Richichi et al., 2005).

The plot shows that the ratio remains close to unity upto a colour excess $\sim$ 2.5, and then increases sharply. For a colour excess of $\sim$3 the measured UD diameter is almost twice the calculated value. The measured UD diameter of AW Aur is in good agreement with the calculated value showing a ratio $\sim$1. However the observed value of BS Aur is almost 1.4 times the calculated value (Table.4.3, column 4). We have also plotted the positions of our sources (AW Aur and BS Aur) in Fig.4.5 which suggests that BS Aur has a high mass loss rate and may harbor a shell. This is also borne out by the IRAS LRS characterization (Halue & Walker, 1988) of these two stars. According to this characterization, AW Aur (LRS Char 15) does not have any detectable circumstellar shell but BS Aur (LRS Char 28) has a thin *o*-rich shell around it.

Following the above procedure we have also carried out a similar investigation for SRVs using a sample of 52 K-band angular diameter measurements (later than M5) taken from Charm2 catalog (Richichi et al., 2005). The SRVs in the sample have a $(K - [12])$ colour excess less than 1.5 (unlike Miras) and the ratio close to unity (Fig.4.5). It appears unlikely that SRVs may exhibit enhancement in their angular diameter.

Using the available distance estimates and our measured angular diameters of each of these sources given in the Section.4.3 we have derived the linear radii of the sources corrected for enhancement. With a reduction of 40% of the enhanced size of BS Aur we find that both Miras have a similar radii (Table.4.3, column 5). However, it may be pointed out that due to large unknown errors in distance to these sources the absolute errors involved in linear radii could be much higher. Hence it is difficult to draw any conclusion regarding the mode of pulsation of these two Miras.

It is speculated that SRVs can pulsate in a number of modes and that too often simultaneously (Lattanzio & Wood, 2003). However, in the absence of reliable distance measurements it is difficult to draw definitive conclusions from our angular diameter measurements.

Table 4.3: Results.

Source	Obs. θ_{UD} (mas)	Pred. θ_{UD} (mas)	Ratio $\frac{UD_{obs}}{UD_{calc}}$	Linear Radius (Corrected) ($R_\odot$)
AW Aur	4.33±0.50	4.0±1.0	1.1±0.1	440±100
BS Aur	5.00±0.70	4.5±1.2	1.4±0.2	470±110
GP Tau	4.85±0.50	6.1±1.5	0.8±0.1	175± 40
RS Cap*	7.70±0.50	8.3±2.1	1.0±0.1	230± 40
RT Cap	8.14±0.30	5.4±1.3	1.0±0.1	490± 70

4.5 Conclusions

K-band uniform disk angular diameters of two Mira variables and three Semi-regular variables (SRVs) are reported. For the two Miras and one SRV (GP Tau) these are the first time angular diameter measurements. For the other two SRVs our values are in good agreement with those reported earlier. Two separate comparative studies have been made to examine our measured values with predictions. One of the methods involves a separate calibrations for Miras and SRVs with previously reported K-band diameters and $(V-K)$ colours. In this case we find a good agreement between measurements and predictions except for one SRV (RT Cap) which is a carbon star. We have also investigated the enhancement of measured UD angular diameter due to heavy mass loss and the presence of a circumstellar shell as indicated by $(K-[12])$ colour excess. We find AW Aur is unlikely to harbor a shell. But for the other Mira in our sample (BS Aur) UD angular diameter measured appears enhanced by nearly 40% compared to the expected value due to presence of a circumstellar shell arising out of mass loss.

Chapter 5

Exploration of Noise reduction methods in observed LO light curves

5.1 Noise in LO light curves

It has already been discussed (in Chapter 2) that Lunar Occultation (LO) observations require high speed photometry of sampling in the milliseconds range to record well defined fringe patterns. A good signal to noise ratio (S/N > 40) is essential to extract the proper angular diameter information of the source from the observed light curve. A LO light curve with very good S/N in the fringe region can also be investigated for signatures of circumstellar material surrounding the star. Also detecting finer structure information of the inner dust shell of sources, for example WR 104, IRC + 10216 (Mondal & Chandrasekhar, 2002; Chandrasekhar & Mondal 2001) is only possible with good light curves. However, the fast sampling and good S/N are two contradictory requirements and they set a limit on the magnitude of observable sources using LO technique. With our instrument (NICMOS sub-array) the sources upto $m_K \sim 5.0$ are observable under excellent sky conditions. Noise appears as a random variation of the registered signal level. The sources of noise in the LO light curves at 2 μm are (1) scintillation noise, (2) photon noise or shot noise from both source and the sky, (3) Read-out noise and (4) Thermal background noise. Noise power also arises at specific frequencies from electrical line pickup (50 Hz and its harmonics/sub-harmonics) and also from detector (readout) electronics (31 Hz).

We begin this chapter with a discussion on noise encountered in LO light curves. We then discuss two methods based on Fourier and Wavelet transforms to reduce the noise in LO light curves and thereby improve S/N. We first give a brief introduction to these techniques as applied to the LO light curves.

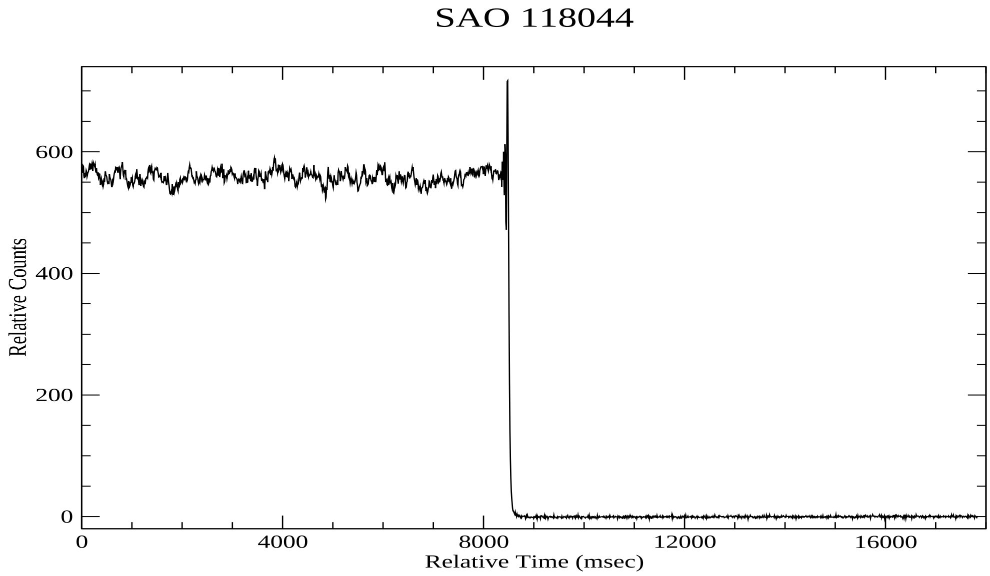

Figure 5.1: The light curve of one of the brightest source SAO 118044 ($m_K = 0.49$) in our sample shows a different noise pattern before and after occultation. The first part of the light curve (before event) is dominated by source photon noise and low frequency scintillation noise. But the second part of the light curve (after event) is purely dominated by background noise.

5.1.1 Scintillation Noise

When a plane wavefront coming from a distant star is incident on the earth's atmosphere, due to variable refractivity in different layers of the atmosphere, the wavefront is deformed in a random manner. This finally causes a temporal variation in the apparent brightness of the source. This phenomena is

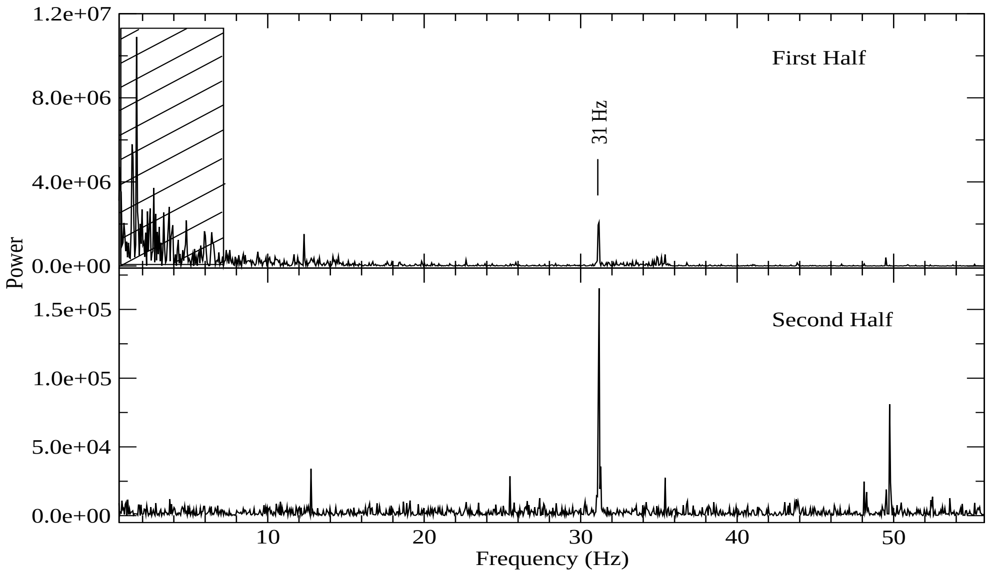

Figure 5.2: The power spectrum of the LO light curve of SAO 118044 shown in Fig.5.1. The upper panel shows the power spectrum of the first half of the light curve (before occultation) and the lower panel shows the power spectrum of the second half. First half of the light curve is dominated by scintillation and source photon noise. There are many low frequency components as seen inside the shaded box. In the second half they did not contribute.

termed *atmospheric scintillation*. Wind, turbulent air and temperature gradients in different layers of the atmosphere, which cause small scale variations in air density, play important roles in fluctuating the refractive index of the atmosphere and hence the scintillation as well. The phase variation of the incoming light due to the variable refractive index of the earth's atmosphere is characterized by spatial and temporal parameters. The circular air parcel size which causes one radian rms variation of the incoming wavefront is the spatial scale to determine the atmospheric condition. It is called Coherence length (r_o) or Fried parameter (Fried, 1966). At the visible wavelengths the typical size of r_o is about 10 cm under good 'seeing' conditions. The statistical theory of Kolmogorov atmospheric turbulence model leads to the conclusion that r_o increases with wavelength and it is proportional to $\lambda^{6/5}$ (Fried 1966). At near infrared K-band (2.2 μm) the value of r_o is about 50 cm (Léna et al., 1998). So, the scintillation effect is more prominent in the visible range than the NIR because the visible light passes through more effective air parcels than the NIR. The temporal scale is defined by the time taken to blow away the air parcel sized of coherence length by the wind across the telescope. So, the coherence time can be written as $t_0 = r_0/v_{wind}$. At visible wavelengths the *coherence* time is about 10 msec at good sites while at 2.2 μm it is about 50 msec by assuming wind velocity of 10 m/sec.

The phase fluctuation of the incoming wavefront is related to the *seeing* while the scintillation corresponds to the amplitude fluctuations. Scintillation does not cause the blurring of the star images but changes only the apparent brightness level of the objects. Scintillation effect can be averaged out either by longer integration or by using a larger telescopes aperture. The scintillation is more prominent in smaller telescopes upto ∼1m due to edge effects. In our case, the LO light curves are sampled in ∼9 milliseconds and operated telescope aperture is 1.2 m, so the scintillation will cause a low frequency variation in the signal levels of the LO light curves. The effect is more near the horizon than the zenith because the star light has to pass through more effective parcels of air when it is near horizon. The low frequency noise pattern is demonstrated in Fig. 5.1 (first half of the light curve) which may include the scintillation noise as well as minute telescope oscillation. The corresponding power spectrum is also shown in Fig.5.2. The upper panel in the figure represents the power spectrum of the first half of the light curve. While the lower panel shows the power spectrum of the second half. The first half of the light curve is dominated by low frequency noise (shaded in figure), when the source is present. But in the second half of the light curve, these low frequency components are absent.

5.1.2 Photon Noise

Photon noise (also called Random noise) arises due to the intrinsic natural variation of the emitted photon flux coming from the star. In near Infrared a large photon noise is also contributed by back-ground sky within the 10×10 pixels sub-array. Source photon noise is a natural contribution of noise from

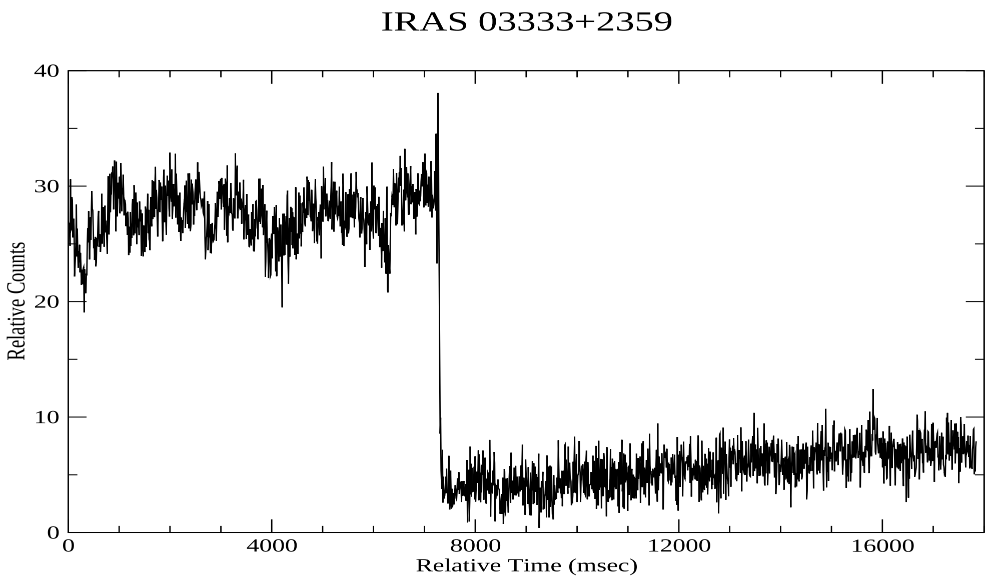

Figure 5.3: The light curve of IRAS 03333+2359 ($m_K = 5.07$) shows a similar noise pattern before and after occultation. Also low frequency modulation ($\sim$ 1.5 Hz) is seen in first half of the light curve when the source is present.

the source, and will always be present in the signal. Even the perfect detector is limited by the photon noise. Detection of photons follow the Poisson's statistics. So, if the source photon noise is the only contribution of noise in the light curve then expected S/N of the light curve is $\sqrt{(n_{phot} \times t_{int})}$ where n_{phot} is average photon rate and t_{int} is integration time. That is why, the effect of the source photon noise is more prominent in the light curves of brighter sources. Examining the occultation light curves, we found that the change over in the dominating noise from source noise to back-ground noise takes place at m_K of about 3.3 under good sky condition and at good altitude of the observation of the source ($\geq 40^o$).

5.1.3 Read-out Noise

The read-out noise is a consequence of the imperfect operation of physical devices in the detector system. Detectors periodically measure the charges accumulated in pixels since the last measurement. The electron charge measuring process has an associated fluctuation which adds noise in the signal.

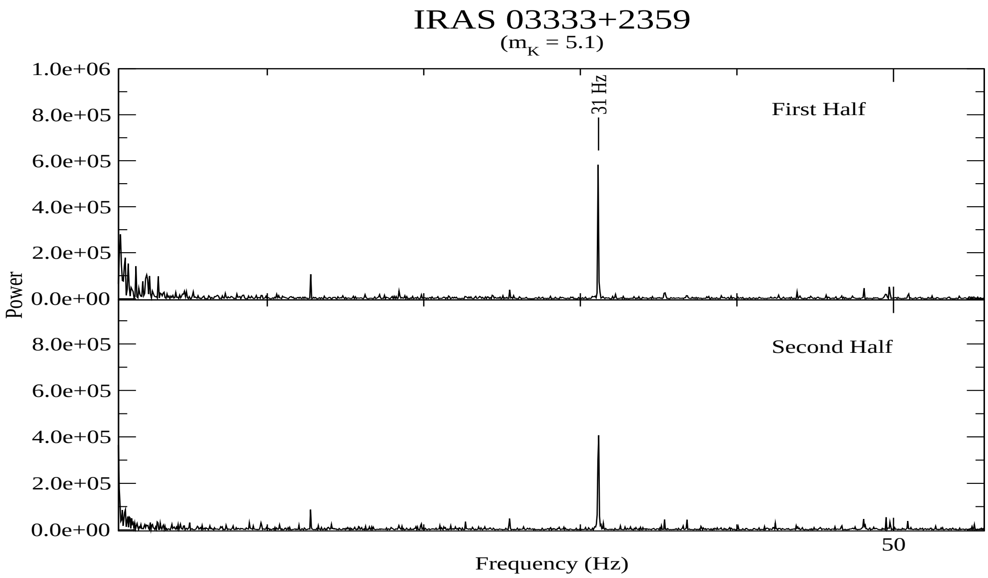

Figure 5.4: The power spectrum of the LO light curve of IRAS 03333+2359 (m_K ~5.1). The upper panel shows the Fourier transforms of the first half of the light curve (before occultation). While the lower panel shows the Fourier transform of the second half of the light curve. Both the part is dominated by the specific frequency noise (31 Hz).

All the pixels in the detector array are not identical and their performances too are not uniform. The inhomogeneity in their nature and performance adds noise in the observed signals. The 'read-out noise' not only arises from the detector array but also from the associated electronics (Christian Buil, 1991).

The digitization of the analog signal also introduces noise in the signal. In the digitization process the analog signal is sliced into a finite number. For any given amplitude, there is a corresponding number of a slice which is saved in the computer. So, the process is approximating the infinite number of possible analog values into a finite amount of information. This is termed as Analog to Digital conversion (ADC) noise.

When a charge packet moves along the array or associated electronics, a fraction of the charge can be left behind. It depends on the quantity of the charge in the packet. This is called $Transfer$ noise. Also the readout diode is brought to a reference voltage before reading a new packet (i.e; 'reset' the array). A small fluctuation in the 'reset' voltage of the array tends to add noise in the observed signal.

5.1.4 Thermal Back-ground Noise

The sensitivity of the near infrared observations is usually limited by the noise from the terrestrial sources of photons. There may be contribution from the night airglow, thermal emission from the optics, scattered lights from the telescope and scattered moon light as well. The main contamination in the NIR comes from the air-glow due to the chemical reactions in the upper atmosphere (a main component is OH), the thermal emission from the atmosphere, the telescope as well as related optics. That is why, a NIR detector receive radiation even if it is exposed to complete darkness. The thermal background (at 300 K) also begin to contribute to the noise in the K-band and beyond.

The thermal noise from the detector and electronics is kept low by cooling them in the dewar to 77 K.

5.1.5 Noise at specific Frequencies

The electrical power line pick-up (50 Hz) and an unknown 31 Hz noise contribution from the detector electronics often adds noise to the observed LO light curves. It can be seen in Fig.5.2 that 31 Hz is present in the power spectrum with large power. The power spectrum of the light curve of fainter source IRAS 03333+2359 ($m_K \sim 5.1$) is shown in Fig.5.4 and the corresponding light curve is also shown in Fig.5.3. The power-spectrum shows that the most dominating frequency is 31 Hz and it is present in both halves of the light curves independent of brightness of the object. But in the case of bright objects, the first half of the power spectrum is dominated by low frequency noise. A few test runs with closed filter (detector looking only at cold (77 K) back-ground and also detaching the detector system from the telescope have been carried out. Here also 31 Hz is present with dominating power. Attempts were made to trace of the 31 Hz noise. It was ascertained to originate from detector electronics.

Attempts to eliminate it in the hardware were not successful.

One of the investigations carried out in this thesis is the study of methods to improve S/N of the observed LO light curves by reducing or eliminating the noise content. Noise reduction technique on the LO light curves is extensively discussed later in this chapter.

Initially a sample of 66 light curves upto $m_K \sim 5.0$ observed during the period 2008 to 2011 were chosen to perform the exercise. Then 12 sources were rejected due to very noisy and highly distorted light curves. Finally, the method was applied on a sample of 54 light curves listed in Table.2.5 (Chapter 2).

5.2 Fourier Denoising method

Any stationary signal can be decomposed into its component frequencies using the Fourier Transforms (FT). It converts any signal from time-amplitude to frequency-power domain. However, the time information of the signal is lost in the frequency domain; which means, the specific time of occurrence of any particular frequency is completely lost. With the help of Fourier transforms one is able to get the frequency informations upto *Nyquist* frequency. Above the *Nyquist* frequency aliasing effect will be seen. Nyquist frequency is quantified by $1/2t$, where t is the sampling interval. In present case most of the light curves are sampled with 8.926 milliseconds at the *Nyquist* frequency of 56.0 Hz. In our LO light curves specific well identified noise frequencies like 31 Hz, 50 Hz and their sub-harmonics are present (see Section.5.1 for more details). Hence, it is useful to apply Fourier transforms to remove these frequencies. The Fourier denoising (FD) method is applied to our sample consisting of 54 observed light curves (Table.2.5). A set of 4096 data points for each light curves have been used for the transformations.

The very initial and fundamental problem in applying the FT on LO data is the characteristic of FT itself. The Fourier Transform of a step function (Fig.5.5) composed of all possible frequencies with rapidly decreasing power

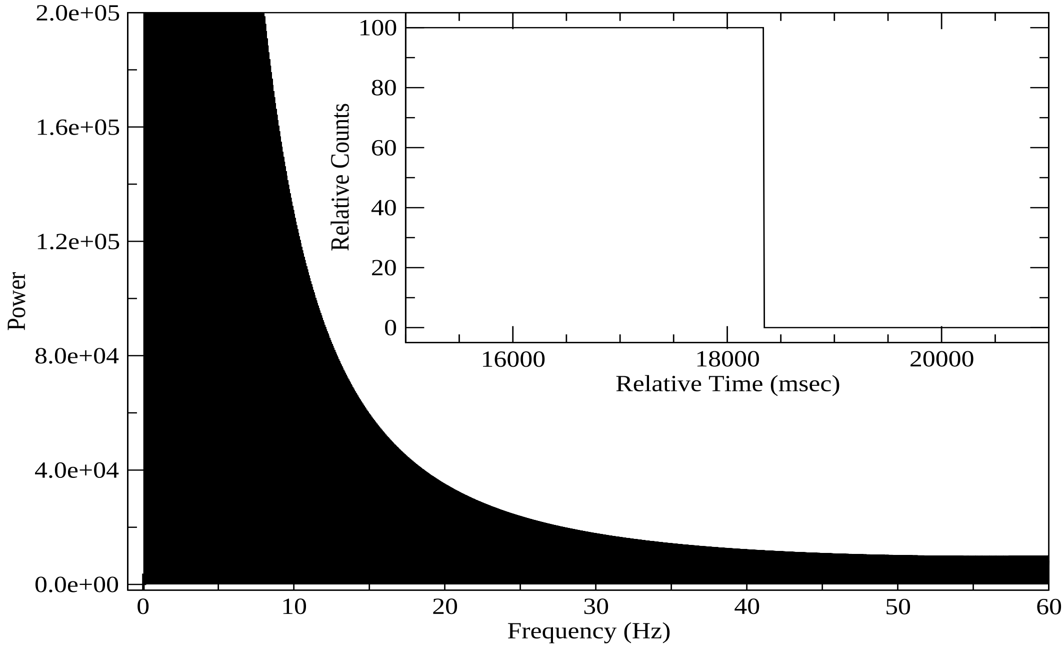

Figure 5.5: A step function (inset) and its power spectrum. The power-spectrum shows rapidly decreasing power towards higher frequencies.

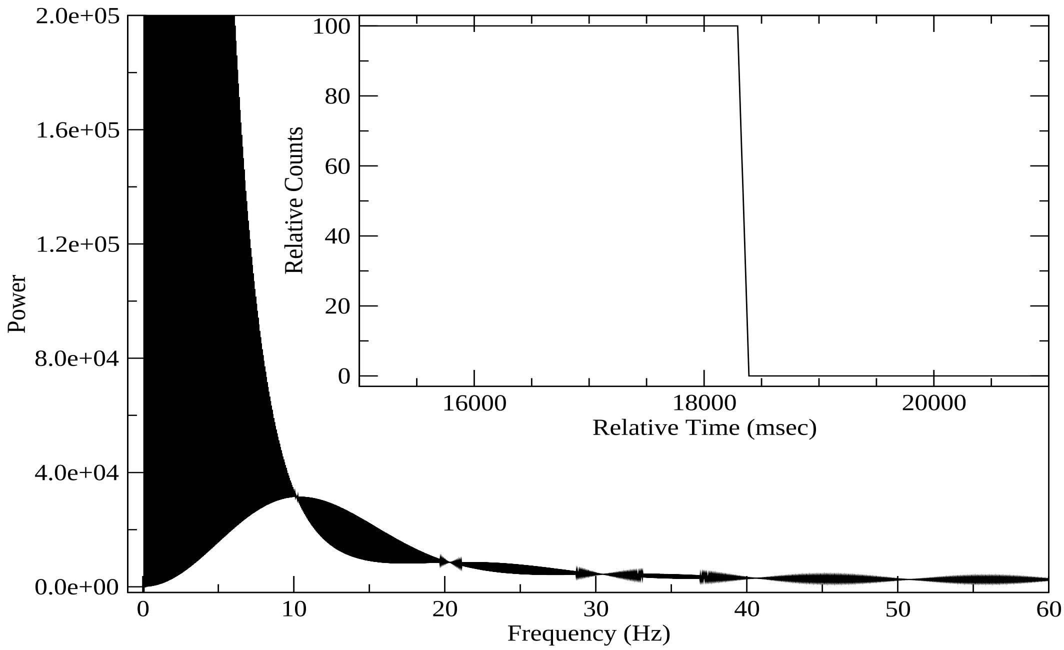

Figure 5.6: A step function with slope (inset) and its power spectrum. The power-spectrum shows a oscillatory behavior along with the rapidly decreasing power.

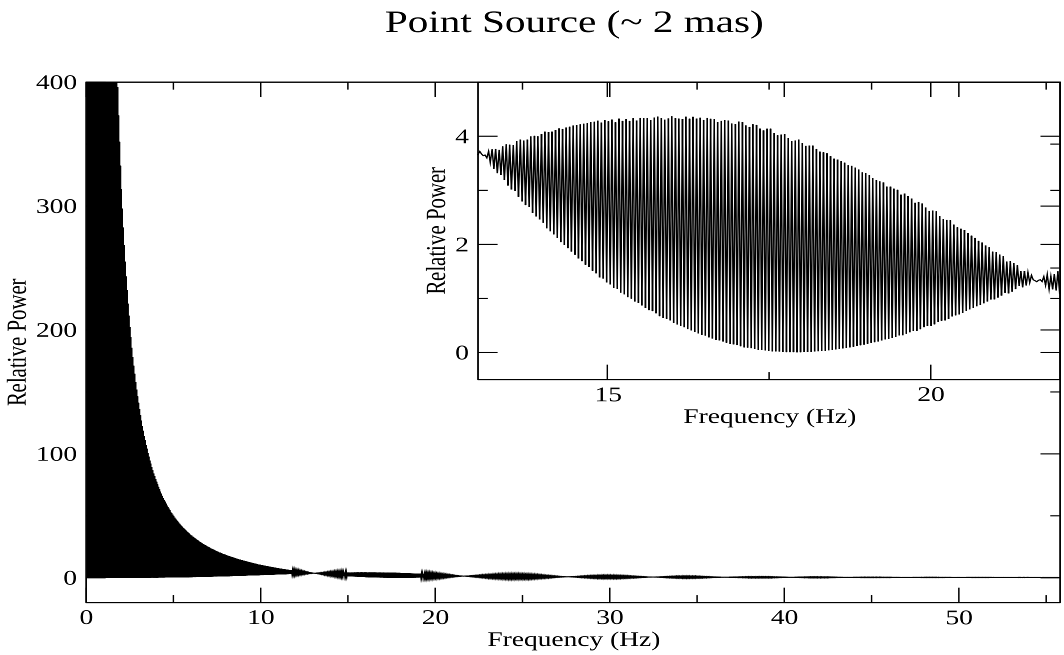

Figure 5.7: The power spectrum of model light curve shows similar nature as it is for the step function with slope (Fig.5.6).

(i.e.; positive X-axis part of the Sinc function) from low frequencies to high frequencies. While a step function with slope shows two kinds of variation in the Fourier domain. One is rapidly decreasing power towards the higher frequencies and second is a low frequency variation associated with it (Fig.5.6). The lower frequency variations change with the slope in the step function. The signal level in LO light curves also changes before and after the occultation like a step function, hence, FT of this data shows a similar kind of characteristic in the Fourier domain. The Fourier Transform of a model light curve with uniform disk angular diameter value of 2.0 mas is shown in Fig.5.7. In the Fourier domain those two patterns mentioned above are clearly visible and a zoomed portion of the power spectrum is also shown as inset for clarity. The high frequency oscillations in the power spectrum arises due to step function like shape of the light curve. The low frequency modulation in the power spectrum is obtained from the nature of falling of the light curve. Flatter the slope in the light curves higher the frequency of second type variation. So, this implies that even the well identified noise frequencies are not easy to remove

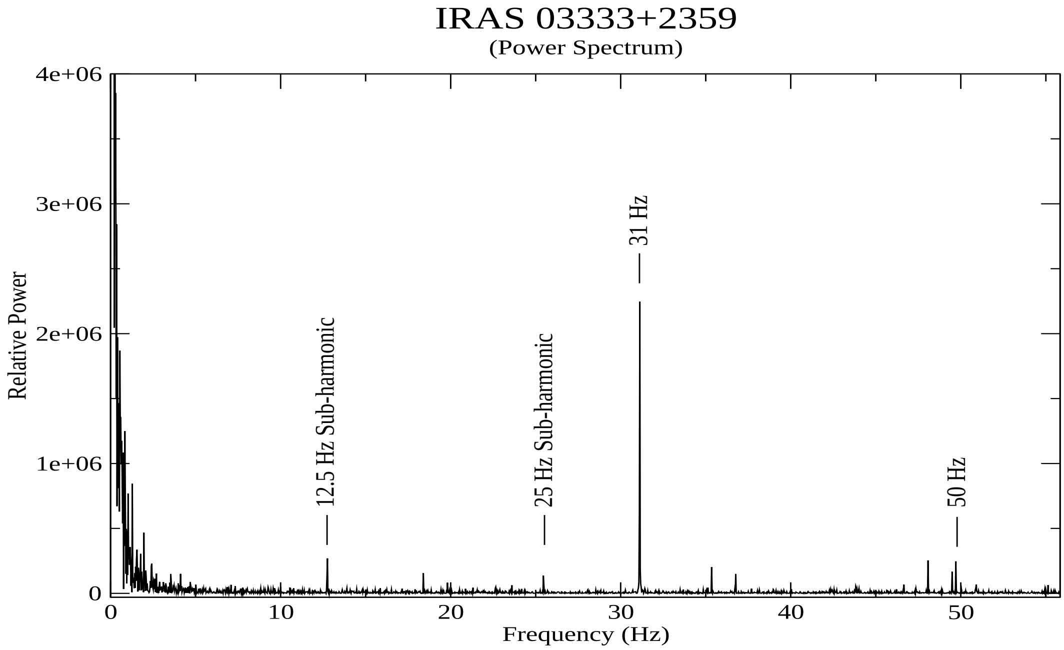

Figure 5.8: The power-spectrum of the observed (raw) LO light curve of IRAS 03333+2359. Apart from the rapidly decreasing power spectrum few well identified noise frequencies like 50 Hz and its sub-harmonics, 31 Hz, and 36 Hz with its sub-harmonics are visible which have been removed from the light curve.

completely, as a little part of it is always contributing to define the shape of the light curve itself. The effect is higher in the low frequency regime ($<$ 10 Hz) of the power spectrum. The frequencies greater than 10 Hz can be removed completely from the light curves without any significant change in it.

The power-spectrum of an observed light curve of the source IRAS 03333+2359 (Fig. 5.8) shows a noisy pattern than a modelled one. A few well identified noise frequencies, like 50 Hz power line pick-up, its sub-harmonics, and 31 Hz etc, are seen in the spectrum. It also occasionally happens that fringe frequency almost matches to the low frequency fluctuations in the signal. It has been noticed that 31 Hz noise frequency is present almost in the all the light curves and it contributes dominating power in many sources (mainly fainter objects). The main targets in Fourier denoising (FD) method were these two (31 Hz & 50 Hz) well identified noise frequencies and their sub-harmonics. But in few cases some other frequencies, with dominating power, have also been

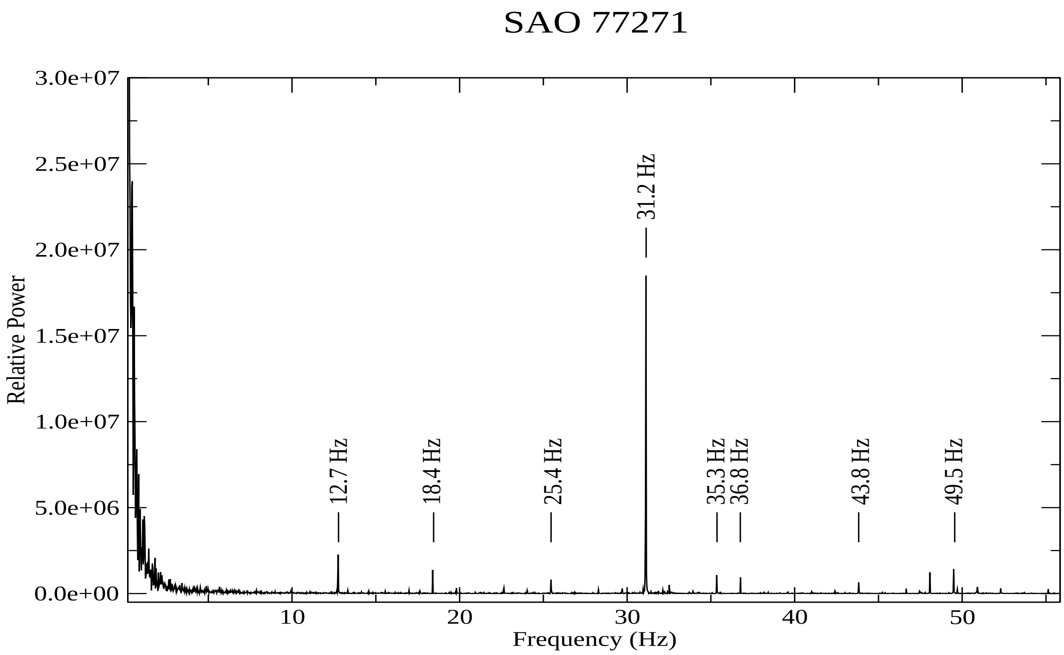

Figure 5.9: The power spectrum of the observed (raw) light curve of SAO 77271. The frequencies, marked in the spectrum, are removed from the light curve applying the FD method.

removed from the light curves. A $MATLAB$ programming script was written and used to pursue this method. The method was applied on all the 54 sources listed in Table.2.5. One example of the source SAO 77271 before and after the application of FD method has been shown in Fig. 5.10. The power-spectrum of the corresponding light curve is also shown in Fig. 5.9. The removed frequencies are marked in the power spectrum. Removal of those frequencies enhanced the S/N of the light curve from 32 to 55.

A histogram plot of S/N vs Number of sources for both observed (*Raw* hereafter) (upper) and FD (lower) is displayed in Fig 5.11. It is seen that FD method has improved the S/N, but not dramatically. A small number of sources with lower S/N have moved towards the S/N >40. To demonstrate this point more clearly the cumulative distribution plot of the same is shown in Fig. 5.12. The dotted curve in the cumulative plot corresponds to the *Raw* set of light curves, while the solid line is for FD processed data set. It represents a plot of S/N vs. the accumulated percentage of sources below any particular

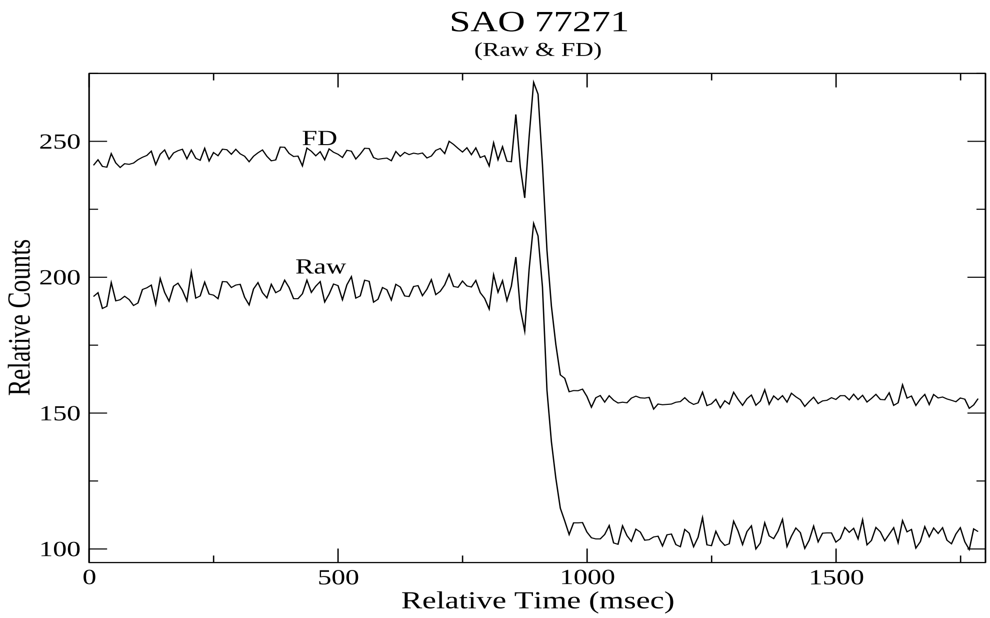

Figure 5.10: Raw and Fourier denoised light curves of SAO 77271. The FT denoised light curve is shifted upward by 15 counts for clarity. The denoised light curve can be clearly seen to have lesser noise than the original ('Raw') data.

S/N. For instance, 70% of the sources were below S/N of 40 before denoising method (i.e, Raw data). After the application of FD method only 55% of the sources were below S/N of 40. But with the help of Fourier transforms only few specific noise frequencies can be removed. Fluctuations for a limited period may also present in the light curves which would contain lesser power in the frequency-power domain. Hence, it is difficult to identify and remove them individually. Handling of these noisy light curves motivated us to investigate the use of wavelet transforms.

5.3 Introduction to Wavelet Transforms

The basic meaning and nature of a wavelet is coded in its nomenclature itself. 'Wavelet' implies a small wave which oscillates for a limited duration with respect to zero. In the same time it should also satisfy two specific conditions : (1) it should integrate to zero and (2) the energy should be finite. So,

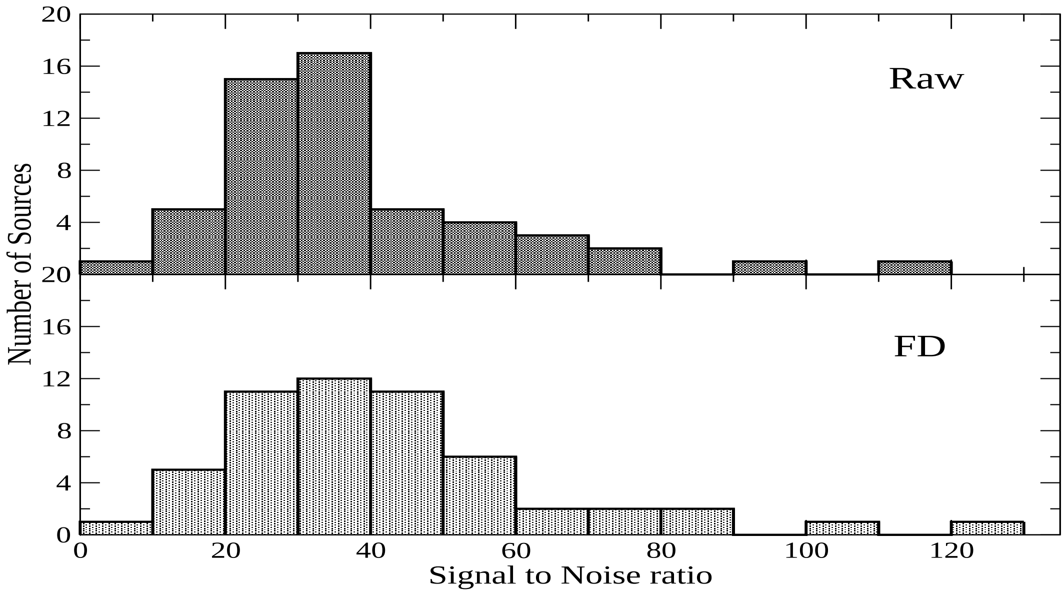

Figure 5.11: The Histogram shows that nine sources improved to S/N > 40 after the application of Fourier Transform method.

mathematically if $\psi(t)$ is a wavelet then,

$$\int_{-\infty}^{\infty} \psi(t) = 0, \tag{5.1}$$

and

$$\int_{-\infty}^{\infty} |\psi(t)|^2 < \infty. \tag{5.2}$$

Wavelets are capable of having any kinds of shape just by satisfying two conditions mentioned above. The wavelets are generally irregular and non-symmetrical and also oscillates for a limited period of time. That is why wavelets are better in describing the irregularities or any sudden changes occurred in the signals. The idea of wavelet first came up in 1909 in the thesis of Haar where he mainly worked with sets of orthogonal basis functions to represent a signal which is basically a consequence of the Fourier Transform where sine and cosine form the orthogonal basis. The improvement in the basic theory of the wavelet is started only after 1970s and few notable contributions made by Grossman and Morlet (1984), Daubechis (1992) and many others. A

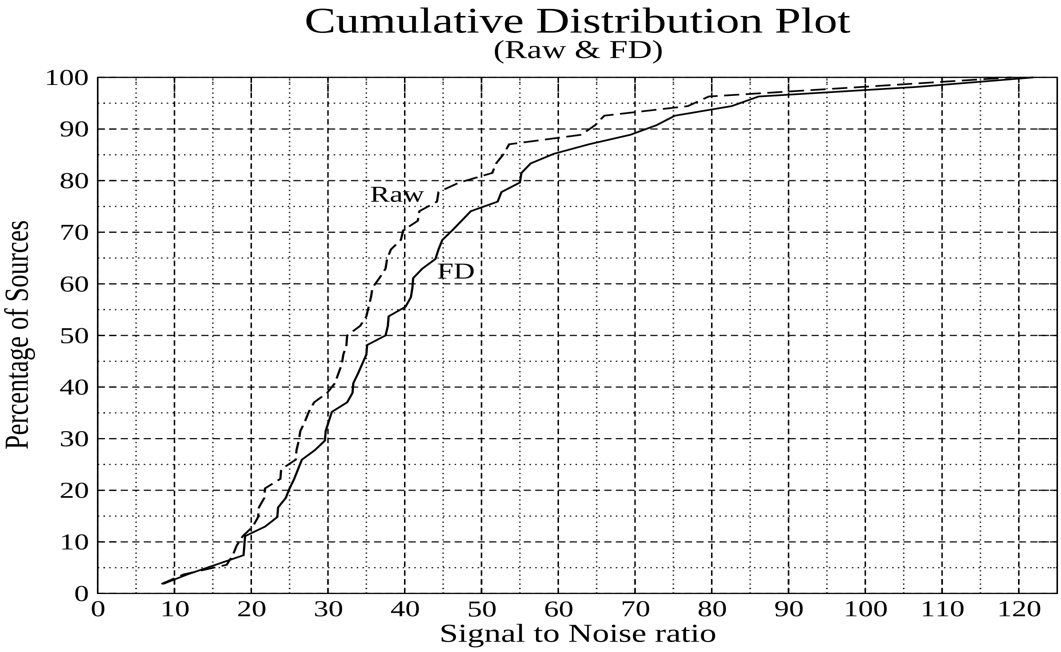

Figure 5.12: The dotted line is the cumulative distribution plot of Raw light curves. It has been shifted towards right hand-side (solid line) after the application of FD method. For example before application of the denoising method, 70% sources had $S/N < 40$. After the application of the method only 55% of the sources have $S/N < 40$.

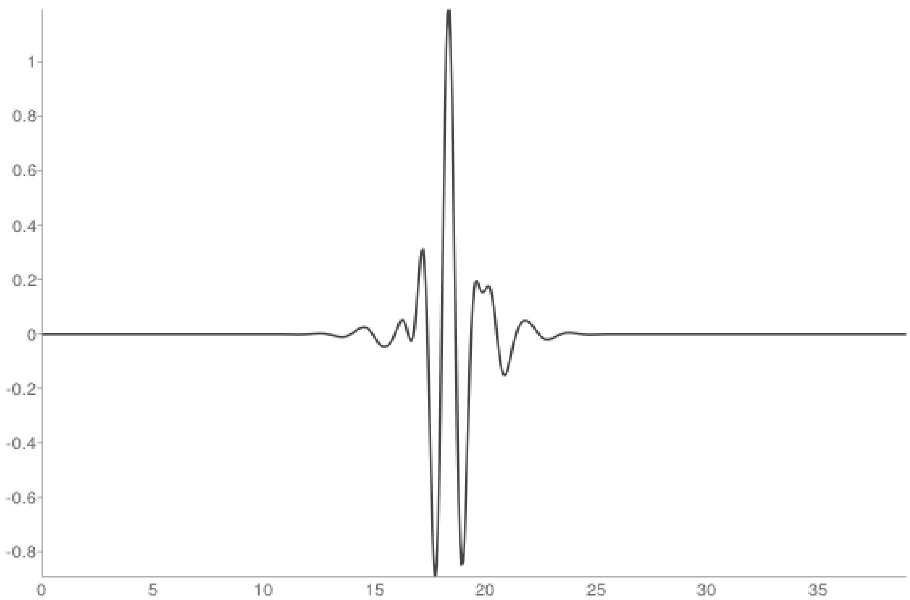

Figure 5.13: An example wavelet of Symlet family. X-axis of the curve represent the number of data points (or time). Y-axis is the relative amplitude.

general form of a wavelet can be expressed as,

$$\psi_{ab}(t) = \frac{1}{\sqrt{|a|}}\psi(\frac{t-b}{a}). \tag{5.3}$$

The parameter a is called scaling parameter and b is called shift parameter. Width of the wavelet is changed with the help of parameter a and the wavelet is translated to different position by changing the parameter b. The wavelet for maximum possible scaling function is termed as $Mother\ wavelet$. Changing the scale parameter 'a' the thinner and thinner $Daughter\ Wavelets$ can be generated. But they should be orthogonal to each other and as well as to $Mother\ Wavelet$.

An example wavelet is displayed in Fig. 5.13. The inner product of a wavelet with a signal gives the nature of the signal for that time-zone where the wavelet exists and the rest will give zero as wavelet itself is zero there. Hence, by shifting the position of the wavelet the signal is decomposed for different time and similarly, by changing the width of the wavelet different frequency levels are accessed. This capability of wavelet made it a powerful and more acceptable tool to examine the nature of any signal and analyze it. Now, if f(t) is a square-integrable function then the wavelet transform of it can be written as

$$W(a,b) = \int_{-\infty}^{\infty} f(t)\frac{1}{\sqrt{|a|}}\psi^{*}(\frac{t-b}{a}). \tag{5.4}$$

This particular wavelet transform is known as Continuous Wavelet Transform (CWT).

5.3.1 Discrete Wavelet Transforms (DWT)

In CWT we have seen that any wavelet can be represent in terms of mathematical functions. Inner product of any wavelet with a finite valued function produces the wavelet coefficients which is an indicator of signal pattern with respect to that particular wavelet. But all the real life data is composed of discrete data points and most of them cannot be expressed in terms of mathematical functions. Decomposition of real life data requires Discrete Wavelet Transformation (DWT).

In discrete wavelet transformation one *Father* wavelet is also introduced along with *Mother* and *Daughter* wavelets. The *Father* wavelet (sometimes named as scaling function) acts as low-pass filter and corresponding mother and daughter wavelets act as high-pass filters of different frequency levels depending on their width. The DWT actually uses four filters in the transformation, namely, low- and high-pass decomposition filters and low- and high-pass recombination filters. In decomposition process it produces two types of coefficients: (1) average coefficients (ca) and (2) details coefficients (cd) with the help of low-pass and high pass filters respectively. The average coefficients (ca) hold the basic structure of the signal while details coefficients (cd) are the fluctuations with respect to ca. The decomposition procedure is demonstrated in Fig. 5.14. First the signal (S) is decomposed in two sets of coefficients, $ca1$ and $cd1$. To acquire more informations on lower frequencies $ca1$ is further decomposed into $ca2$ and $cd2$ and it can be repeated further. In Fig. 5.14, a 4^{th} level decomposition process is demonstrated.

In case of Discrete Wavelet Transforms the parameters a and b (see equation 5.3) change their values as 2^k where k is an integer. This does not mean that DWT is under-sampling the data during the transformation but it is basically avoiding the coefficients which do not effectively contain any significant information of the signal. According to the *Nyquist–Shannon* sampling theorem, if f_m is the highest frequency content in a signal, then it can be completely determined if it is sampled in $1/(2f_m)$ seconds. So, it implies that not all but alternate data points are required in further analysis and that is what is happening in DWT. Hence, using DWT, one is able to decompose the signal, filter it and again recompose it. If $\psi_{j,k}(t)$ is wavelet and $\phi_k(t)$ is scaling function then the decomposition of a signal f(t) can be expressed as (Nanavati & Panigrahi, 2004),

$$f(t) = \sum_{k=-\infty}^{\infty} c_k \phi_k(t) + \sum_{k=-\infty}^{\infty} \sum_{j=0}^{\infty} d_{j,k} \psi_{j,k}(t), \tag{5.5}$$

and the corresponding wavelet is expressed as

$$\psi_{j,k}(t) = 2^{j/2} \psi(2^j t - k). \tag{5.6}$$

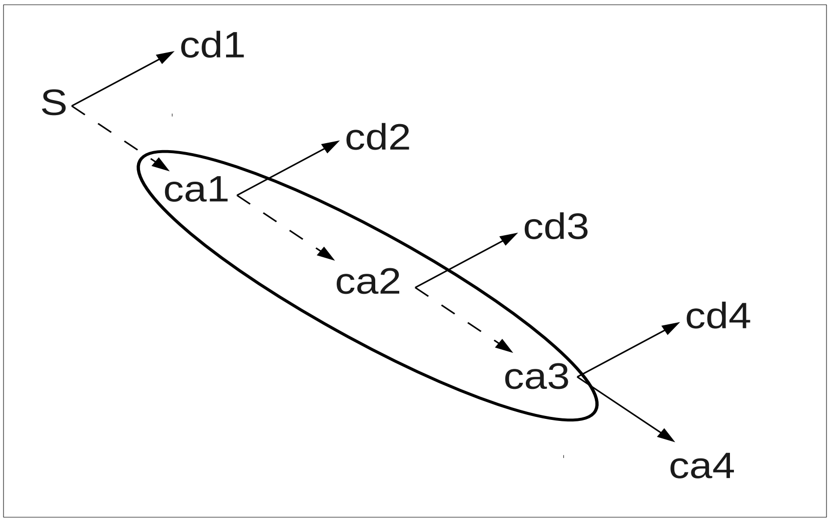

Figure 5.14: Decomposition process in Wavelet Transforms. First level decomposition produces a set of high-pass or detailed coefficients (cd1) and low-pass or average coefficients (ca1). To acquire more information ca1 are again decomposed to produce cd2 & ca2 and so on. The fourth level decomposition is shown here. The 'average' coefficients marked inside the ellipse are further decomposed and do not come as output.

More details on wavelet transforms can be found in Lee Fugal (2009).

5.4 WT Application on LO data

The *MATLAB* wavelet tools and scripts written by us have been used to pursue the noise reduction of the LO light curves. Many mathematical forms of wavelets are present in the literature. Also generating user defined wavelet filter is also possible, subject to satisfying those conditions discussed in previous section. To select the suitable wavelet to be used in decomposition of LO data, a trial of about 15 different wavelets on few light curves has been pursued. It was found that two specific wavelets among them, namely, coiflet 4 and symlet 20 are applicable for filtering.

Application of wavelet on the signal will first decompose it into several

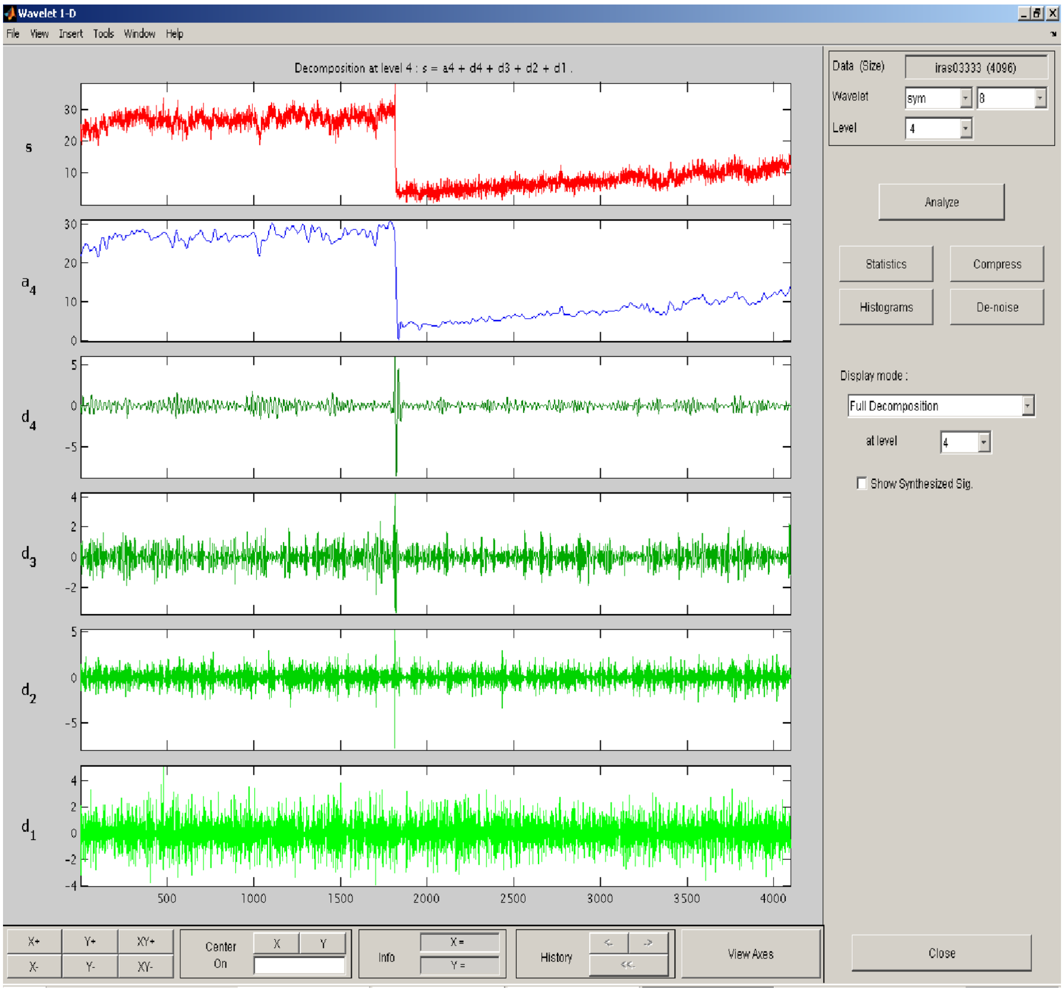

Figure 5.15: The MATLAB wavelet toolbox used in analysis. X-axis shows the number of data points (or time) and Y-axis of each panel shows the relative amplitudes present in the signal. The upper most panel shows the input raw light curve of IRAS 03333+2359 with 4096 (2^{12}) data points. The second panel shows the average coefficients after 4^{th}-level decomposition. The next four panels show the detail coefficients of the decomposition. In MATLAB window the options are available to change the wavelet and level of decomposition. Using the De−noise button one can move to denoising window and set the cut-off for each detail coefficients individually, and then reconstruct the denoised light curve. Two mode of cut-offs are available in MATLAB - (1) Soft-cutoff & (2) Hard-cutoff. In 'Soft-cutoff' a certain amount of amplitude is deducted from all the coefficient, while in the case of 'Hard-cutoff' amplitude above the cutoff value are clipped. Here, 'Soft-cutoff' has mainly been used on all the light curves.

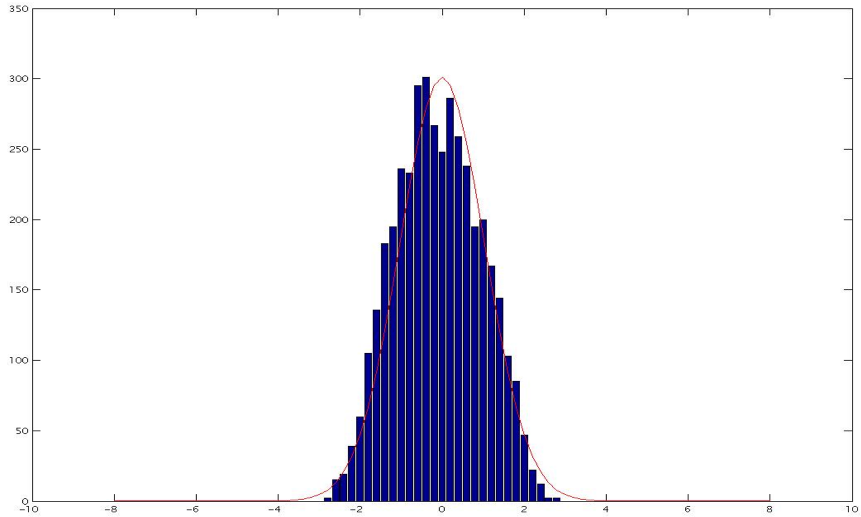

Figure 5.16: Histogram of the removed components from the light curve of IRAS 03333+2359 using the Wavelet transforms. It follows the Normal distribution and hence, the removed components are purely random in nature. A Normal distribution curve is also over-plotted on the histogram for illustration.

details coefficients and one average coefficient subjected to the level of decomposition. After 3^{rd} level decomposition it will produce $cd1$, $cd2$, $cd3$ and $ca3$ where $cd1$ corresponds coefficients of highest frequencies. An example of the wavelet tool window used for analysis is displayed in Fig. 5.15. X-axis represents the time in which data has been acquired, while Y-axis show the amplitudes of the coefficients. It shows a 4^{th} level decomposition of the light curve of the source $IRAS\ 03333 + 2359$ with a wavelet called $symlet8$. The upper most panel shows the raw light curve, while the 2^{nd} panel shows the low-pass (or average) coefficients after decomposition. The next four panels show the details coefficients. The lower most panel corresponds to the highest frequency. Photon noise contributes to the two highest frequency coefficients (or the lowest level detail coefficients in $MATLAB$ window). The contribution from the scintillation creates low frequency variations in the light curve and hence, they will come in the higher level details coefficients.

To remove the high frequency noise from the signal a cut-off limit for each

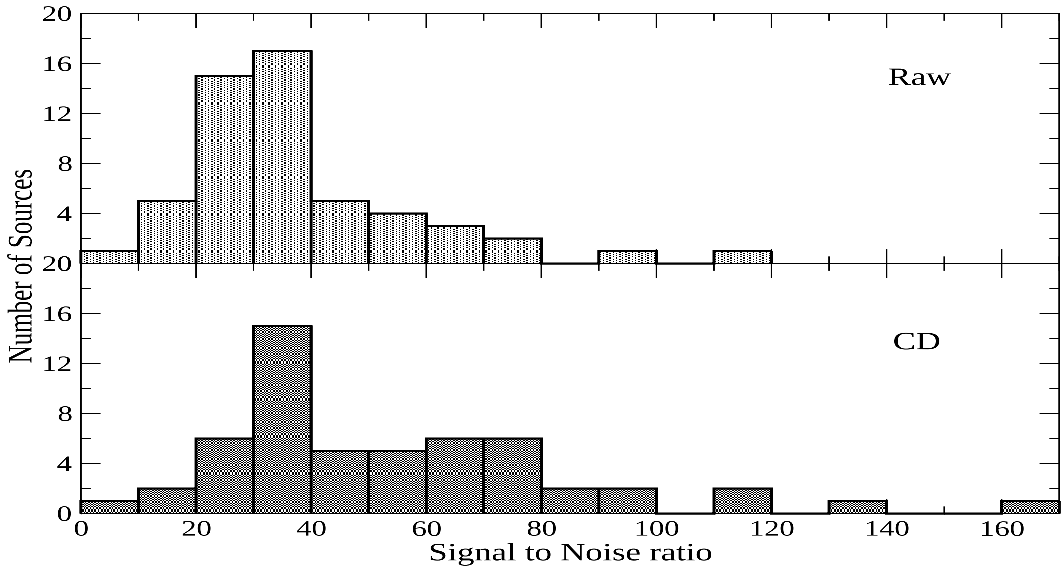

Figure 5.17: The Histogram shows that 14 sources improved to S/N > 40 after the application of Combination method.

components is implemented manually. Two mode of cut-offs are available in MATLAB : (1) Soft-cutoff & (2) Hard-cutoff. In 'Soft-cutoff' a certain amount of amplitude is deducted from all the coefficient, while in the case of 'Hard-cutoff' amplitude above the cutoff value are clipped. Here, 'Soft-cutoff' has mainly been used for noise removal of the light curves. But the removed components should also follow some constraints. In LO light curves mainly the highest frequency coefficients are removed and they are Gaussian noise. Hence, their residuals (raw − denoised) should follow a Gaussian distribution with zero mean (Fig. 5.16).

Wavelet denoising has been applied on all the 54 LO light curves. Though significant improvement was obtained in the S/N using the Wavelet transform method, it is found that purely noise frequencies like 31 Hz, 50 Hz are present with significant power in the wavelet denoised light curves. The wavelet denoising method also has an averaging effect, because it deducts the detail coefficients with a certain cutoff. The reduction of high fluctuation from the average base-level would always lead to a smoothening effect. The effect finally smoothen the observed light curves and hence, in the model they fit to higher

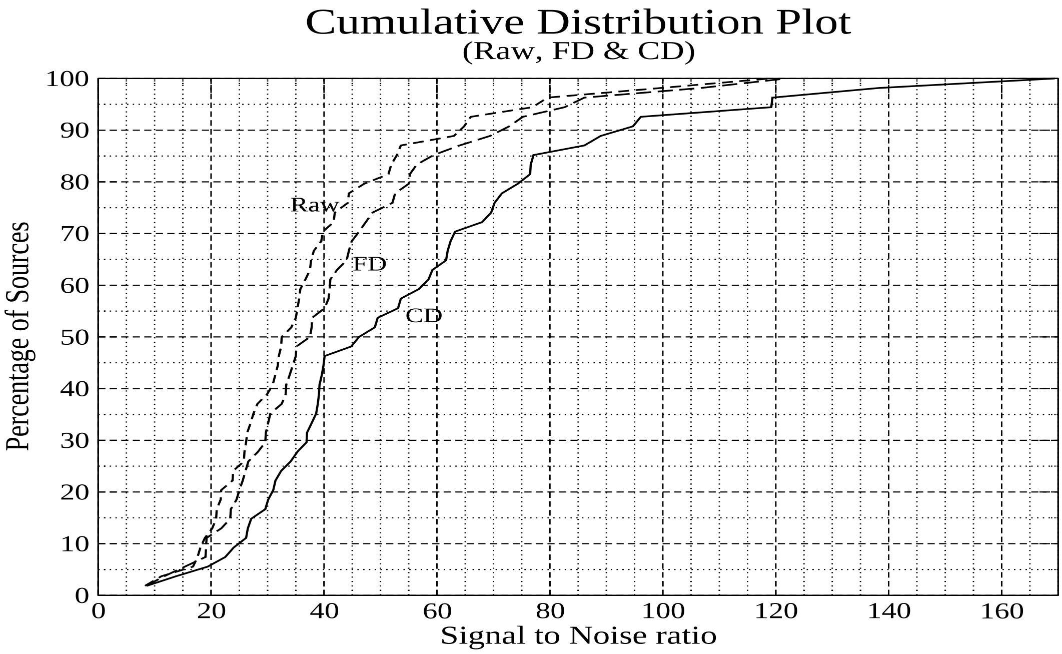

Figure 5.18: The histogram of the number of sources in a specific S/N regime shows that a significant number of light curves moved towards the S/N > 40 after the application of CD method. Number of light curves with S/N > 100 has changed to 9 (lower panel) from 1 (upper panel).

UD values than they actually are.

So, it was decided to use a combination of both the methods. First, FD is carried out to remove those specific noise frequencies. Then WT method is applied in similar manner as explained above. The WT method is executed after the application of FD to put minimum cut-offs on WT coefficients. This is because the averaging effect is cut-off dependent. The deformed fringe pattern fits to absurd UD values. This is also another reason to use the Combination method. The combined denoising (CD) method has been applied on all 54 LO light curves by setting the cut-off limit manually.

5.5 Results & Discussion

The result of the applied methods has two aspects : (1) the improvement in the S/N of the light curves and (2) improvement in the model fits for possible angular diameter determination. We first discuss enhancements in S/N using the two methods, namely, Fourier denoising method (FD) and the combination of Fourier & Wavelet denoising method (CD). Part of the numerical details before and after the application of denoising methods are listed in Table.5.1. The full table is listed in Appendix B. The table here is arranged in the decreasing order of brightness of the sources. The first column of the table lists the source designations and the second column is the apparent K-magnitude as given in 2MASS catalog. The S/N of the observed (raw) and denoised light curves using *Fourier* and *Combination* methods are listed in next three columns of the table.

5.5.1 S/N after FD method

The improvement in the S/N using the FD method is graphically shown in the histogram plot in Fig.5.11. The number of sources with S/N < 40 in the original (raw) sample is 38 and it has reduced to 29 after the application of FD method. It means that 9 sources have improved their S/N beyond 40 after applying the FD method. A different cumulative representation in percentage of the same result is shown in Fig.5.12. Here, the X-axis corresponds to the S/N of the light curves and Y-axis represents the percentage of sources below any specific S/N. For example the dotted line, representing the observed (raw) light curves, shows that 70% of the sources have S/N below 40. It reduces to 55% after the application of FD method (solid line).

The sources which show significant S/N improvement are marked with **bold face** in column 4 of Table.5.1. It can be noticed that a total of 29 out of 54 sources (more than 50%) show significant ($\geq 3\sigma$) improvement in S/N using the FD method. The remaining 25 sources did not show any improvement in their S/N. Out of these 25 sources 14 are brighter than $m_K \sim 3.0$. Noise in these light curves is dominated by low frequency (< 5 Hz) noise. But the main noise components removed in the FD method are 50 Hz, its sub-harmonics (25 Hz & 12.5 Hz) and 31 Hz. The removal of the low frequency noise (mainly due to scintillation) is difficult as it is not at a single frequency but arise upto

5 Hz (see Fig.5.2) with varying power. Complete removal of low frequency component leads to distortion of LO fringes. Hence, S/N of the 14 brighter sources could not be improved by FD method.

Out of the 25 sources 11 are fainter than $m_K \sim 3.0$. It is found that 9 of those 11 sources were observed in the presence of high speed wind ($>$ 40 km/hr) resulting in minute telescope oscillations. One source (SAO 145698) was observed during day time when back-ground scintillation was very high. Another source (SAO 76450) occasionally drifted out of the 10×10 pixels sub-array due to improper telescope tracking at lower elevation. Hence, these 11 fainter sources did not show S/N improvement.

The average enhancement obtained in value of the S/N for 29 sources is 18% after application of FD method. It is also observed that among the 29 sources which show significant S/N improvement, 19 are fainter than $m_K \sim 3$. Infact the largest improvement in S/N using FD method is obtained in the light curve of a faint source SAO 77271 ($m_K \sim 3.3$). The S/N of the source has improved from 32 to 55 (72%). The fainter objects ($m_K > 3.0$) are mainly affected by the sky background photon noise but have a higher noise content at specific frequencies (31 Hz, 50 Hz etc) which is removed by FD method. That is why, they show a good response to the application of the FD method on removing noise at specific frequencies (31 Hz, 50 Hz etc).

5.5.2 S/N after CD method

We now take up S/N improvement obtained using the combination method. It must be noted that in CD method, FD is applied first, followed by the wavelet transform. Wavelet transforms decompose any signal into 'average coefficients' and 'detail coefficients'. It is possible to directly remove fluctuations from the light curve without knowledge of their frequencies by setting suitable cutoffs. That is why it is not surprising that CD method has shown improvement in S/N of all but five of the light curves significantly (except IRC -10564, RT Cap, IRAS 04320+2519[a], IRC +20035 & CW Cnc) and performed better than FD method. The sources IRC -10564 & CW Cnc were observed at lower elevation of 16^o and 18^o respectively. Their light curves are affected by large scintillations and the sources also had occasionally drifted out of 10×10 sub-array. RT cap was observed in the day time and its light curve is affected by large back-ground scintillation. It was partly cloudy during the observation of IRAS 04320+2519[a] and telescope oscillation added uneven noise in the light curve of IRC +20035. Hence, denoising methods did not yield improvement for these sources.

It is mentioned above that in the *Combination* method the wavelet transform is applied after the application FD method on observed light curves. So, the S/N of 29 light curves is already enhanced by average of 18% using FD method before application of wavelet. The histogram plot (Fig.5.17) shows that 38 sources were below S/N ∼40 before application of any denoising method. The number reduced to 29 by FD method (Fig.5.11) which has further reduced to 24 after the application of wavelet method. The cumulative histogram plot in Fig.5.18 (dotted curve) shows that 70% of the sources fall in the region S/N < 40 for observed data (raw). The application of FD method has reduced it to 55% (Fig.5.12). Then the application of wavelet (in CD) method has further reduced it to 45% (solid curve). One source (SAO 77271) has shown significant improvement after applying FD and CD methods. It has shown improvement in S/N from 32 to 55 after application of FD which is further improved to 74 after the application of wavelet transform in CD method.

5.5.3 Model fits to denoised light curves

We next consider the possible improvement in the light curves for better model fits to determine the uniform disk (UD) values (or UD limit on unresolved sources) after the application of FD and CD methods. To examine this aspect, fits to all three (i.e., *Raw*, FD & CD) light curves of all the sources have been carried out. Details of the modeling the LO light curves using the Nonlinear Least Square technique is described in Section.2.6.

After obtaining the best fit to the light curves, the Standard Deviation

(SD) of the residuals (data − model) have been calculated for (a) total data set of 200 points (∼1.8 sec) used in the model fit and (b) fringe portion (40 data points with first fringe of the light curve in the middle). Ideally the values of standard deviation in the fringe portion (SD$_{fringe}$) as well as total data set (SD$_{total}$) should decrease after the application of denoising methods. We expect this to happen because the noise in the observed light curve are reduced by the denoising methods. It was indeed found that the SD$_{fringe}$ and SD$_{total}$ values for denoising light curves are lower than the observed (raw) data in most of the sources (listed in Table.B.1 in Appendix B). However, we have introduced one more parameter called SD$_{ratio}$ ($={}^{SD_{fringe}}/_{SD_{total}}$) to examine the improvement of the model fit in the fringe region relative to the rest of the light curve. SD$_{ratio}$ along with SD$_{fringe}$ and SD$_{total}$ values for all three cases (*Raw*, *FD* & *CD*) are not shown in this chapter but they are listed in columns 6-14 of Table.B.1 of Appendix B. **Lower the value of SD$_{ratio}$ better is the fit to the fringes.**

Table 5.1: Comparison of Raw, FD and CD light curves.

Source	m_K	S/N			Remarks	
		Raw	FD	CD	S/N Improve	Best fits to Fringes
TX Psc	-0.51	63	**73**	**77**	Yes	FD
RS Cap	-0.22	51	53	**59**	No	Raw
CW Cnc	0.11	19	19	19	No	Raw
RT Cap	0.31	38	38	39	No	Raw
SAO 118044	0.49	119	**122**	**138**	Slight	Raw
UZ Ari	1.25	42	42	**46**	No	Raw
IRC +20052	1.25	77	**83**	**95**	Slight	Raw/FD
6 Leo	1.98	54	55	**63**	No	All
SAO 92697	2.03	47	**52**	**62**	Slight	Raw/FD
IRC +20186	2.18	35	35	**39**	No	FD
IRC -10564	2.22	24	26	26	No	All

Table 5.1 – continued from previous page

Source	m_K	S/N			Remarks	
		Raw	FD	CD	S/N Improve	Best fits to Fringes
SAO 92755	2.50	28	30	**31**	No	Raw
IRC +10210	2.50	38	**44**	**57**	Slight	Raw/FD
IRC +00202	2.59	53	**56**	**77**	No	Raw
IRC +20066	2.60	65	**75**	**119**	Yes	Raw/FD
CW Oph	2.65	27	**33**	**39**	Slight	Raw
IRC +30140	2.70	100	**107**	**169**	Slight	Raw/FD
IRC +20037	2.90	34	35	**40**	No	Raw/FD
NSV 1406	2.93	26	26	**30**	No	FD
SAO 77792	2.97	40	**45**	**62**	Slight	All
SAO 76450	3.06	21	22	**27**	No	Raw/FD
BI Gem	3.17	52	**64**	**89**	Slight	FD
SAO 76350	3.20	66	**69**	**96**	Slight	FD
SAO 145992	3.22	80	**86**	**119**	Slight	Raw/FD
SAO 157613	3.24	36	**44**	**72**	Yes	Raw
SAO 77271	3.27	32	**55**	**74**	Yes	FD
SAO 75669	3.35	26	**30**	**45**	Slight	FD
C* 3246	3.58	44	**59**	**86**	Yes	FD
IRAS 06395+2409	3.66	42	**49**	**77**	Slight	FD
AU Ari	3.68	24	25	**34**	No	Raw
UY Ari	3.69	37	**41**	**70**	Slight	All
SAO 75706	3.71	18	19	**23**	No	Raw
SAO 109252	3.74	31	**35**	**53**	Slight	FD
IRAS 05212+2655	3.74	26	28	**31**	No	Raw/FD
SAO 145698	3.80	36	38	**59**	No	Raw/FD
V1134 Tau	3.84	40	40	**54**	No	Raw
SAO 77229	3.87	32	**38**	**49**	Slight	Raw
IRAS 05232+2400	3.94	33	34	**40**	No	Raw/FD

Table 5.1 – continued from previous page

Source	m_K	S/N			Remarks	
		Raw	FD	CD	S/N Improve	Best fits to Fringes
BD+26 1131	4.06	38	**46**	**68**	Yes	FD
IRAS 05013+2704	4.12	35	**41**	**62**	Slight	Raw
SAO 77474	4.14	22	**25**	**35**	Slight	Raw/FD
IRAS 05551+2305	4.18	44	**47**	**70**	Slight	FD
IRAS 04320+2519	4.30	18	19	**24**	No	R/FD
IRAS 04320+2519	4.30	11	12	**14**	No	R/FD
SAO 77357	4.39	22	27	**40**	Slight	FD
SAO 76965	4.40	28	**31**	**39**	Slight	FD
HD 249571	4.50	26	**31**	**37**	Slight	FD
SAO 76952	4.70	17	19	**27**	Slight	FD
IRAS 06165+2431	4.87	20	**23**	**30**	Slight	Raw/FD
IRAS 03333+2359	5.07	21	**24**	**32**	Slight	FD

Out of the original sample of 54 sources considered for S/N improvement, only 50 are accounted for model fits. The remaining four sources though bright (m_K <3.0), could not be fitted to a model curve due to the following reasons. The light curve of SAO 92755 (Observed on January 23, 2010) is too noisy (due to telescope tracking problems) to fit. The light curves of TU Gem and VV Cnc suffer from fringe distortions possibly because of variable rate of lunar component velocity due to limb irregularities. The light curve of IRC +20177 was observed in 20×20 pixels sub-array to accommodate its visual binary component. Sampling time in 20×20 pixels sub-array is poorer than 10×10. Its poor sampling time of ∼14 msec, provided a few data points on the fringes and could not be fitted properly. However its binary separation of 700±50 mas is obtained.

5.5.4 Improvement in model fits

When we examine the Table.B.1, in most of the cases the SD_{ratio} for CD is higher than SD_{ratio} for original (raw) and FD light curves. It shows that CD light curves fit poorly to model compared to FD or *Raw* light curves. This result arises because the S/N enhancement seen in CD method is mainly due to better denoising effect in the non-fringe region compared to the fringe region. CD method results in a slight smoothening of the light curves in general and leads to a higher UD value in the model fit. Only in the case of a well resolved source (TX Psc), SD_{ratio} value for CD is lower than other two. This results are also illustrated in Fig.5.19. In the figure, SD_{ratio} values of all three methods are plotted arranging the SD_{ratio} values for *Raw* data in ascending order. It can be seen that while the SD_{ratio} values for FD method is fluctuating with respect to the *Raw* values, they generally show higher values for CD than other two methods.

Out of the 50 sources selected for the model fits about one third (17) have lower SD_{ratio} value for the observed (raw) light curve than that for FD or CD. For half of the sources (24) the SD_{ratio} is not significantly different between raw and FD but they are lower than CD (Fig.5.19). For the remaining 8 sources; namely, BD+26 1131, C* 3246, IRAS 06395+2409, SAO 109252, SAO 75669, HD 249571, NSV 1406 & IRAS 05551+2305, SD_{ratio} value for FD is significantly lower than both *Raw* and CD data. Out of the 8 sources, 6 have shown earlier significant S/N improvement on applying the FD method. Those sources are marked in the Fig.5.19 along with their S/N improvement in percentage. These sources are all fainter than $m_K \sim$3.3.

5.5.5 Resolved and unresolved sources in the sample

Out of 50 sources, we find on analysis that, five are clearly resolved. Our values agree well with the earlier reported UD angular diameters. They are listed in Table.5.2 along with the references of the earlier reports in the last column. These sources are bright and, except $TX\ Psc$, the observed (raw)

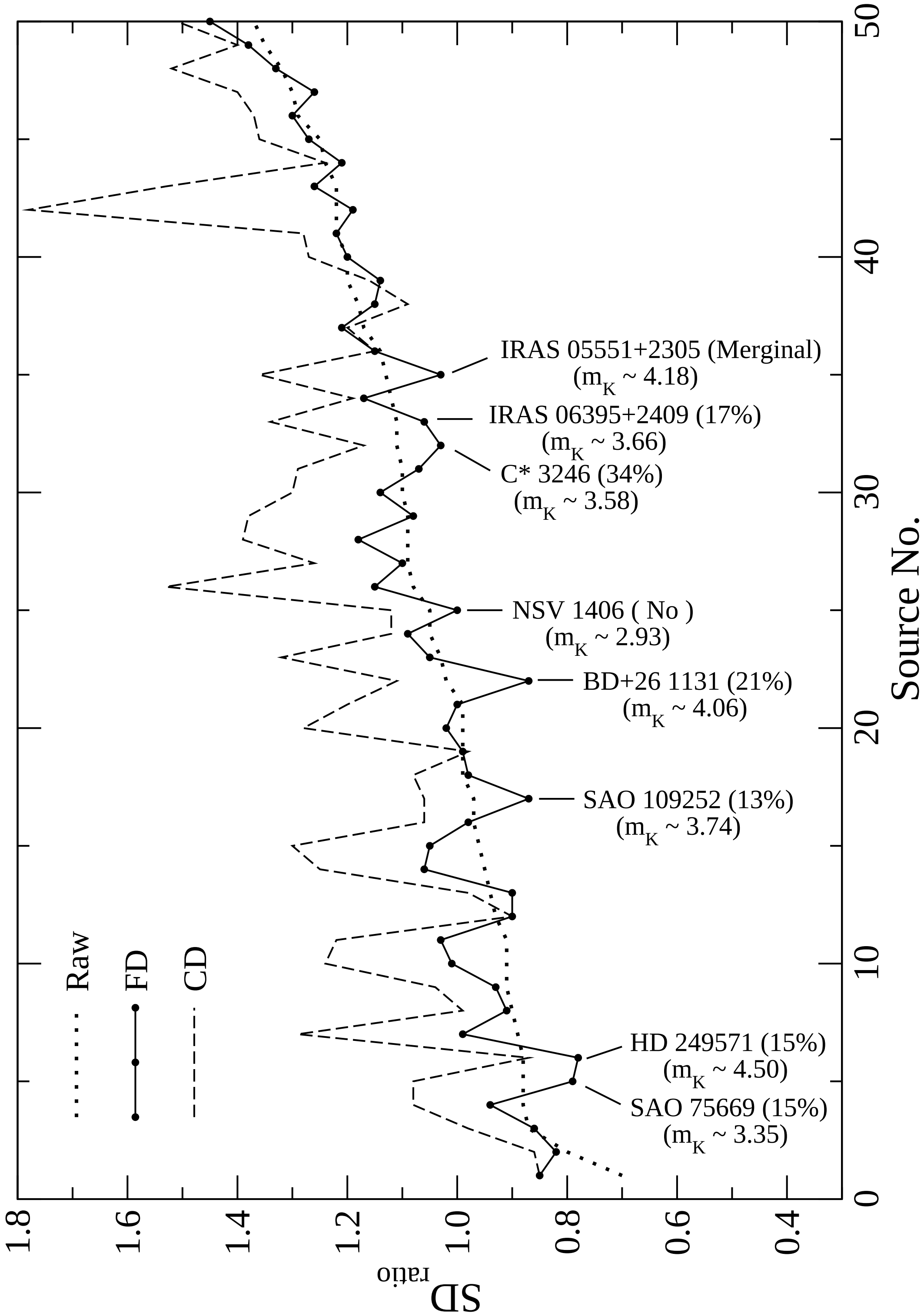

Figure 5.19: SD_{ratio} of Raw, FD and CD light curves are plotted with SD_{ratio} of observed (raw) data arranged in ascending order. The SD_{ratio} values of CD methods are generally higher (poorer fit to the light curve) than the other two. SD_{ratio} for FD fluctuates with respect to the Raw values. The sources which show lowest SD_{ratio} values for FD method (best fit to the light curves) are marked along with their S/N enhancement (in percentage) obtained using FD method.

data provides the best fit. For $TX\ Psc$, CD data fits best.

A close examination of our model fits and details of sources in the literature reveals that two more sources are expected to be resolved. There are two LO observations of $UZ\ Ari$ (IRC +20052). One light curve (observed on November 30, 2009) shows improvement after the application of FD method but both show improvement in S/N after CD method. However, no improvement has been obtained in their fits. This object is a semi-regular variable with a period of 163 days. Fits to them provide comparable UD values of 5.5±0.5 mas and 6.0±0.5 mas respectively. According to the angular diameter prediction method discussed in Baug & Chandrasekhar (2012; Also discussed in Chapter 4 of this thesis) expected UD value for this source is 4.2±1.0 which is a little lower than the measured values. The source SAO 92697 is also a semi-regular variable with period of 206 days. A close examination of the model fit reveals that the source is expected to be resolved. The FD data fits slightly better than the observed (*Raw*) light curve giving the UD angular diameter of 4.7±0.5 mas. These sources are also listed in Table.5.2.

The light curve and model fits of the remaining sources have been carefully examined to see if any of these sources is resolved. We find all these sources to be unresolved (Table.5.3). But the limit of resolution varies from source to source depending on the S/N and other conditions. The faintest source $IRAS$ $03333 + 2359$ ($m_K = 5.1$) has a S/N∼25, is best fitted with FD light curve giving a limit $< 4.3 \pm 1.2$ mas. The lowest limit to the resolution of $< 3.5 \pm 0.5$ mas is obtained for UY Ari ($m_K = 3.7$). A good S/N improvement is obtained by applying the denoising methods on this source and all three light curves fits to UD limits. For most of the sources with good light curves, we obtained a resolution limit close to < 4.0 mas.

For bright sources the *Raw* data appears to be the best for model fits. For fainter objects ($m_K > 3.3$) where back-ground noise dominates, it appears that the better fit is obtained with FD light curves in which noise at specific frequencies are filtered out. In case of CD though there is substantial S/N improvement in most of the cases, there is a smoothening of the light curves.

This leads to a larger limit to the fitted UD values compared to FD and Raw data. In case of well resolved sources like TX Psc where fit is less affected from smoothening effect, CD also provides a good fit.

Table 5.3: Uniform disk angular diameter limits for unresolved sources.

Source	UD (mas)	Best fit light curve
IRAS 03333+2359	<4.3±1.2	FD
IRC +20186	<4.0±0.5	FD
SAO 76965	<4.6±0.8	FD
BD+26 1131	<4.0±0.5	FD
SAO 77271	<4.8±0.5	FD
SAO 76350	<3.6±0.3	FD
C* 3246	<3.9±0.5	FD
BI Gem	<4.2±0.6	FD
SAO 77357	<4.0±0.5	FD
IRAS 06395+2409	<4.4±0.6	FD
SAO 109252	<4.7±0.6	FD
SAO 75669	<4.0±0.5	FD
NSV 1406	<4.0±0.5	FD
SAO 76952	<4.0±0.5	FD
HD 249571	<4.0±0.5	FD
IRAS 05551+2305	<4.0±0.5	FD
SAO 145992	<4.6±0.5	R/FD
IRAS 05212+2655	<4.5±0.5	R/FD
SAO 77229	<3.8±0.5	R/FD
IRC +30140	<4.0±0.4	R/FD
IRAS 04320+2519	<6.0±1.0	R/FD
IRC +20037	<4.0±0.5	R/FD
SAO 76450	<6.0±1.0	R/FD
IRAS 04320+2519	<5.0±1.0	R/FD

Table 5.3 – continued from previous page

Source	UD (mas)	Best fit light curve
SAO 77474	<5.5±1.5	R/FD
IRC +10210	<4.0±0.5	R/FD
SAO 145698	<4.0±0.5	R/FD
IRC +20066	<4.0±0.5	R/FD
IRAS 05232+2400	<4.0±0.5	R/FD
IRC -10564	<4.0±0.5	All
UY Ari	<3.5±0.5	All
SAO 77792	<4.0±0.5	All
6 Leo	<4.0±0.5	All
V1134 Tau	<4.5±1.0	R
IRAS 05013+2704	<4.0±0.6	R
SAO 157613	<4.0±0.5	R
IRC +00202	<4.8±0.5	R
SAO 92755	<4.0±1.0	R
IRAS 06165+2431	<5.9±1.2	R
AU Ari	<5.4±1.1	R
SAO 75706	<4.0±0.5	R
CW Oph	<4.0±1.0	R

5.6 Conclusions

Noise reduction method in LO light curves using Fourier, Wavelet transforms and their combination is discussed in this chapter. A total of 54 light curves have been chosen as the sample. We found -

1. S/N enhancement occurs in both Fourier and combination methods .

2. The FD denoised light curves which have significant S/N improvement, show best model fit in a few cases. Further the FD method performs better

Table 5.2: Resolved sources in the sample (UD values).

Source	Filter (μm)	UD Ang. Dia. (mas)	Earlier Reported UD (mas)	Reference
RT Cap	2.20/0.40	8.1±0.3	7.72±0.16	WF 1987
			8.18±0.21	VT&PTI 2000
RS Cap	2.37/0.10	7.7±0.5	7.75±0.67	RDLC 1992
			7.70±0.80	DVT 1998
CW Cnc	2.20/0.40	7.0±0.5	7.05±0.33	WF 1987
SAO 118044	2.20/0.40	4.9±0.5	4.85±0.23	WF 1987
TX Psc	2.37/0.10	10.6±0.5	7.50±0.50	RCL 1995
			7.72±0.06	RCL 1995
			9.50±0.83	VT 1999
			9.82±0.10	RCL 1995
			11.20±0.30	DVB 1996
			11.24±0.05	Charm2 (A.R. unp)
			11.44±0.31	VT 1999
			11.45±1.04	VT 1999
Resolved (No earlier reports)				
UZ Ari (2009)	2.20/0.40	5.5±0.5	–	–
UZ Ari (2010)	2.20/0.40	6.0±0.5	–	–
SAO 92697	2.20/0.40	4.7±0.5	–	–

in the fainter regime ($m_K \geq$3.3).

3. *CD* method definitely improves S/N on all light curves but due to its smoothening effect, it provides a higher UD value for diameter fits. It appears to be more suitable for fitting well resolved sources like TX Psc.

4. Five sources in our sample are clearly resolved. The fitted angular diameters are in good agreement with earlier measurements. From our analysis on light curves, we expect two more sources to be resolved (Table.5.2). One of these sources (UZ Ari) has been observed twice. There are no earlier reports of angular resolution on these sources.

The rest of the sources in our sample are unresolved. Most of them are expected to have UD values <4 mas (Table.5.3).

Chapter 6

Summary and Outlook

6.1 Summary

The aims of this thesis are -

(1) To study late type giants at high angular resolution using the lunar occultation technique in the near infrared.

(2) To study sources towards the highly obscured Galactic centre region at high angular resolution.

(3) Compared to the single element fast photometer used earlier, it is possible to go fainter by ∼2 magnitudes in K-band using the NICMOS sub-array. But S/N remains a problem, hence the motivation to develop a noise reduction method of the observed lunar occultation (LO) light curves in this thesis.

A concerted effort has been made to achieve the goals mentioned above. A total of 69 LO light curves are reported and analysed in this thesis. Among them 13 are clearly resolved. The resolved sources include - two oxygen-rich Mira variables, four oxygen-rich and one carbon-rich semi-regular variables, and two carbon stars. Three of the resolved sources are located in the direction of the highly obscured Galactic centre region. The upper limits for uniform disk (UD) angular diameters have been derived for the remaining 56 unresolved sources. The reported upper limits are variable ranging from 3 to 8 milliarcseconds (mas) depending on the signal to noise ratio of the observed light curves.

Prior to this thesis the recording of the lunar occultation events at Mt. Abu observatory were carried out using a single element fast photometer sensitive to $m_K \leq$3.0. Hence, the Two Micron Sky Survey (TMSS) catalog ($m_K \leq$3.5) was used as the input catalog for the prediction of LO events. To explore the angular diameters in the fainter regime upto $m_K \sim$5.0, an Area of Interest (AOI) sub-array was made operational in the NICMOS IR-camera and used for observations in this thesis. The experiments carried out for optimum sub-array size and integration time reveal that the 10×10 pixels ($5'' \times 5''$ on the sky) sub-array is best suited to record the LO events using the 1.2m telescope at Mt. Abu in the present conditions. As the fainter regime of stars is being explored with NICMOS sub-array, modification in the LO event prediction script has been made. A subset of 2-Micron All Sky Survey (2MASS) catalog with $m_K \leq$6.0 and declination limit of -30^o to +30^o is included as input catalog for prediction of LO events. Using this sub-array sources upto $m_K \sim$5.0 have been successfully recorded with a signal to noise ratio of about 20.

The second goal of studying the rare LO events towards the Galactic centre became possible only because of the fainter detection limit of the NICMOS sub-array. All the the sources observed in that direction are fainter than the detection limit of the fast photometer ($m_K \sim$3.5). We clearly resolved three late type giants towards the Galactic Centre at high angular resolution. Their huge resolved angular sizes imply the presence of extended circumstellar emission. But we could not separate stellar and circumstellar extent because of the limited S/N of the observed LO light curves.

A prediction method for the uniform disk values of oxygen-rich Mira and Semi-regular variables (SRVs) is developed in this thesis through a calibration procedure using previously measured angular diameters of several AGB variables available in CHARM2 catalog. It only needs the (V−K) colour for prediction of UD angular diameter value of o-rich Mira and SRVs. However, it may have upto 25% error in the calculated value because of the unavailability of the contemporaneous photometry of the sources used in the calibration. The predicted uniform disk values show good agreement with the UD angular diameters measured by us. In addition in this thesis we have examined the effect of mass-loss or presence of thick circumstellar shell on the measured uniform disk angular diameter of Mira variables. It is found that one of the Mira variables, BS Aur, has a substantial enhancement ($\sim$40%) in its uniform disk angular diameter due to mass-loss/circumstellar shell.

Two noise reduction techniques based on Fourier and Wavelet transforms have been implemented to improve the S/N of the observed light curves. Both the methods, particularly the Wavelet transform, are found to be effective in terms of the S/N improvement of the light curves. A combination of Fourier and Wavelet transforms has also been studied. But the intrinsic smoothening effect of Wavelet transforms leads to fit higher uniform disk values in the modeling of the light curves. So, effectively the noise reduction of LO light curves with the help of Wavelet transforms turns out to be inefficient. An improvement in the S/N as well as better model fits of the Fourier denoised light curves is found to occur in the fainter regime ($m_K \geq$3.3).

6.2 Outlook

The method of lunar occultations continues as a useful one dimensional high angular resolution (HAR) technique at 1-m class telescopes in the era of modern optical/IR long baseline interferometers. There are tens of thousands stars present in the solar neighbourhood as discussed in Section.1.1, but only a few thousand stars have angular diameter measurements. The Catalog for High Angular Resolution Measurements (CHARM2; Richichi et al., 2005) lists 502 lunar occultation angular diameter values and K & M-giants are the most favoured targets in HAR studies, using LO.

Generally late type giants show enhanced angular diameters in the longer wavelengths as discussed in Section.4.1. Considerable effort was made earlier by the group at PRL for multi-band (NIR K-band (2.2μm) & narrow L'-band (3.6μm)) LO observations simultaneously. Simultaneous K- & L-bands LO observations can help to unravel stellar and circumstellar contributions.

The two channel photometer has not been exploited fully. Only a few sources have multi-band lunar occultation observations. L'-band LO observations are challenging to make but can be scientifically rewarding.

Recent spectro-interferometric study on AGB stars have resulted in new findings like - (1) Correlation between presence of amorphous silicates in the circumstellar shell of oxygen rich AGB and shell thickness (Waters & Leinert, 2008), (2) Variability in the angular diameters values within NIR K-band (Wittkowski et al., 2011). Multi-spectral lunar occultations in the infrared can also probe the atmosphere of these stars. A study of a carbon star at the wavelength region 1-4 μm using multi-spectral lunar occultation has been reported (Harvey & Oldag, 2007). More sources need to be explored in detail using multi-spectral LO methods. The earlier instrument (fast IR-photometer) with a single element detector would not be suitable for spectral mode occultations even with 1m telescope. But specially configured linear array detectors can help in observing bright objects in multi-spectral mode.

Though late-type giants cover major part of the angular resolution measurements till date, the HAR studies at different variability epochs are relatively few. The AGB variables like Mira experience high stellar pulsation and the size and spectral types also change accordingly. The region where the mass outflows are initiated is unknown. The availability of angular diameters at different photometric phases of these AGB variables can help to probe interesting questions related to their pulsation modes as well as mass-loss mechanism. Multi-spectral lunar occultation can answer many questions related to the circumstellar matter of late type giants and other dust enshrouded stars like Wolf-Rayet stars. Asymmetries are common phenomena in Mira variables due to heavy mass-loss. Multiple Lunar occultation observations of same source at different position angles can help to determine the asymmetry to an extent. LO has the potential to perform these studies using moderate sized 1-2m class telescopes and can complement results derived from highly sophisticated optical long baseline interferometers.

Appendix A

NICMOS sub-array script

The NICMOS 10×10 pixels Area of Interest (AOI) sub-array script written in *C*-language is developed for observing lunar occultation events.

```
int aoi_fixed_10X10(void)
{
  int framecount =0, recivedframe=0,  temp, *val;
  int smin=25000, smax=38000,   k1=0, k2=0, row, col, delay1=30;
  char cc='!', answer, cbuf[60];
  int dis_delay =100;

_settextposition(26,1);
 sprintf(cbuf,"AOI  10X10  selected Please enter parameter ..    ");
 _outtext(cbuf);
 _settextposition(27,1);
 sprintf(cbuf,"                                                    ");
 _outtext(cbuf);
 _settextposition(28,1);
 sprintf(cbuf,"                                                    ");
 _outtext(cbuf);
 _settextposition(29,1);
 sprintf(cbuf,"                                                    ");
 _outtext(cbuf);
```

```
 serial_out(SYS_PORT,"I0 1 100");
 serial_out(SYS_PORT,"I1 1 100");
 serial_out(SYS_PORT, "CT 1");
 serial_out(SYS_PORT, "CR 0");
 serial_out(SYS_PORT, "RUN");
 delay(500);
 serial_out(SYS_PORT, "STOP");

serial_out(SYS_PORT,"I1 1 3");
serial_out(SYS_PORT,"I0 1 3");
serial_out(SYS_PORT,"CT 7");
serial_out(SYS_PORT,"CR 0");
serial_out(SYS_PORT,concatethree("AOIPOS ",px,py));
serial_out(SYS_PORT,"AOIDIM 10 10");
serial_out(SYS_PORT,"AOIBLD");

  i0time =3;
  i1time =3;
  xxx=10;
  yyy=10;
   _settextposition(26,1);
   sprintf(cbuf,"AOI build given to camera approx wait %d ",delay1);
   _outtext(cbuf);
   _settextposition(27,1);
   sprintf(cbuf,"AOI,10x10 3+3+4msec'0'stop aq. f. & Max4800 F no display");
   _outtext(cbuf);
   _settextposition(28,1);
   sprintf(cbuf,"I0=3 I1=3 px=%d py=%d F1=%1d F2=%1d",px,py,filter1,filter2);
   _outtext(cbuf);
```

```
  for(i=0;i<delay1;  i++)
  {
delay(980);
   _settextposition(26,1);
   sprintf(cbuf,"AOI BUILD COMMAND TO ARRAY Wait  %d ",(delay1-i));
   _outtext(cbuf);  }
   _settextposition(26,1);
   sprintf(cbuf,"AOI BUILD ARRAY DONE & Data acquisition  is ready ");
   _outtext(cbuf);
   _settextposition(27,1);
   sprintf(cbuf,"Do you want (n/N for stop) RUN (y/Y any key )?:  ");
   _outtext(cbuf);
answer ='W';

 do{
   if (kbhit()) { answer=getch();}
   display_time();
   read_telescope_status();
   strip_fields();
   } while (answer =='W');
   if(answer=='n' || answer=='N')
   {
    return(PASSED);
 }
   _settextposition(27,1);
   sprintf(cbuf,"                                   ");
   _outtext(cbuf);
   _settextposition(26,1);
   sprintf(cbuf," Aq. frame no. =%6d     ",framecount);
   _outtext(cbuf);
   display_time();
```

```
serial_out(SYS_PORT,"RUN");


       while((cc!=48) && (framecount < 4800))
              {
               do_dma((656 * BYTES_PER_PIX),dma_array1);


               for(i=259; i< 656; i+=4)
               {temp = *(dma_array1+i);
               *(bufo+k1) = temp;
               k1++;         }
               if (kbhit()) {cc=getch();}
               framecount++;
               _settextposition(26,17);
               sprintf(cbuf,"%6d  ",framecount);
               _outtext(cbuf);
               delay(1);
               }
recivedframe =framecount;
display_time_stop();
serial_out(SYS_PORT,"STOP");
i0time =0.10;
i1time =0.10;
serial_out(SYS_PORT,"I0 1 100");
serial_out(SYS_PORT,"I1 1 100");
serial_out(SYS_PORT, "CT 1");
serial_out(SYS_PORT, "CR 0");
serial_out(SYS_PORT, "RUN");
delay(10);


_settextposition(26,1);
_outtext("Writing to the Disk in single file .......        ");
```

```
   _settextposition(27,1);
   sprintf(cbuf,"                                                    ");
   _outtext(cbuf);
   _settextposition(29,1);
   sprintf(cbuf,"AOI 20x20 aq. frames recived = %d  ",recivedframe);
   _outtext(cbuf);
   repeat = framecount;

                  if((increment_file(AOIFIX)) == PASSED )
                     {  fwrite(bufo,(framecount * 400),1,single);
                        }
                 else
                  {
                      user_int("Some Files not Saved,Exiting Routine.");
                      return(FILE_OPENING_ERROR);
                  }

 _settextposition(26,1);
 _outtext("Display data on monitor & small file save");
 display_time;
 k1=0;

framecount =0;
cc ='!';

  for(col=1;col<520 && (cc!=48 && (framecount <recivedframe )) ;)
  {
     for(row=1; row<380 && (cc!=48 && (framecount<recivedframe));)
     {
            if (smax== smin)  {smax=smax+100;};
            k2=k1;
```

```
            for(j=0;  j<100; j++)
{
temp = *(bufo+k1);
*(buf2+j) = temp;
k1++;
if(temp < smin)
*(gbuf+j)=0;
else if(temp > smax)
*(gbuf+j) = 255;
else
*(gbuf+j)=((temp-smin)*255/(smax-smin));
}
framecount++;
rap_dosvid_write(row,col,10,10,(PCBFVOID)gbuf,0);
row= row + 20 +10;
if (dis_delay < 1)   dis_delay = 1;
if (dis_delay > 500) dis_delay = 500;
delay(dis_delay);

    _settextposition(27,1);
    sprintf(cbuf,"Display delay  A+ B-  %6d       ",dis_delay);
    _outtext(cbuf);
    _settextposition(28,1);
    sprintf(cbuf,"Smin=%6d Smax=%6d Save frame-no=%6d",smin,smax,framecount);
    _outtext(cbuf);

     if (kbhit())
{
if ((cc=getch()) == '0')
{
return(PASSED);
```

```
};
if (cc == 'l') { val = &smin; };
if (cc == 'L') { val = &smin; };
if (cc == 'u') { val = &smax; };
if (cc == 'U') { val = &smax; };
if (cc == 55) { *val += 10;    };
if (cc == 49) { *val -= 10;    };
if (cc == 56) { *val += 100;   };
if (cc == 50) { *val -= 100;   };
if (cc == 57) { *val += 1000;  };
if (cc == 51) { *val -= 1000;  };
if (cc == 54) { *val += 10000; };
if (cc == 52) { *val -= 10000; };
if (cc == 'A' || cc=='a') { dis_delay += 10;};
if (cc == 'B' || cc=='b') { dis_delay -= 10;};
}
if(increment_file(SINGLE)==PASSED)
fwrite(buf2,(400),1,single);
else
{
user_int("Some Files not Saved, Exiting Routine.");
return(FILE_OPENING_ERROR);
}
}
    col=col+ 20 +10;
    if(col>=521) col=1;
   }
   _settextposition(26,1);
   _outtext("Data Acquisition & display/storage Over & array reset ");
   _settextposition(27,1);
   _outtext("                                                      ");
```

```
    _settextposition(28,1);
    _outtext("                                                          ");
    getch();
    serial_out(SYS_PORT, "CT 1");
    serial_out(SYS_PORT, "CR 0");
    serial_out(SYS_PORT, "RUN");
    delay(10);
    return(PASSED);
}
```

Appendix B

Statistical details before and after Denoising methods

The full details after the denoising methods is listed as a table for 54 sources. The part of this table is listed in Table.5.1. The columns in this table are listed in the following manner. Column 1: Source designation, Column 2: K-magnitude of the source as given in the 2MASS catalog, Column 3 to 5: the Signal to noise ratio of observed (*Raw*), FD and CD light curves, Column 6 to 8: SD_{fringe} values (see Chapter 5 for details) for *Raw*, FD and CD light curves, Column 9 to 11: SD_{total} values for for *Raw*, FD and CD light curves, Column 12 to 14: SD_{ratio} for *Raw*, FD and CD light curves, Column 15: whether the S/N improvement is seen or not, and Column 16: the best model fit obtained among *Raw*, FD and CD light curves.

Table B.1: Comparison of Raw, FD and CD light curves.

Source	m_K	S/N			SD_{fringe}			SD_{total}			SD_{ratio}			Remarks	
		Raw	FD	CD	Raw	FD	CD	Raw	FD	CD	Raw	FD	CD	S/N Improve	Best fits to Fringes
TX Psc	-0.51	63	**73**	**77**	1.53	1.19	0.90	1.29	1.03	0.83	1.18	1.15	1.09	Yes	FD
RS Cap	-0.22	51	53	**59**	4.25	3.96	3.86	3.55	3.48	3.33	1.20	1.14	1.16	No	Raw
CW Cnc	0.11	19	19	19	7.43	8.08	7.92	5.49	5.86	5.67	1.35	1.38	1.40	No	Raw
RT Cap	0.31	38	38	39	11.16	11.27	10.87	9.76	9.79	9.47	1.14	1.15	1.15	No	Raw
SAO 118044	0.49	119	**122**	**138**	2.48	2.44	2.37	2.07	2.03	1.87	1.20	1.20	1.27	Slight	Raw
UZ Ari	1.25	42	42	**46**	6.67	7.08	6.83	4.88	4.88	4.52	1.37	1.45	1.51	No	Raw
IRC +20052	1.25	77	**83**	**95**	2.22	2.09	1.92	1.80	1.73	1.56	1.24	1.21	1.24	Slight	Raw/FD
6 Leo	1.98	54	55	**63**	5.31	5.34	5.24	4.16	4.10	3.83	1.29	1.30	1.37	No	All
SAO 92697	2.03	47	**52**	**62**	0.92	0.81	0.71	1.02	0.89	0.71	0.90	0.91	0.99	Slight	Raw/FD
IRC +20186	2.18	35	35	**39**	4.76	4.69	5.06	3.68	3.71	3.61	1.30	1.26	1.40	No	FD
IRC -10564	2.22	24	26	26	2.78	2.77	2.72	2.81	2.79	2.76	0.99	0.99	0.98	No	All
SAO 92755	2.50	28	30	**31**	1.25	1.51	1.43	1.80	1.78	1.68	0.70	0.85	0.85	No	Raw
IRC +10210	2.50	38	**44**	**57**	1.12	1.08	1.00	1.03	0.91	0.72	1.09	1.18	1.39	Slight	Raw/FD

Table B.1 – continued from previous page

Source	m_K	S/N			SD_{fringe}			SD_{total}			SD_{ratio}			Remarks	
		Raw	FD	CD	Raw	FD	CD	Raw	FD	CD	Raw	FD	CD	S/N Improve	Best fits to Fringes
IRC +00202	2.59	53	**56**	**77**	0.87	0.82	0.64	0.78	0.70	0.54	1.12	1.17	1.19	No	Raw
IRC +20066	2.60	65	**75**	**119**	1.05	1.01	1.05	0.98	0.88	0.68	1.08	1.15	1.53	Yes	Raw/FD
CW Oph	2.65	27	**33**	**39**	1.44	1.16	0.98	1.54	1.29	1.10	0.93	0.90	0.90	Slight	Raw
IRC +30140	2.70	100	**107**	**169**	1.07	0.91	0.94	0.87	0.77	0.53	1.22	1.19	1.78	Slight	Raw/FD
IRC +20037	2.90	34	35	**40**	1.52	1.51	1.38	1.89	1.84	1.61	0.80	0.82	0.86	No	Raw/FD
NSV 1406	2.93	26	26	**30**	1.22	1.08	1.00	1.16	1.08	0.89	1.05	1.00	1.12	No	FD
SAO 77792	2.97	40	**45**	**62**	1.36	1.22	1.11	1.03	0.92	0.73	1.32	1.33	1.52	Slight	All
SAO 76450	3.06	21	22	**27**	1.16	1.16	1.08	1.06	1.02	0.83	1.10	1.14	1.30	No	Raw/FD
BI Gem	3.17	52	**64**	**89**	0.74	0.66	0.62	0.81	0.65	0.50	0.91	1.01	1.24	Slight	FD
SAO 76350	3.20	66	**69**	**96**	0.90	0.86	0.87	0.91	0.84	0.68	0.99	1.02	1.28	Slight	FD
SAO 145992	3.22	80	**86**	**119**	0.87	0.85	0.77	0.96	0.91	0.75	0.91	0.93	1.04	Slight	Raw/FD
SAO 157613	3.24	36	**44**	**72**	0.67	0.65	0.67	0.75	0.66	0.52	0.89	0.99	1.29	Yes	Raw
SAO 77271	3.27	32	**55**	**74**	1.35	0.90	0.86	1.42	0.85	0.68	0.95	1.06	1.25	Yes	FD
SAO 75669	3.35	26	**30**	**45**	0.83	0.65	0.56	0.94	0.83	0.52	0.88	0.79	1.08	Slight	FD

Table B.1 – continued from previous page

Source	m_K	S/N			SD_{fringe}			SD_{total}			SD_{ratio}			Remarks	
		Raw	FD	CD	Raw	FD	CD	Raw	FD	CD	Raw	FD	CD	S/N Improve	Best fits to Fringes
C* 3246	3.58	44	**59**	**86**	0.87	0.67	0.55	0.78	0.65	0.47	1.11	1.03	1.17	Yes	FD
IRAS 06395+2409	3.66	42	**49**	**77**	0.86	0.73	0.60	0.78	0.68	0.46	1.10	1.07	1.29	Slight	FD
AU Ari	3.68	24	25	**34**	0.97	0.89	0.83	0.89	0.83	0.60	1.09	1.08	1.38	No	Raw
UY Ari	3.69	37	**41**	**70**	0.90	0.84	0.68	0.74	0.67	0.45	1.22	1.26	1.53	Slight	All
SAO 75706	3.71	18	19	**23**	0.84	0.86	0.82	0.92	0.84	0.67	0.91	1.03	1.22	No	Raw
SAO 109252	3.74	31	**35**	**53**	0.64	0.52	0.45	0.66	0.59	0.42	0.97	0.87	1.06	Slight	FD
IRAS 05212+2655	3.74	26	28	**31**	1.81	1.68	1.60	1.48	1.38	1.25	1.22	1.22	1.28	No	Raw/FD
SAO 145698	3.80	36	38	**59**	0.58	0.54	0.44	0.59	0.54	0.36	0.99	1.00	1.20	No	Raw/FD
V1134 Tau	3.84	40	40	**54**	1.03	1.00	0.88	0.95	0.91	0.70	1.09	1.10	1.26	No	Raw
SAO 77229	3.87	32	**38**	**49**	0.96	0.90	0.87	1.00	0.86	0.67	0.96	1.05	1.30	Slight	Raw
IRAS 05232+2400	3.94	33	34	**40**	1.91	1.94	1.76	1.64	1.60	1.46	1.17	1.21	1.20	No	Raw/FD
BD+26 1131	4.06	38	**46**	**68**	0.78	0.57	0.50	0.77	0.66	0.45	1.02	0.87	1.11	Yes	FD
IRAS 05013+2704	4.12	35	**41**	**62**	0.71	0.64	0.55	0.69	0.61	0.42	1.03	1.05	1.32	Slight	Raw
SAO 77474	4.14	22	**25**	**35**	0.64	0.62	0.54	0.73	0.67	0.50	0.88	0.94	1.08	Slight	Raw/FD

Table B.1 – continued from previous page

Source	m_K	S/N			SD_{fringe}			SD_{total}			SD_{ratio}			Remarks	
		Raw	FD	CD	Raw	FD	CD	Raw	FD	CD	Raw	FD	CD	S/N Improve	Best fits to Fringes
IRAS 05551+2305	4.18	44	**47**	**70**	0.96	0.85	0.84	0.85	0.82	0.61	1.13	1.03	1.36	Slight	FD
IRAS 04320+2519	4.30	18	19	**24**	0.94	0.88	0.75	0.89	0.81	0.66	1.05	1.09	1.12	No	R/FD
IRAS 04320+2519	4.30	11	12	**14**	1.44	1.37	1.21	1.15	1.08	0.89	1.25	1.27	1.36	No	R/FD
SAO 77357	4.39	22	27	**40**	0.67	0.55	0.48	0.60	0.52	0.36	1.11	1.06	1.34	Slight	FD
SAO 76965	4.40	28	**31**	**39**	0.66	0.57	0.49	0.67	0.58	0.45	0.99	0.98	1.08	Slight	FD
HD 249571	4.50	26	**31**	**37**	0.73	0.58	0.51	0.84	0.74	0.59	0.88	0.78	0.87	Slight	FD
SAO 76952	4.70	17	19	**27**	0.81	0.71	0.60	0.93	0.82	0.61	0.87	0.86	0.98	Slight	FD
IRAS 06165+2431	4.87	20	**23**	**30**	0.63	0.55	0.47	0.64	0.56	0.45	0.97	0.98	1.06	Slight	Raw/FD
IRAS 03333+2359	5.07	21	**24**	**32**	0.67	0.53	0.41	0.71	0.58	0.41	0.94	0.90	0.98	Slight	FD

References

[1] Alcock C., Allsman R.A., Axelrod T.S., Bennett D.P., Cook K.H., Freeman K.C., Griest K., Marshall S.L., Peterson B.A., Pratt M.R., Quinn P.J., Reimann J., Rodgers A.W., Stubbs C.W., Sutherland W., Welch D.L., 1995, AJ, 109, 1653

[2] Alvarez R., Mennessier M.-O., 1997, A&A, 317, 761

[3] Aschenbach B. & Brinkmann W., 1975, A&A, 41, 147

[4] Aubourg E. et al, 1993, Nature, 365, 623

[5] Baug Tapas & Chandrasekhar T., 2012, MNRAS, 419, 886

[6] Bergeat J., Knapik A., Rutily B., 2002, A&A, 390, 987

[7] Bergeat J., Chevallier L., 2005, A&A, 429, 235

[8] Born E.& Debrunner H., 1979, Ap&SS, 63, 457

[9] Cabrera-Lavers A., González-Fernández C., Garzón F., Hammersley P. L., López-Corredoira M., 2008, A&A, 491, 781

[10] Carroll B. W., Dale A. O., 2007, An Introduction to Modern Astrophysics, Pearson Addison-Wesley

[11] Chandrasekhar T., 2005, Bull. Astron. Soc. India, 33, 87

[12] Chandrasekhar T. & Mondal Soumen, 2001, MNRAS, 322, 356

[13] Chandrasekhar T., Shah Rajesh, Mondal S., 2003, BASI, 31, 471

[14] Christian Buil, 1991, CCD Asttronomy, Willmann-Bell, Inc.

[15] Cruzalebes P., Lopez B., Bester M., Gendron E., Sams B., 1998, A&A, 338, 132

[16] Cutri R. M. et al, 2003, The IRSA 2MASS All-Sky Point Source Catalog, NASA/IPAC Infrared Science Archive, Available at : http://irsa.ipac.caltech.edu/cgi-bin/Gator/nph-dd?catalog=fp_psc

[17] Daubechies I., 1992, Ten Lectures on Wavelet, Society for Industrial and Applied Mathematics, Philadelphia

[18] De Becker M., Sana H., Absil O., Le Bouquin J.-B., Blomme R., 2012, MNRAS, 423, 2711

[19] di Benedetto G. P., 1993, A&A, 270, 315

[20] Diercks H. & Hunger K., 1952, Z. Astron., 31, 182

[21] Dyck H.M., Lockwood G.W., Capps R.W., 1974, ApJ, 189, 89

[22] Dyck H.M., van Belle G.T., Benson J.A., 1996, AJ, 112, 294

[23] Dyck H.M., van Belle G.T., Thompson R.R., 1998, AJ, 116, 981

[24] Eddington A.J., 1918, MNRAS, 69, 178

[25] Eisner J.A., Graham J.R., Akeson R.L., Ligon E.R., Colavita M.M., Basri G., Summers K., Ragland S., Booth, A., 2007, ApJ, 654, L77

[26] Fizeau A.H., 1868, C.R. Acad. Sci. (Paris), 66, 932

[27] Fried D.L., 1966, J. Opt. Soc. Am., 56, 1372

[28] Grossman A. & Morlet J., 1984, Decomposition of Hardy functions into square integrable wavelets of constant shape, Society for Industrial and Applied Mathematics, 15, 732-736.

[29] Han F., Mao R.Q., Lu J., Wu Y.F., Sun J., Wang J.S., Pei C.C., Fan Y., Tang G.S., Ji H.R., 1998, A&AS, 127, 181

[30] Hanbury Brown R. & Twiss R.Q., 1956, Nature, 178, 1046

[31] Haniff C. A., Scholz M., Tuthill P.G., 1995, MNRAS, 276, 640

[32] Hartkopf I., Mason D., McAlister A., Roberts C. Jr., Turner H., ten Brummelaar A., Prieto M., Ling F., Franz G., 2000, AJ, 119, 3084

[33] Harvey M., Oldag A., 2007, ApJ, 663, 543

[34] Helou George, Walker D.W., 1988, The IRAS Point Source Catalog v2.1 (PSC), NASA/IPAC Infrared Science Archive, Available at : http://irsa.ipac.caltech.edu/cgi-bin/Gator/nph-dd?catalog=iraspsc

[35] Herwig F., 2005, ARA&A, 43, 435

[36] Huber D. et al, 2012, MNRAS, 423, L16

[37] Kahane C., Jura M., 1994, A&A, 290, 183

[38] Kim J., Cho Se-Hyung., Oh Chung Sik., Byun Do-Young., 2010, ApJS, 188, 209.

[39] Koorneef J., 1983, A&A, 128, 84

[40] Labeyrie A., 1970, A&A, 6, 85

[41] Labeyrie A., 1975, APJL, 196, 71

[42] Lacour S., Tuthill P., Amico P., Ireland M., Ehrenreich D., Huelamo N., Lagrange A.-M., 2011, A&A, 532, 72

[43] Lang K. R., 1991, Astrophysical Data: Planets and Stars, Springer

[44] Lattanzio J.C., Wood P.R., 2003, in Habing Harm J., Olofsson Hans., eds, Asymptotic Giant Branch Stars, Springer, p.80-88

[45] Le Bertre T., Tanaka M., Yamamura I., Murakami H., 2003, A&A, 403, 943

[46] Le Blank Fransis., 2010, An Introduction to Stellar Astrophysics, John Willy & Sons Ltd, p240-248

[47] Lee Fugal D., 2009, Conceptual Wavelets In Digital Signal Proccessing, Space & Signals Technical Publishing

[48] Léna P., Leburn F. & Mignard F., 1998, Observational Astrophysics, Spinger, 2nd ed.

[49] López-Corredoria M. A., Cabrera-Lavers F. Garzón, P. L. Hammersley, 2002, A&A, 394, 883

[50] Lyne A.G., 1972, MNRAS, 158, 431

[51] MacMohan P.A., 1909, MNRAS, 69, 126

[52] Mason D., Hartkopf I., Raghavan D., Subasavage P., Roberts C. Jr., Turner H., ten Brummelaar A., 2011, AJ, 142, 176

[53] McAlister A., Hartkopf I., Hutter J., Shara M., Franz G., 1987, AJ, 93, 183

[54] McCarthy D. W. & Low F. J., 1975, ApJ, 202, L37

[55] McCaughrean J., Glindemann A., Birk C., Herbst M., Rohloff R.-R., Beckwith W., 1994, ExA, 3, 137

[56] Mennesson B. et al, 2002, ApJ, 579, 446

[57] Millan-Gabet R., Pedretti E., Monnier J. D., Schloerb F. P., Traub W. A., Carleton N. P., Lacasse M. G., Segransan D., 2005, ApJ, 620, 961

[58] Michelson A.A. & Pease F.G., 1921, ApJ, 53, 249

[59] Mondal S., 2004, Ph.D. Thesis, Gujarat Univ., India

[60] Mondal S. & Chandrasekhar T., 2002, MNRAS, 334, 143

[61] Mondal S. & Chandrasekhar T., 2005, AJ, 130, 842

[62] Nanavati S. & Panigrahi P., 2004, Wavelet Transform *A New Mathematical Microscope*, Vol.9, No.3, pp.50-64

[63] Nather R.E. & Evans D.S., 1970, AJ, 75, 575

[64] Nather R.E., McCants M.M., 1970, AJ, 75, 963

[65] Neufeld A., González-Alfonso E., Melnick J., Szczerba R., Schmidt M., Decin L., de Koter A., Schier F., Cernicharo J., 2011, ApJ, 727, 28

[66] Neugebauer G. & Leighton R.B., 1969, Two Micron Sky Survey (TMSS) Catalog, Online available at: http://vizier.cfa.harvard.edu/viz-bin/VizieR?-source=tmss

[67] Nishiyama S.,, Tamura M., Hatano H., Kato D., Tanabe T., Sugitani K., Nagata T., 2009, ApJ, 696, 1407

[68] Paresce F., 2003, AP&SS, 286, 297

[69] Perrin G., Ridgway S. T., Mennesson B., Cotton W. D., Woillez J., Verhoelst T., Schuller P., Coudé du Foresto V., Traub W. A., Millan-Gabet R., Lacasse M. G., 2004, A&A, 426, 279

[70] Perryman C. et al, 1997, A&A, 323, 49

[71] Pojmanski G., Maciejewski G., Pilecki B., Szczygiel D., 2005, ASAS catalog of Variable Stars, Online available at: http://vizier.cfa.harvard.edu/viz-bin/VizieR?-source=II/264

[72] Quirrenbach A., 2001, Ann. Rev. Astron. Astrophys., 39, 353

[73] Ragland S., 1996, Ph.D. Thesis, Devi Ahilya Univ., India

[74] Ragland S. et al, 2006, ApJ, 652, 650

[75] Rahasto M., Hamajima K., Ichikawa T., Ishida K., Hidayat B., 1984, Ann. Tokyo. Astron. Obs., 19, 469

[76] Richichi A., 1989, A&A, 226, 366

[77] Richichi A., 1994, IAU Symposium, 158, 71

[78] Richichi A., Chandrasekhar T., Lisi F., Howell R. R., Meyer C., Rabbia Y., Ragland S., Ashok N. M., 1995, A&A, 301, 439

[79] Richichi A., di Giacomo A., Lisi F., Calamai G., 1992, A&A, 265, 535

[80] Richichi A., Fors O., Mason E., Stegmeier J., Chandrasekhar T., 2008a, A&A, 489, 1399

[81] Richichi A., Fors O., Mason E., 2008b, 489, 1441

[82] Richichi A., Chen W. P., Fors O., Wang F., 2011, A&A, 532, 101

[83] Richichi A., Percheron I., Khristoforova M., 2005, A&A, 431, 773, CHARM2: An updated Catalog of High Angular Resolution Measurements, Online available at: http://vizier.cfa.harvard.edu/viz-bin/VizieR?-source=J/A+A/431/773

[84] Richichi A., Baffa C., Calamai G., Lisi F., 1996, AJ, 112, 2786

[85] Ricker G.R., Ryckman S.G., Ballintine J.E., Doty J.P., Downey P.M., Lewin G., Scheepmaker A., 1975, ApJ, 197, L83

[86] Ridgway S.T., Jacoby G.H., Joyce R.R., Siegel M.J., Wells D.C., 1982, AJ, 87, 808

[87] Ridgway S.T., Wells D.C., Joyce R.R., Allen R.G., 1979, AJ, 84, 247

[88] Saha S.K., 2002, Rev. Mod. Phys., 74, 551

[89] Samus N. N., Durlevich, O. V., et al., 2009, General Catalogue of Variable Stars, Online available at: http://vizier.cfa.harvard.edu/viz-bin/VizieR?-source=B/gcvs

[90] Scargle J. D., 1982, ApJ, 263, 835

[91] Schmidtke P.C., Africano J.L., Jacoby G.H., Joyce R.R., Ridgway S.T., 1986, AJ, 91, 961

[92] Simon M., Chen W. P., Forrest W. J., Garnett J. D., Longmore A. J., Gauer T., Dixon R. I., 1990, ASPC, 14, 205

[93] Singal A.K., 1987, A&AS, 69, 91

[94] Sloan G. C., Price S. D., 1998, ApJS, 119, 141

[95] Tej A., 1999, Ph.D. Thesis, Gujarat Univ., India

[96] Terzan A., Gosset E., 1991, A&AS, 90, 451

[97] Thomson R. R., Creech-Eakman M. J., van Belle G. T., 2002, ApJ, 577, 447

[98] Thureau N.D., Monnier J.D., Traub, W.A., Millan-Gabet R., Pedretti, E., Berger J.-P., Garcia M.R., Schloerb F.P., Tannirkulam A.-K., 2009, MNRAS, 398, 1309

[99] Tsuji T., 1978, PASJ, 30, 435

[100] Udalski, A., Szymanski, M., Kaluzny, J., Kubiak, M., Krzeminski, W., Mateo, M., Preston, G. W., Paczynski, B., 1993, Acta Astronomica, 43, 289

[101] van Belle G.T., 1999, PASP, 111, 1515

[102] van Belle G.T. et al, 1999a, AJ, 117, 521

[103] van Belle G.T. & Thompson R.R., 1999b, BAAS, 31, 1435, Available at:http://pti.jpl.nasa.gov/publications/aas_atlanta/atlanta0001_carbon.pdf

[104] van Belle G.T. & Thompson R.R., 1999, AAS, 195, 4501

[105] van Belle G.T., Thompson R. R. & PTI Collaboration, 2000, AAS, 197, 4502

[106] van Belle G.T., Thompson R. R., Creech-Eakman M. J., 2002, AJ, 124, 1706

[107] van Leeuwen, 2007, *Hipparcos, the New Reduction of the Raw Data*, Astrophysics and Space Science Library, Vol.350

[108] von Hoerner S., 1964, ApJ, 140, 65

[109] Wainscoat R. J., Cohen M., Volk K., Walker H. J., Schwartz D. E., 1992, ApJS, 83, 111

[110] Warner, B., 1988, *High Speed Astronomical Photometry*, Cambridge Univ. Press

[111] White N.M., 1987, *Lunar occultations: From conjecture to results*, Vistas in Astronomy, 30, pp.13

[112] White N.M.& Feierman B.H., 1987, AJ, 94, 751

[113] Whitelock P., Feast M., van Leeuwen F., 2008, MNRAS, 386, 313

[114] Whitelock P., Menzies J., Feast M., Marang F., Carter B., Roberts G., Catchpole R., Chapman J., 1994, MNRAS, 267, 711

[115] Whitford A.E., 1939, APJ, 89, 472

[116] Williams J.D., 1939, APJ, 89, 467

[117] Winters J. M., Le Bertre T., Jeong K. S., Nyman, L.-Å., Epchtein N., 2003, A&A, 409, 715

[118] Wittkowski M., Karovicova I., Boboltz D. A., Fossat E., Ireland M., Ohnaka K., Scholz M., van Wyk F., Whitelock P., Wood P. R., Zijlstra A. A., 2011a, The Messsenger, 145, 24

[119] Wittkowski M., Boboltz D. A., Ireland M., Karovicova I., Ohnaka K., Scholz M., van Wyk F., Whitelock P., Wood P. R., Zijlstra A. A., 2011b, A&A, 532, L7

[120] Wittkowski M., Hauschildt P.H., Arroyo-Torres B., Marcaide J. M., 2012, A&A, 540, L12

[121] Wood P.R., Habing H.J., McGregor, P.J., 1998, A&A, 336, 925

[122] Woodruff H.C., Ireland M.J., Tuthill1 P.G., Monnier J.D., Bedding T.R., Danchi W.C., Scholz M., Townes C.H., Wood P.R., 2009, ApJ, 691, 1328

[123] Young K., 1995, APJ, 445, 872

Publications attached with the thesis

1. **"Lunar Occultations of sources in the near infrared towards the Galactic centre"**
   T. Chandrasekhar and Tapas Baug
   2010, MNRAS, 408, 1006

2. **"Near Infrared Angular diameters of a few AGB variables by Lunar Occultations"**
   Tapas Baug and T. Chandrasekhar
   2012, MNRAS, 419, 866